Dual Mode Brain Near Infrared Spectroscopy and Electroencephalography

Hardware Design and Signal Processing

by

Shahbaz Askari

B.Sc. Electrical Engineering, Tehran University, 1996

A THESIS SUBMITTED IN PARTIAL FULFILLMENT

OF THE REQUIREMENTS FOR THE DEGREE OF

MASTER OF APPLIED SCIENCE

in

THE FACULTY OF GRADUATE AND POSTDOCTORAL

STUDIES

(Biomedical Engineering)

THE UNIVERSITY OF BRITISH COLUMBIA

(Vancouver)

July 2016

Abstract

Electroencephalography (EEG) and cerebral near-infrared spectroscopy (NIRS) are both well-known monitoring methods for analyzing cerebral neurophysiology and hemodynamics. Neuronal activity in the gray matter of the brain requires energy and thus a high metabolic rate, which is related to oxygen consumption. The blood regulatory system operates to ensure sufficient spatial and temporal distribution of oxygen and energy substrates to supply neuronal activity. In this study, we designed and developed a prototype NIRS/EEG instrument for recording electrophysiological activity and hemodynamic changes in the human forehead. This novel probe, combining both EEG and NIRS technologies, consists of Ag/AgCl EEG electrodes positioned between NIRS optodes. As ambient light is capable of contaminating the NIRS signal, a novel amplitude modulation methodology was incorporated into the NIRS/EEG device for multiplexing NIRS light sources and eliminating the interfering noise signal produced by ambient light. This method is based on the modulation of each specific NIR source by its specific carrier frequency. The summation of all sources and ambient interference is measured at the receiver site. A bandpass filter separates each source based on the carrier frequency. Three experiments were conducted using the aforementioned NIRS/EEG instrument. The experiments were performed on five healthy human subjects. The initial experiment was conducted to evaluate the functionality of the developed NIRS/EEG prototype. The association between gamma-band oscillations and total hemoglobin during subjective pain (Cold Pressor Test, CPT) was demonstrated. The increase in gamma-band oscillations, as measured by EEG electrodes on the forehead, and the increase of total hemoglobin, as measured by NIRS optodes on the

forehead, have been recorded and reported accordingly. Conventional EEG recording is conducted in the 0.16 to 70 Hz frequency range. However, ultra-low-frequency EEG, found in the range of 0.015 to 4 Hz, is highly informative and allows discovery of the general state of neurons. The genesis of low-frequency EEG signals may be non-neuronal. In the last experiment, the changes of pCO_2 and low-frequency EEG are measured concurrently and the results are presented accordingly.

Preface

Figures 1.1, 1.2, 1.3, and 1.4 from Chapter 1 as well as Figures 2.1, 2.2, 2.3, and 2.4 from Chapter 2 are used with permission from applicable sources.

This dissertation is ultimately based on a novel NIRS/EEG experimental apparatus and data collected using this device. The design of the EEG component of the device that has been used in the experiments discussed as part of this thesis, is the work of Zoya Bastany [1]. The NIRS hardware design, the combined NIRS/EEG probe design, as well as the implementation discussed in Chapter 2 and signal processing discussed in Chapter 3, are all my original work.

The second experiment in Chapter 3, "Hemodynamic and Electrophysiologic response to repeated CPT" is based on the Cold Pressor Test (CPT) protocol of "Hemodynamic Response to Repeated Noxious Cold Pressor Tests Measured by Functional Near Infrared Spectroscopy on Forehead" which was developed by Zeinab Barati and Dr Kambiz Pour Rezaee [2].

The investigations were conducted as part of a UBC CREB approved protocol to test non-invasive sensor prototypes developed by the Electrical and Computer Engineering in Medicine team at the Child and Family Research Institute in Vancouver, BC (H14-02000).

Table of Contents

Abstract ..... **ii**

Preface ..... **iv**

Table of contents ..... **v**

List of Tables ..... **viii**

List of Figures ..... **ix**

List of Abbreviations ..... **xii**

Acknowledgements ..... **xv**

Dedication ..... **xvi**

Chapter 1: Introduction **1**

1.1 Introduction to Near Infrared Spectroscopy 1

1.2 Introduction to Electroencephalography 5

1.3 NIRS Instrumentation 8

1.4 NIRS Theory and Formulations 9

1.5 NIRS Safety Considerations 14

1.6 Limitations of NIRS and EEG 15

1.6.1 NIRS Limitations: 15

1.6.2 EEG Limitations 16

1.7 The Motivation for Combined NIRS and EEG Recording. 16

1.7.1 Ultra-low-frequency EEG, Suppression Depression Recording 18

1.7.2 Epilepsy 19

1.7.3 Language Studies 20

1.7.4 Hypoxic Ischemia (HI) 20
1.8 Thesis Contributions 20
1.9 Thesis Outline 21
Chapter 2: Hardware Design and Prototyping 23
2.1 EEG/NIRS Design Review 25
2.1.1 Primary Definition of Design Input 25
2.1.2 NIRS Photo-detectors 26
2.1.3 Light Source and Driver 35
2.1.4 Time Domain and Frequency Domain NIR Source Multiplexing 42
2.1.5 Transmittance and Reflectance Probes 56
2.1.6 Light Source and Sensor Placement 58
2.2 The Method's Advantages Constraints, and Source of Errors 61
2.2.1 Scattering and Absorption of the Tissue 61
2.2.2 Effect of Ambient Light 62
2.3 Design, Implementation, and Prototyping 62
2.3.1 The Block Diagram of Near Infra-Red Spectroscopy Hardware 63
2.3.2 EEG Amplifier 64
2.3.3 Conclusion 64
Chapter 3: NIRS/EEG Validation 66
3.1 NIRS Recording During The Forearm Arterial Occlusion Test 67
3.1.1 Material and Methods 67
3.1.2 Results 68
3.2 Hemodynamic and Electrophysiologic Response to Repeated CPT 69
3.2.1 Materials and methods 70
3.2.2 Results 75

3.3 The Hypoxic Breathing Test: 82
3.3.1 Materials and Methods 84
3.3.2 Results 86
Chapter 4: Conclusion 92
4.1 Design and Implementation NIRS/EEG Instrument 92
4.2 NIRS/EEG Validation 93
Bibliography 96

List of Tables

Table 2-1 The Typical NIRS design input descriptions and specifications. 25

Table 2-2 The Typical EEG design input descriptions and specifications. 26

Table 2-3: General specification of LED and LD [8, 50]. 39

Table 2-4. Comparing two methods. 54

List of Figures

Figure 1-1: HbO2 and HHb absorption coefficients in infrared spectra (700-900 nm) [8]. 2

Figure 1-2: The light absorption coefficient of different biological substances. 3

Figure 1-3: Continuous wave NIRS 8

Figure 1-4: Time-resolved implementation of NIRS systems. 9

Figure 1-5 A complex, heterogeneous media properties. 12

Figure 2-1 Waterfall design process 24

Figure 2-2: The equivalent model of Photodiode. 27

Figure 2-3 A typical Spectral Responsivity of silicon photodiode. 28

Figure 2-4 The transform function (I-V) diagram of a silicon photodiode. 31

Figure 2-5 Trans-Impedance or current to voltage amplifier 34

Figure 2-6 The energy band diagram with and without forward voltage. 36

Figure 2-7: The emission spectrum (spectrum output) of multi-wavelengths LED. 37

Figure 2-8 Optical spectrum of LD and LED. 38

Figure 2-9 Voltage-controlled-current source driver. 42

Figure 2-10 Time-multiplexing and demultiplexing. 43

Figure 2-11 Frequency Division Multiplexing (FDM). 44

Figure 2-12 Modulation of sources in the NIRS/EEG optical source controller. 46

Figure 2-13 The estimation of each wavelength intensity at the receiver point. 48

Figure 2-14 Sallen-key configuration filter circuit. 49

Figure 2-15 Ambient light spectrum. 50

Figure 2-16 Frequency response of circuit (Gain in dB). 52

Figure 2-17 Frequency response of circuit. 52
Figure 2-18 The experimental test method. 53
Figure 2-19 Amplitude modulation technique and signal decomposition. 55
Figure 2-20 The path of light in reflectance probe. 57
Figure 2-21: The placement of EEG electrode in between receiver and sender. 59
Figure 2-22 The arrangement of EEG and NIRS optodes in the forehead. 59
Figure 2-23 Implemented NIRS/EEG probe. 60
Figure 2-24 The block diagram of the NIRS/EEG device. 63
Figure 2-25 The implemented NIRS/EEG prototype. 64
Figure 3-1 The positioning of NIRS probe on the forearm. 68
Figure 3-2: The change of HbO_2 and HHb during arterial occlusion. 69
Figure 3-3. The arrangement of EEG and NIRS optodes in the forehead. 71
Figure 3-4: The placement of EEG electrode in between NIRS optodes. 72
Figure 3-5 The probe integrates NIRS optodes and EEG electrodes. 73
Figure 3-6 EEG B1, B2 electrode positions 73
Figure 3-7. The timing diagram of the CPT experiment. 75
Figure 3-8 The hemodynamic response to cold pressor test (CPT) 76
Figure 3-9 The neuronal activity, and hemodynamic variation during CPT. 78
Figure 3-10 Changes of gamma-band power during CPT. 79
Figure 3-11 Gamma-band oscillations during CPT 80
Figure 3-12 Time-frequency transform of EEG signal in gamma-band (30-80Hz). 81
Figure 3-13 The timeline of the experiment. 86
Figure 3-14 EEG and hemodynamic changes induced by hypoxic breathing. 88
Figure 3-15 EEG and NIRS in the frontal and sensory cortex during hypoxic breathing. .. 89
Figure 3-16 The time-frequency analysis of signal based on STFT. 90

Figure 3-17 The superposition of EEG signal A1 and HHb multiplied by 50K..... 90

List of Abbreviations

AC	Alternative Current
ADC	Analog to Digital Converter
APD	Avalanche Photodiode
BP	Blood Pressure
CBF	Cerebral Blood Flow
CPT	Cold Pressor Test
CW	Continuous Wave
DAC	Digital to Analog Converter
DC	Direct Current
DDS	Direct Digital Synthesis
DPF	Differential Path-length Factor
EEG	Electroencephalography
FDM	Frequency Division Multiplexing
FET	Field Effect Transistor
fMRI	Functional Magnetic Resonance Imaging
fNIRS	Functional Near Infrared Spectroscopy
FPCB	Flexible Printed Circuit Board
GaAlAs	Gallium Aluminum Arsenide
GaAs	Gallium Arsenide

HbO_2	Oxygenated Hemoglobin
HHb	Deoxygenated Hemoglobin
HI	Hypoxic Ischemia
IR	Infra Red
LD	Laser Diode
LED	Light Emitting Diode
MBLL	Modified Beer-Lambert Law
MEG	Magneto Encephalography
MRI	Magnetic Resonance Imaging
NIRS	Near Infrared Spectroscopy
OD	Optical Density
PCA	Principal Component Analysis
PCB	Printed Circuit Board
PD	Photo Detector
PET	Positron Emission Tomography
ROI	Regions Of Interest
SNR	Signal to Noise Ratio
SPI	Serial Peripheral Interface
STFT	Short Time Fourier Transform
TD	Time Domain
TIA	Trans Impedance Amplifier
TPSF	Temporal Point Spread Function
ULN	Ultra-Low Noise

USB	Universal Serial Bus
UV	Ultra Violet

Acknowledgements

The completion of this dissertation would not have been possible without the support and encouragement of many people.

Firstly, I offer my greatest gratitude and regard to my supervisor, Prof. Guy A Dumont, for his invaluable encouragement, intellectual advice, and patience. I am greatly indebted to him for his support and constant inspiration throughout my research. I would like to express my deepest appreciation to my co-supervisor, Prof. Ali Gorji, for his excellent advice and guidance. I would especially like to express my most sincere gratitude to Zoya Bastany for her constructive comments and unrelenting support. I am grateful to Prof. Naznin Virji Babul for her steadfast encouragement and patience.

Dedication

To my parents . . .

To Zoya, my wife, and best friend…

For their immeasurable spiritual support and love.

Chapter 1: Introduction

1.1 Introduction to Near Infrared Spectroscopy

The application of light energy for the investigation of human tissues dates back to the early 20th century, when it was first employed as a diagnostic tool for breast lesions [3]. After the discovery of the role of hemoglobin in oxygen transport, many researchers investigated the spectroscopic characteristics of tissue oxygenation, and the absorption spectra of oxyhemoglobin (HbO_2) and deoxyhemoglobin (HHb) were discovered [4]. In 1938, Matthes and Gross, two German scientists, determined the spectroscopic characteristics of HbO_2 and HHb from human tissue, by utilizing two wavelengths in red and near infrared spectra [5]. The Beer-Lambert law was the first quantitative approach used for estimating the concentrations of HbO_2 and HHb. However, the Beer-Lambert law is only applicable in non-scattering environments. Consequently, it cannot be applied to biological tissues to describe their absorption, transmission, and scattering, as a result of their diffused spectroscopy. Hence, Delpy introduced the modified Beer-Lambert law (MBLL) in 1988. Delpy's law can be employed in environments with light scattering [6]. The MBLL has become the gold-standard approach for monitoring concentration changes.

In 1977, Jobsis monitored the concentration of HbO_2 and HHb in the human brain for the first time, non-invasively. His work is regarded as the origin of near-infrared spectroscopy. Since

that time, NIRS has become of increasing interest to many researchers, and the technology has since been applied to many different purposes [7].

NIRS technology can be used as a non-invasive neuroimaging method to detect hemodynamic changes in the cerebral cortex. NIRS takes advantage of the fact that in the NIR spectra (~700-900nm, also known as the 'optical window'), only HbO_2 and HHb are relatively highly sensitive to infrared light (700-900 nm), while skin, bone, and other tissues of the human body are almost transparent in this spectrum [6]. See Figure 1-1(below).

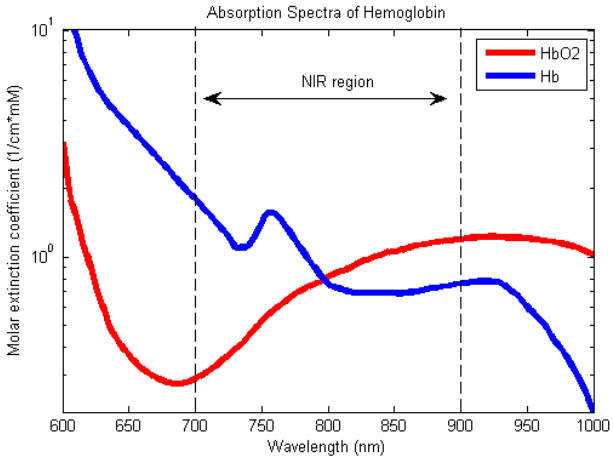

Figure 1-1: HbO2 and HHb absorption coefficients in infrared spectra (700-900 nm) [8].

In the spectrum of the optical window, infrared light is able to sample the biological tissues with appropriate depth of penetration. Water and hemoglobin in the tissue massively absorb infrared radiation with wavelengths greater than 900nm. Therefore, the optimum spectral range for cerebral spectroscopy or the 'NIR optical window', is the spectrum in which the light is largely absorbed by HbO_2 and HHb. As shown in Figure 1-2 (below), other substances like collagen and fat in the NIR optical window are sensitive to NIR radiation, and may absorb near infrared wavelengths more strongly than HbO_2 and HHb. However, the high absorption coefficients of these biological materials are not a major issue in cerebral NIR since the

concentrations of these materials are dramatically lower relative to the concentration of HbO_2 and HHb in cerebral NIRS [8].

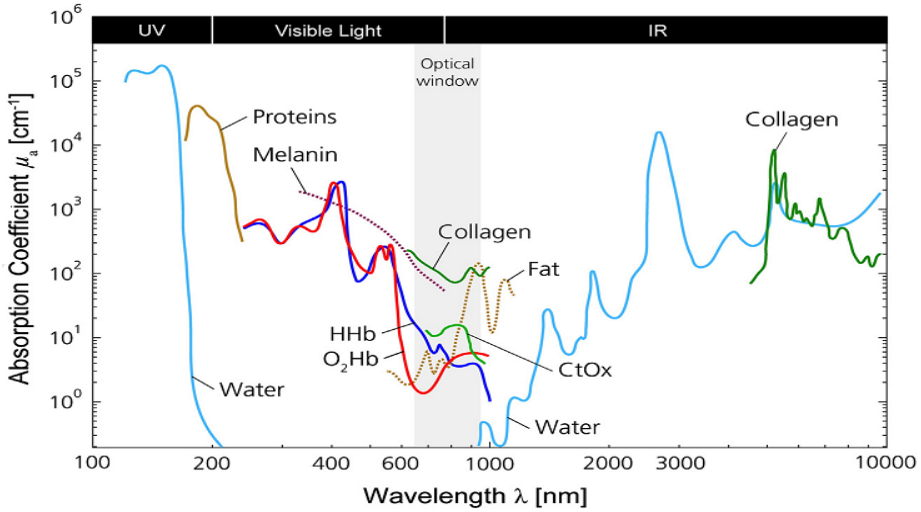

Figure 1-2: The light absorption coefficient of different biological substances.
The highlighted spectra are referred to as the NIR optical window (~630 to ~970nm) [8].

In principle, a NIRS instrument must include at least one light source and one photodetector. In practice, more than one light source and one photodetector are utilized, and, generally, more photodetectors than light sources are employed in a NIRS instrument. The light source emits near-infrared light that can penetrate the skin, scalp, and the extracranial and intracranial tissues of the human brain. Incident light follows a banana-shaped pathway and finally approaches the photodetectors [9].

The tissue chromophores absorb a portion of the emitted light. A part of the emitted light may be scattered from its original direction. Usually, only the attenuation phenomenon is considered in studies, and the scattering effect of tissues is neglected due to the high computational complexity of accounting for it [8, 9].

The depth of tissue penetration is roughly half of the separation distance between the optodes. In some applications, two or three photodetectors are associated with one light source. In such cases, photodetectors are divided into "Near" and "Far" optodes. The "Near" optodes monitor hemodynamic changes of solely the superficial layers of the brain, such as the scalp and skull, while the "Far" optodes are only slightly associated with hemodynamic changes in the superficial layers of the brain and more dominantly with hemodynamic changes in deeper layers of the brain. Thus, by using mathematical processing, hemodynamic changes in the superficial layers can be eliminated and concentration changes related to the deep layers of the brain can be estimated [9].

In comparison with other brain imaging techniques (e.g., functional magnetic resonance imaging [fMRI], electroencephalography [EEG], and positron emission tomography [PET]), NIRS has significant advantages such as portability and low cost. More importantly, since NIRS uses non-ionizing electromagnetic radiation in the near-infrared spectrum, a safe form of radiation, NIRS measurements are not harmful and have been categorized as a non-invasive imaging method [10]. Furthermore, challenges created by motion artifacts due to subjects' slight movements can be overcome with respect to NIRS [11], whereas motion artifacts are still a serious issue in the aforementioned imaging modalities. NIRS can measure hemodynamic changes in capillaries whilst fMRI can only accomplish measurements in small vessels. Therefore, NIRS measurements are more accurate for monitoring the local hemodynamic characteristics of tissue at the microscopic scale. The temporal resolution of NIRS is greater than in fMRI; however, the spatial resolution of NIRS is lower than in fMRI [12].

NIRS has several disadvantages including low SNR (signal-to-noise ratio), moderate spatial resolution, and low penetration depth through the scalp due to power limitations of the light sources. NIRS, with both its advantages and disadvantages weighed against each other, is widely believed to be a promising method for human brain imaging [7].

1.2 Introduction to Electroencephalography

Electroencephalography (EEG) is a measurement of the neurophysiological activity of the brain, taken from the scalp. Hans Berger conducted the first EEG measurements in 1929, although similar investigations were accomplished in animals as early as 1870 [13].

The nervous system consists of neuronal and glial cells. Glial cells, sometimes called neuroglia, are non-neuronal cells that surround and provide support and protection for neurons. Glial cells are located in the central and peripheral nervous system. Each neuron consists of axons, dendrites, and a cell body. Neurons respond to stimuli and transmit information. An axon is a long cylinder that transmits electrochemical impulses. An axonal transport tunnel length may vary between less than one millimeter and more than a meter in humans [13].

The activity of neurons in the CNS is mostly due to the synaptic current transferred between neuronal junctions. The action potential (AP) is the electrochemical mechanism that transmits the information. APs are generated by the displacement of Na+ and K+ ions across the neuron membrane, and they temporarily change the internal electric potential of the neuron. The AP electric potential is about -70mV [13].

An EEG signal is a recording of current that flows during synaptic excitations of the dendrites of many pyramidal neurons in the gray matter of the brain. The pyramidal neurons

are located vertically in cortical layers III, V, and VI. Because of the attenuating impacts of the skull, the spatial density of cortical neuronal activities is crucial, forming the voltage that can be detectable on the skull [14]. The EEG signals, which are derived from the cerebral cortex, are mostly correlated with spatial neuronal activities. However, some recorded signals don't have neuronal genesis and are considered non-neuronal EEG signals.

Conventional concepts of electroencephalography consider neurons and their proximal dendrites to be the most important active originators of the EEG signal recorded on the scalp. However, according to recent studies, cerebral neuronal functionality is not the only source of recorded EEG signals. Glial cells may generate slow local field potentials during spreading depression, seizures, and sleep. Cerebrospinal fluid and partial CO_2 pressure can also be considered a cause of slow potential shifts in surface EEG. These slow potential changes were suggested to have originated across the blood brain barrier (BBB) [15].

In conventional EEG recordings, signals are usually recorded within the frequency bandwidth of 0.16Hz to 70Hz. However, according to some studies, by extending this frequency bandwidth to lower frequencies, more information can be extracted from the EEG signal. In addition to non-neuronal EEG signals, spreading depression is one of the most significant features in low-frequency EEG. Spreading depression is relatively dominant and results in rapid depolarization of neuronal tissues. The amplitude of SD varies between 5 to 30mv (with invasive electrodes), and its duration can be between 30 to 90 seconds. The SD propagation velocity in the brain is about 3 to 5mm/min.

According to the filter effects of the skull, and in the presence of other distractive slow shift potentials, the recording of an SD signal with the non-invasive method can be a challenging task.

Moreover, sometimes it is hard to distinguish SD signals from other slow potentials. Although the most distinctive characteristic of the SD signal is the propagation phenomenon, the propagation mechanism is not reported for non-neuronal EEG signals [15].

Recording SD signals with non-invasive methods is accomplished using a novel amplifier, and an appropriate set of electrodes, as has been demonstrated recently in rats [16]. Although the propagation of SD is a distinctive feature that may distinguish SD from other similar artifacts, during the noninvasive recording of SD, it is not always easy to identify the propagation. Detecting and calculating SD propagation using adjacent non-invasive electrodes is not always feasible. According to recent studies, the distribution of the SD within the tissue is accompanied by hemodynamic variations in the tissue. During SD observed in animal subjects, the blood flow pattern of capillaries is rigorously disturbed[17, 18]. Consequently, using a NIRS/EEG method can provide supplementary information about the hemodynamic variation of the tissue combined with the electrophysiological activity of the tissue during SD.

Brain tissues have limited energy reserve and require a continuous supply of glucose and oxygen through cerebral blood flow. A sudden increase in demand necessitates swift changes in cerebral blood flow (CBF). The neural activity of the brain is regularly followed by local changes in CBF and blood oxygenation. These regional hemodynamic changes of the brain are detectable with functional magnetic resonance imaging (fMRI). Growing evidence shows that neurons, glia, as well as vascular cells are all structurally, and functionally associated. In this study, we propose the concurrent measurement of local hemodynamic changes and neurophysiological activity of the brain [19, 20]. For these reasons, a NIRS/EEG device may provide important information

about the hemodynamic changes and neurophysiology of the brain, that may be translated to neuronal metabolism, neurovascular functionality, and the electrochemical activities of neurons.

1.3 NIRS Instrumentation

NIRS can be implemented based on three dominant techniques: continuous wave (CW) NIRS, time-domain (TD) NIRS, and frequency-domain (FD) NIRS. The latter two techniques may also be referred to as time-resolved techniques. The CW systems are primarily based on changes in the intensity of light within its pathway. The intensity of the input light beam gradually decreases as it passes through biological tissues. Therefore, its intensity is decreased at the receiver site. The CW method is not able to estimate the absolute concentration of chromophores in the area of interest. However, by making a few assumptions and applying several constraints, the CW approach can be successfully applied to a variety of investigations, including within commercial products [8, 9]. A schematic plan of CW NIRS is depicted in Figure 1-3(below).

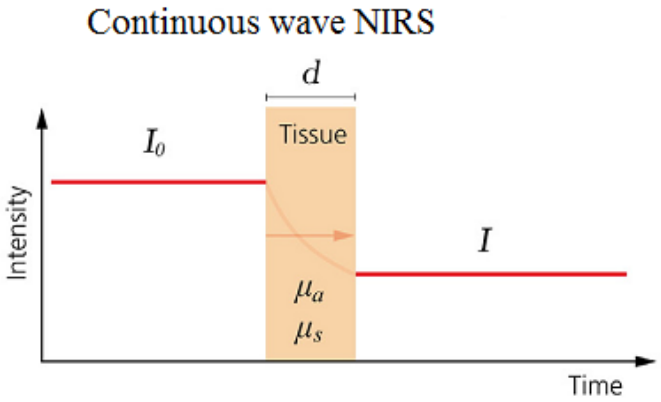

Figure 1-3: Continuous wave NIRS
NIRS implementations using the continuous wave technique are based on intensity attenuation of incident light beam; scattering and absorption account for the attenuation of incident light [8]

Time-resolved techniques for NIRS implementation include time-domain and frequency-domain implementations, as shown in Figure 1-4. In the time-domain technique, an impulse light beam is employed as the input to the system. Therefore, the output light is assumed to be a temporal point spread function (TPSF). Alternatively, in the frequency-domain method, an AC photon density wave is applied to the system as an input. Based on biological properties of tissue in the path of light beams, the amplitude and phase of input waves are altered accordingly [8].

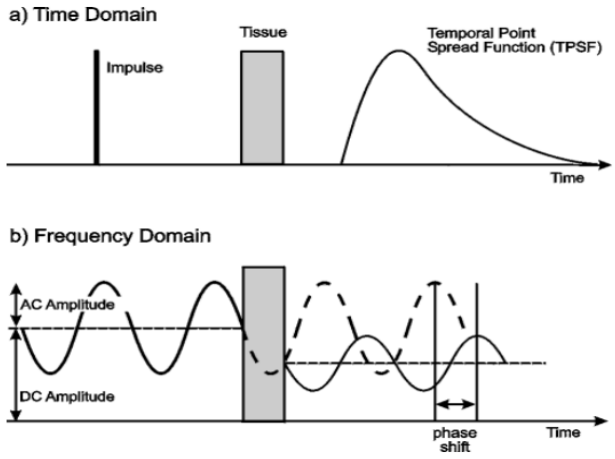

Figure 1-4: Time-resolved implementation of NIRS systems.
(a) Time-domain NIRS is based on the measurement of a temporal point spread function (TPSF). (b) Frequency-domain NIRS is based on phase and amplitude shifts of the incident light. [21].

1.4 NIRS Theory and Formulations

Incident light may be absorbed, scattered, or transmitted by a given media. We assume that incident light encounters a cubic homogenous media (thickness, *L,* and concentration, *C*). According to Beer-Lambert's law, we have:

$$I = I_0 e^{-\sigma C x} = I_0 e^{-\mu x} \qquad \textbf{Equation 1-1}$$

In Equation 1-1 (above), I_0 is the intensity of incident light, x is the depth that light beam has penetrated, I is the intensity of light in depth x, μ is the linear attenuation coefficient and finally, σ is the cross section of the material. This equation is valid under the assumption that no scattering phenomenon is present [22].

The linear attenuation coefficient μ is dependent on wavelength of incident light beam, Thus the Beer-Lambert would be dependent on the wavelength λ and is given by:

$$I(\lambda) = I_0(\lambda) e^{-\mu(\lambda) x} \qquad \textbf{Equation 1-2}$$

Two other parameters, *transmittance* (T) and *optical density* (OD_λ) can be defined according to the following formulae:

$$T = \frac{I(\lambda)}{I_0(\lambda)} = e^{-\mu(\lambda) L} \qquad \textbf{Equation 1-3}$$

$$OD_\lambda = -\ln \mathrm{T} = -\ln\left(\frac{I(\lambda)}{I_0(\lambda)}\right) = \mu(\lambda) L \qquad \textbf{Equation 1-4}$$

$I_0(\lambda)$ is the intensity of incident light at wavelength λ , $I(\lambda)$ is the intensity of light at wavelength λ, μ is the linear attenuation coefficient at wavelength λ and finally L is the actual path length.

The instrument does not easily measure absorbed light; therefore, the light that has been transmitted through the path of attenuation is measured. The light detector measurements are proportional to the derivative of optical density. Therefore, we may substitute A_λ for OD_λ,

yielding Equation 1-4 (above). It is apparent from Equation 1-4 (above) that the deeper the light beam goes, the higher the values of absorbance will be. [22].

The x is replaced with L since the separation distance between source and detector is fixed. New parameter extinction coefficients appear in this equation. Knowing that that $\varepsilon = 0.4343\sigma$ and $\mu = \sigma C$, and substituting them in Equation 1-4 (above),[23] we have:

$$OD_\lambda = \mu_{(\lambda)} L \qquad \textbf{Equation 1-5}$$

$$OD_\lambda = \varepsilon_{(\lambda)} CL \qquad \textbf{Equation 1-6}$$

In Equation 1-6 (above) OD_λ is the optical density at wavelength λ, $\varepsilon_{(\lambda)}$ is the extinction coefficient at wavelength λ, and L is the inter-optode (source and receiver) separation distance.

The Beer-Lambert Law does not consider the scattering effect in transparent media and assumes that light beams propagate along their original pathway [24]. This is, however, a controversial assumption for compound materials such as biological tissues. It is optimal that the scattering effect should also be taken into account for biological tissues, especially in the brain. In order to incorporate the scattering effect, Equation 1-6 (above) is multiplied by a corrective factor called the Differential Path Length Factor (DPF).

The dimensionless DPF model increases the path length for light beams to account for the scattering effect. In addition, G is a geometrical factor added to Equation 1-6 (above) to compensate for the scattering attenuation effect. We can simply assume that the DPF does not change during NIRS. So, we define d = L×DPF as the optical path length [24]. These collectively result in the modified Beer-Lambert Law (MBLL):

$$OD_\lambda = \varepsilon_\lambda C\ (L \times DPF) + G\ \ = \varepsilon_\lambda Cd + G \qquad \textbf{Equation 1-7}$$

In Equation 1-7 (above) OD_λ is the optical density at wavelength λ , $\varepsilon_{(\lambda)}$ is the extinction coefficient at wavelength λ, and L is the inter-optodes (source and receiver) separation distance. DPF is differential path-length factor, and G is a geometrical factor.

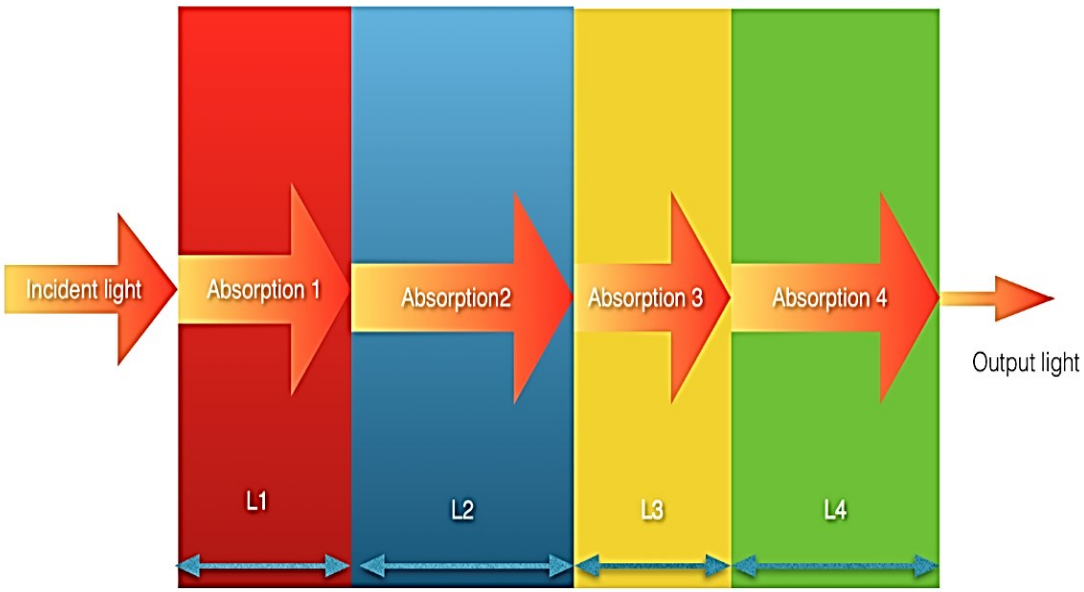

Figure 1-5 A complex, heterogeneous media properties.
A complex media may be decomposed into individual homogenous layers with respect to their extinction coefficients, each can be considered as a homogenous media and analyzed accordingly. Equation 1-8 (below) [24]

Among different tissues of the human body, hemoglobin is the only substance that absorbs light in the near-infrared range. Other present tissues and substances are relatively transparent to light in the NIR range. Therefore, using NIRS, oxygenated- and deoxygenated hemoglobin (HbO_2 and HHb, respectively) concentrations can be measured. One advantage of using A(λ) in place of I(λ) is that in multi-layer materials, it can be easily summed. Assume an n-layer

compound material (Figure 1-5 above). Each layer has its corresponding parameters $\epsilon_{i\lambda}, C_i \; and \; L_i$:

$$OD_{total,\lambda} = OD_{1,\lambda} + OD_{2,\lambda} + \cdots + OD_{n,\lambda} \qquad \textbf{Equation 1-8}$$

$$= (\epsilon_{1,\lambda} C_1 L_1 + \epsilon_{2,\lambda} C_2 L_2 + \cdots + \epsilon_{n,\lambda} C_n L_n)$$

In Equation 1-7 (above) ϵ_λ, d and G are constant for a specific wavelength λ. Thus, the differential form of this equation can be written as:

$$\Delta OD_\lambda = \varepsilon_\lambda d \Delta C. \qquad \textbf{Equation 1-9}$$

In this equation, the change in optical density (ΔOD_λ) is proportional to the concentration variation (ΔC).

Since there are mainly two light-sensitive substances (HbO_2 and HHb) in the medium, two wavelengths, λ_1 and λ_2 , are utilized to generate two equations. These two equations can be described as follows:

$$\Delta OD_{\lambda_1} = \varepsilon_{\lambda_1}^{\mathrm{O_2Hb}} d \Delta C_{\mathrm{O_2Hb}} + \varepsilon_{\lambda_1}^{\mathrm{HHb}} d \Delta C_{HHb}$$

$$\Delta OD_{\lambda_2} = \varepsilon_{\lambda_2}^{\mathrm{O_2Hb}} d \Delta C_{\mathrm{O_2Hb}} + \varepsilon_{\lambda_2}^{\mathrm{HHb}} d \Delta C_{HHb}. \qquad \textbf{Equation 1-10}$$

The linear equations in Equation 1-10 (above) can be written in a matrix form given by:

$$\begin{bmatrix} \Delta OD_{\lambda_1} \\ \Delta OD_{\lambda_2} \end{bmatrix} = \begin{bmatrix} \varepsilon_{\lambda_1}^{\mathrm{O_2Hb}} d & \varepsilon_{\lambda_1}^{\mathrm{HHb}} d \\ \varepsilon_{\lambda_2}^{\mathrm{O_2Hb}} d & \varepsilon_{\lambda_2}^{\mathrm{HHb}} d \end{bmatrix} \begin{bmatrix} \Delta C_{\mathrm{O_2Hb}} \\ \Delta C_{\mathrm{HHb}} \end{bmatrix}. \qquad \textbf{Equation 1-11}$$

The unknown parameters in linear system

Equation 1-11 (above) are $\Delta C_{\mathrm{O_2Hb}}$ and ΔC_{HHb}. Solving the linear system yields:

$$\Delta C_{\mathrm{O_2Hb}} = \frac{1}{d}\frac{\Delta OD_{\lambda_1}\varepsilon_{\lambda_2}^{\mathrm{HHb}} - \Delta OD_{\lambda_2}\varepsilon_{\lambda_1}^{\mathrm{HHb}}}{\varepsilon_{\lambda_1}^{\mathrm{O_2Hb}}\varepsilon_{\lambda_2}^{\mathrm{HHb}} - \varepsilon_{\lambda_1}^{\mathrm{HHb}}\varepsilon_{\lambda_2}^{\mathrm{O_2Hb}}} \qquad \textbf{Equation 1-12}$$

$$\Delta C_{HHb} = \frac{1}{d}\frac{\Delta OD_{\lambda_2}\varepsilon_{\lambda_1}^{\mathrm{O_2Hb}} - \Delta OD_{\lambda_1}\varepsilon_{\lambda_2}^{\mathrm{O_2Hb}}}{\varepsilon_{\lambda_1}^{\mathrm{O_2Hb}}\varepsilon_{\lambda_2}^{\mathrm{HHb}} - \varepsilon_{\lambda_1}^{\mathrm{HHb}}\varepsilon_{\lambda_2}^{\mathrm{O_2Hb}}} \qquad \textbf{Equation 1-13}$$

Finally, blood oxygenation and blood volume are given by:

Total Blood oxygenation level:

$$= \Delta C_{\mathrm{O_2Hb}} - \Delta C_{HHb} \qquad \textbf{Equation 1-14}$$

Totol Blood volume level:

$$= \Delta C_{\mathrm{O_2Hb}} + \Delta C_{HHb} \qquad \textbf{Equation 1-15}$$

1.5 NIRS Safety Considerations

NIRS is a comparatively harmless optical method employing non-ionizing radiation; it is non-invasive and applies low power radiation to analyze the tissue. Since NIR wavelengths are used to investigate the tissue of interest, the heat generated in the tissue by the radiated NIR, is identified as the most significant risk. IEC 62471 is a standard guideline for LED-based devices [25] and are applicable in LED-based NIRS devices [26, 27]. Most commercial devices consider power levels of 0.5 to1.5mW, which are harmless, even for application on newborn infants [27].

1.6 Limitations of NIRS and EEG

1.6.1 NIRS Limitations:

In the cerebral NIRS, there is no direct path between the light source and the receiver, and therefore, a scattering probe is more applicable and convenient relative to transitional probes. In the scattering probe, the light samples a banana-shaped area within the brain. The separation distance between the two optodes is proportional to the maximum depth that the optodes are able to sample. The SNR of the signal decreases dramatically by increasing the separation distance between the optodes. Consequently, depth of penetration can be identified as a limitation of NIRS. In the hair-covered part of the scalp, the depth of penetration is often worse because of the high absorption of melanin pigments. In NIRS, based on the scattering phenomenon, the scattering rate of the signal must be considered unchanged. Neglecting the change in scattering rate may be determined as another limitation of cerebral NIRS. However, the fixed scattering rate of the tissue during an experiment may be a reasonable assumption that can be applicable in most of the cases [28].

The received signal at the receiver point carries not only the information of the tissues located at penetration depth but also the other more superficial layers that are located in the sampling path. This additional information may reduce the spatial resolution of NIRS[8, 28].

Electrode fixation and optical coupling are other limitations of NIRS. Since the intensity of light at the receiver site is exponentially related to the inter-optode separation distance, any unwanted change in inter-optode distances or direction may cause variation in the detected intensity at the receiver site [29].

Brain NIRS measures hemodynamic changes in the tissue of interest that are widely correlated with local physiological conditions. However, the measured signal may be contaminated with problematic interference. Motion artifacts are the unwanted effects of motion of the subject during measurement that may cause the variation in the optical properties of a sampled area of NIRS optodes, and consequently, undesired variation in the NIRS signal, as detected by NIRS sensors [11].

Physiological artifacts are the other artifacts that may contaminate the NIRS signal, due to other physiological activities of the body. Physiological interference associated with NIRS is usually called “global interference” or “systemic interference” and includes cardiac pulsation, respiration, blood pressure (Mayer waves) and other homeostatic variations [30].

1.6.2 EEG Limitations

The most significant limitation of EEG is the weak spatial resolution. Since EEG measurements are usually conducted on the surface of the scalp, the received signal is the summation of many neuronal action potentials, which represent EEG activity in the brain tissue underlying the scalp. The spatial resolution of a single electrode on the surface is about one centimeter in the cortex and includes action potentials from hundreds of thousands of neurons. Consequently, EEG is not a very useful tool in terms of pinpointing the exact source of abnormal activities in the brain [31].

1.7 The Motivation for Combined NIRS and EEG Recording.

The main motivation for combined NIRS and EEG recording is that both technologies are well-known monitoring methods for describing neurophysiology and neuro-metabolic activities.

EEG measurements are favored with respect to temporal resolution. The EEG signal represents a summation of the neurophysiological activity in a particular area of the brain. Most EEG signals are associated with the neural activity of an enormous number of neurons that are connected to each other and firing concurrently. EEG measurements are very informative in both the time and frequency domains, and can provide crucial information for diagnosis and control of treatment in neurological disorders [8, 28].

Increasing the number of channels and using electrodes with the smaller surface area may improve the spatial resolution of EEG. Moreover, by using fine invasive electrodes, this resolution can be increased dramatically to accurately detect and localize the point of dysfunction [32].

The brain has high-energy requirements. About 20% of the oxygen and 25% of the glucose utilized by the body are dedicated exclusively to brain activity, although the brain represents only 2% of the body's total mass. Restoration and maintenance of ion gradients dissipated by signaling processes, such as post-synaptic and action potentials, as well as uptake and recycling of neurotransmitters, are the essential processes contributing to the significant energy requirements of the brain. In other words, neuronal activity in the gray matter, in terms of synaptic activities and action potentials, corresponds to high glucose and oxygen consumption as well as high water and CO_2 production [19].

A stable regulatory system operates to guarantee sufficient spatial and temporal distribution of energy substrates for ongoing neuronal activity. Astrocytes, a type of glial cell, are responsible for the distribution, production, consumption, and storage of brain energy. A remarkable characteristic of brain energy metabolism is the tight coupling that exists between energy

requirements and supply (reflected by glucose and oxygen distribution within the vasculature). Admittedly, task-dependent events that increase the cerebral activity are regularly followed by an increase in local blood flow and glucose consumption [28].

NIRS signals are primarily correlated to the available oxygenated and deoxygenated blood in the tissue. As previously mentioned, variation in the metabolism of the tissue is associated with changes in local cerebral blood flow. However, changes in cerebral blood flow are not necessarily equivalent to a shift in neuronal metabolism related to synaptic activity [19]. General oxygenation, heart rate, and blood pressure may also cause variations in local cerebral blood flow. Combining EEG and NIRS signals may provide useful information about neuronal activity and blood flow to the tissue, concurrently. The combination of these two technologies allows investigators to study the tissue from two distinct and essential perspectives [31].

According to contemporary literature, there are several applications for combined NIRS/EEG recording. The following four subsections of this document discuss major applications and motivations for combined NIRS/EEG measurements.

1.7.1 Ultra-low-frequency EEG, Suppression Depression Recording

In conventional EEG, physicians are usually interested in bandwidths between 0.16 Hz to 70 Hz. In 2005, Speckmann, Gorji, and their team found that ultra-low-frequency EEG, occurring in the bandwidth ranging from 0.015 to 4 Hz, is a magnificent feature and indicator for discovering the general state of neurons [33]. They attempted to identify how ultra-low frequency EEG activity contributes to the characterization of surface EEG [34, 35]. Detecting the low-frequency component of EEG signals by non-invasive electrodes on the scalp is challenging. The substantial cause of difficulty in this task is due to the electrical characteristics of the skull bone

and skin tissues. Other challenges include the electrochemical reaction between electrodes and the skin, which generates a low-frequency voltage that corrupts the very low voltage EEG signals on the skin. ovement may also be another potential source of artifacts [36].

One of the motivations for developing a NIRS/EEG apparatus is to find the potential correlation between EEG and cerebral oxygenation in a particular area of the brain. This correlation may be observed either in ultra-low-frequency EEG (0.015 Hz to 1 Hz) or normal EEG signals (0.16 Hz to 70 Hz) and oxygenation. According to recent investigations, significant hemodynamic variations were observed during suppression depression. Monitoring the hemodynamic changes of the tissue by using cerebral NIRS during suppression depression, can help to confirm the recorded SD signal. On the other hand, since the recording of suppression depression (SD) may be challenging in some instances, NIRS recording presents an alternative to ultra-low-frequency EEG.

1.7.2 Epilepsy

The investigation of cerebral blood flow (CBF) and EEG in epileptic patients is another major application of combined NIRS/EEG technology. This technique can be employed in the pre-surgical study of epileptic patients, for the purposes of localizing the center of epilepsy and quantifying post-surgical side effects [37]. NIRS combined with video EEG is a novel development for the evaluation of epileptic patients. It may become a widely adopted and essential tool for the management of epileptic patients in daily clinical practice, particularly in neonates and children [38].

1.7.3 Language Studies

The study of the brain's ability to integrate and interpret information is one of the most challenging research areas in neuroscience. Multiple evaluation techniques integrated into a multi-modal approach may represent informative features for language investigations. While every evaluation technique has its advantages and disadvantages, the integration of methods can help the investigators to elucidate certain aspects of neural network capacity for processing information. These measurements should ideally provide researchers with parameters that describe the neural activities and the hemodynamic and metabolic variations of areas of interest. NIRS/EEG recordings can provide a better understanding of the mechanisms that are involved in cerebral activation. Compared with fMRI, the NIRS/EEG technique can be conducted under conditions comparable to daily life [39, 40].

1.7.4 Hypoxic Ischemia (HI)

Any potential hypoxic ischemia (HI) injury in neonates must be identified, as they may lead to neural disability. In a recent study, the amplitude-integrated EEG (aEEG) and NIRS were recorded concurrently. By analyzing concurrent NIRS and aEEG signals, HI can be estimated accurately and can be detected in its early stages. Investigators have suggested this methodology for monitoring the progress of HI treatments. The tissue oxygenation index, measured via NIRS, detects acute changes in cerebral oxygenation and is highly associated to HI (sensitivity = 0.97). According to this study, the aEEG measurements correlated well with HbO_2 during the entire HI event [41].

1.8 Thesis Contributions

The major contributions of this thesis are summarized as follows. This thesis:

- Introduces a novel method for simultaneous NIRS/EEG recording to monitor cerebral electrophysiological activity and hemodynamic changes of the brain simultaneously.
- Design and implements a NIRS/EEG prototype for recording EEG and NIRS signals concurrently. Furthermore, a special probe consisting of EEG electrodes and NIRS optodes has been designed and prototyped.
- Proposes frequency multiplexing based on amplitude modulation for multiplexing the NIR sources and eliminating the effect of ambient light noise.
- Evaluates the functionality of the device by conducting two experiments: measurement of oxygenation in the forearm during occlusion and measurement of hemodynamic changes during a cold pressor test (CPT).
- Evaluates the correlation between Total-Hb and power of EEG gamma-band oscillations during the cold pressor test.
- Evaluates the correlation between Total-Hb and low-frequency EEG signals during hypoxic breathing.

1.9 Thesis Outline

Chapter 1 provides background information on NIRS and EEG, the motivation of dual mode NIRS/EEG recording, and the limitations of NIRS and EEG recording. Chapter 2 is dedicated to the design, implementation, and prototyping of the NIRS/EEG instrument. In this chapter, we provide the alternative methods and components for developing the NIRS/EEG device. The primary focus of this chapter is on NIRS and the concurrent recording of EEG signals. The technique of source multiplexing based on frequency modulation is presented in this chapter.

Chapter 3 is dedicated to the evaluation of NIRS/EEG functionality and signal processing of NIRS/EEG measurements. In this chapter, we present three experiments:

The initial experiment consisted of the measurement of NIRS on the forearm during occlusion to evaluate the functionality of the NIRS instrument in detecting hemodynamic responses to occlusion, for the purposes of evaluating the functionality of the NIRS instrument. The second experiment consisted of the measurement of electrophysiological and hemodynamic responses to CPT with the goal of assessing the correlation between the power of gamma-band oscillation and hemodynamic changes in the tissue. The third experiment in this chapter presents the hemodynamic and electrophysiological responses of the brain under hypoxic breathing conditions. The correlation between low-frequency components of EEG and hemodynamic fluctuations are described in this experiment. The last section of this thesis, Chapter 4 summarizes the outcomes and findings of this thesis and identifies prospective directions and opportunities for study.

Chapter 2: Hardware Design and Prototyping

The NIRS/EEG instrument is a research-based dual-mode recording device that may have widespread applications in brain research studies. By concurrently recording both neurophysiological and hemodynamic signals, it can provide information beyond available monitoring devices, on a given subject of study. It appears that there are significant relations between the cerebral blood oxygenation and the neurophysiological activity of the subject. The primary goal of designing this device was to measure the electrical activity of the brain and the optical density of the area at different wavelengths. The EEG and NIRS signals can be recorded concurrently. This chapter addresses and evaluates the major topics of NIRS/EEGS design, such as:

- Available alternatives for NIRS sensors (photodetectors).
- Near Infrared light source alternatives and available drivers.
- Frequency and time-multiplexing methods.
- Estimation of penetration depth and inter-optode separation distance.
- Arrangement of EEG electrode and NIRS optodes

The principal methods and elements of the NIRS/EEG device are the primary concern of this design process. The design process was essentially based on the waterfall design model. The design starts with user requirements; in the next step, all user requirements must be translated to

design inputs. In the design process, the alternative methods, elements, and materials should be identified and evaluated [42].

Based on the constraints, advantages, and drawbacks of the proposed methods or elements, the applicability of the methods or elements has to be investigated and addressed. The process of design is commonly defined as the integration of several components, methods, and materials. The ultimate aim of the design process is the effective integration of these materials, components, and methods to meet the design input requirements efficiently [42, 43].

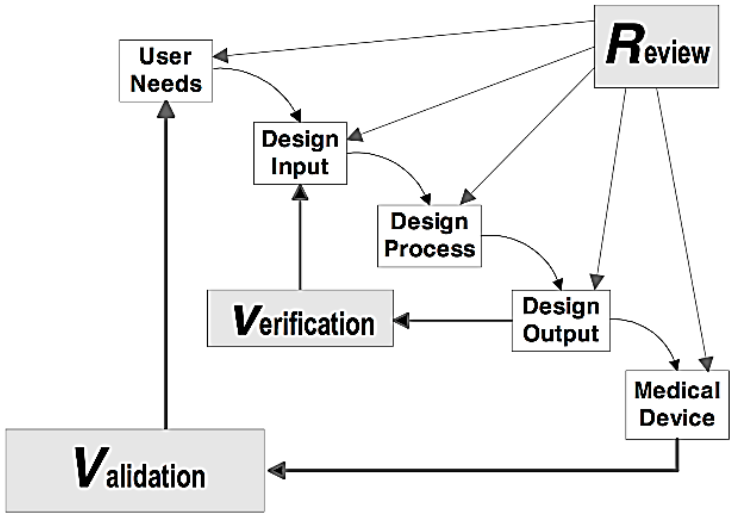

Figure 2-1 Waterfall design process
1 Waterfall design process. The design proceeds in a consistent sequence of stages or steps. Essentially, methods and elements are developed, and a device is designed to satisfy those requirements. Then, the design needs to be evaluated. After evaluation, the design inputs, methods, and elements might be revised. This process may be iterated many times until the output meets the requirements [42].

In this process of design, the physical dimensions and appearance of the device are not matters of concern. Instead, the technical specifications, principal elements, functional structures, and methods are investigated and addressed.

2.1 EEG/NIRS Design Review

2.1.1 Primary Definition of Design Input

The design input is included in the basic requirement for the NIRS/EEG device. In this section, we intend to define the technical requirements of the instrument. Additionally, the standard considerations and some user requirements have to be considered as design inputs [42]. The aim of this thesis is to elaborate on the technical aspects of the prototype design. Technical requirements and restrictions will be defined. The foundation of the design input is primarily based on the primary aim of the research and the general requirement of the NIRS device. See Table 2-1 (below) and Table 2-2 (below).

NIRS design input description	Design input specification
Number of sources	4 sources
Wavelengths of Source Stimulation	670,770,810,850nm
Delivered power	<1.6mW/cm2
Number of Recorders	1-32 channels
Bandwidth of recorders	0.01Hz to 80Hz
Power supply isolation	6000V
Isolation Capacitor	<100pF
Isolation between Optical stimulators and recorders	Electrically isolated
Sample rate	250Hz to 2KHz
Resolution	14bit

Table 2-1 The Typical NIRS design input descriptions and specifications.

EEG design input description	Design input specification
Number of sources	More than 16 channels
Input impedance	>1 G Ohm
CMRR	>100db at 50Hz
Input max noise	<5uV
Bandwidth of recorders	0.01Hz to 80Hz
Power supply isolation	6000V
Isolation Capacitor	<100pF
Isolation between Optical stimulators and recorders	Electrically isolated
Sample rate	250Hz to 2KHz
Resolution	14bit

Table 2-2 The Typical EEG design input descriptions and specifications.

2.1.2 NIRS Photo-detectors

The photo-detectors are the most crucial component of the NIRS device. Photo-detectors are found within the probe. They measure the transmitted intensity of optical energy at the receiver site. Photo-detectors absorb light at receiver sites and convert the absorbed optical energy to electrical current; this current is highly correlated with the incident light [8]. The sensitivity of photodetectors to the incident light may be considered as the most dominant parameter for choosing appropriate photodetector, although the price, packaging, size, linearity and safety are the other parameters that should be considered during component evaluation [22].

A variety of photo-detector components are available: photoresistors, photodiodes, phototransistors. The photoresistors are light dependent resistors, and the resistance of a photoresistor decreases with increasing incident light energy; in other words, it presents photoconductivity. The most important disadvantage of photoresistors is their low responsivity to

NIR wavelengths. Another drawback of photoresistors is the limited frequency response of the component [22].

Photodiodes provide light detection for wavelengths ranging from 380nm to 1700nm [44, 45]; they are available in different sizes, packages and specifications to meet the customer's space constraints, sensitivity, and speed requirements.

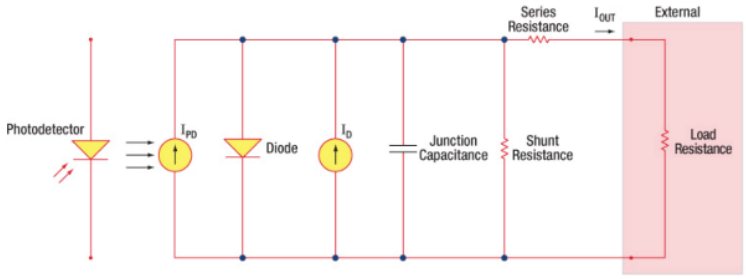

Figure 2-2: The equivalent model of Photodiode.
Photodiode current (I_{pd}) is a dependent current source and is related to the intensity of the received light; I_d is the dark current of the junction [22, 46].

A silicon photodiode is fabricated from a shallow diffused p-n junction, commonly a p-on-n form. Furthermore, "P-type" devices (n-on-p) are available for intensified responsivity in the 1µm region. Modern silicon photodiodes are regularly fabricated using planar diffusion or ion-implantation methods [47]. When photons with energy higher than 1.1eV (the band gap of silicon) reach the region, electrons absorb the energy of photons; consequently, the energy level of electrons increases. Increasing the energy level of electrons generates electron-hole pairs. The depth at which electrons absorb the photons is in accordance with their level of energy; the lower the energy of the photons, the deeper they are likely to be absorbed by electrons. The electron-hole pairs drift apart, and the minority carriers gradually move to reach the junction.

The electric field sweeps the minority carrier and if the circuit is closed, tiny external current flows through it [47]. If the bulk carriers consume the minority carriers of the region before touching the junction, the minority carriers are wasted, and no external current flows through the circuit. A drift of temperature in the silicon photodiode changes its spectral response curve; heating shifts the peak toward the longer wavelengths, and conversely, cooling shifts the spectral response peak toward the shorter wavelengths [47, 48].

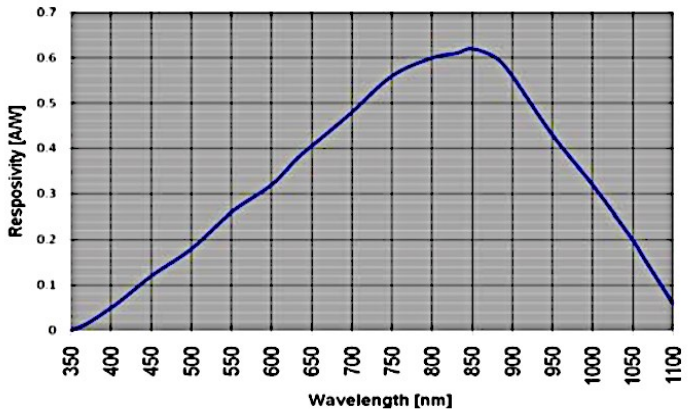

Figure 2-3 A typical Spectral Responsivity of silicon photodiode.
A typical spectrum of a Silicon photodiode. As it is illustrated, the sensitivity of the photodiode is maximum at 850nm (NIR wavelength). (Picture from PDB-C160SM Datasheet, Advance Photonics. Inc.)

For estimating the oxygenation of tissue by near-infrared spectroscopy, the optical density of the tissue of interest has to be measured at more than one wavelength. Consequently, any shift in spectral responsivity may cause a gain error in photodetectors and eventually, an error in final estimation. The dependency of spectra-dominant-wavelengths in silicon photodiodes is minimal at NIR wavelengths (0 to 0.1% /°C). However, this dependency is more significant in infra-red wavelengths greater than 1064nm (0.75 to 0.9% /°C). On the other hand, the spectral responsivity of silicon photodiodes indicates that they are sensitive to NIR wavelengths (600nm to 1100) and may be an appropriate choice for NIRS applications [22]. See Figure 2-3 (above).

2.1.2.1 Modes of Operation (Biasing)

Either photovoltaic or photoconductive circuit configurations can be applicable in designing a photodiode amplifier. Choosing an appropriate configuration depends upon the speed, dark current, gain and noise requirements. In the photovoltaic circuit configuration, the diode is in the forward-biased state, while, in photoconductive configuration, the diode is reversely biased [48].

In photovoltaic circuit configuration, since the diode is unbiased, less dark current flows through the junction; moreover, a photovoltaic configuration exhibits less noise and higher sensitivity. The speed of operation is not a primary concern in designing a NIRS/EEG device; however, noise, sensitivity, and dark current of the sensor should be considered as essential requirements. Linearity is another condition that can be fulfilled in a photovoltaic configuration [48].

2.1.2.2 Photodiode Electrical Characteristics

2.1.2.2.1 Junction Electrical Capacitance

The boundaries of the depletion region, in the presence of an electric field, act as a capacitor. Consequently, an equivalent capacitance has to be considered in the equivalent electrical model. Given that the depletion region represents the capacitor effect, the equivalent junction capacitance is directly proportional to the area of the depletion region [47]. On the other hand, the equivalent capacitance is inversely proportional to the effective width of the depletion region. Higher resistivity substrates exhibit lower junction equivalent circuits. This equivalent junction capacitance is voltage dependent and, in the presence of bias voltage, changes slightly [47].

2.1.2.2.2 Dark Current

While ideally no dark current should flow at zero bias, in practice, most zero-bias configurations have a slight voltage difference across the junction of the photodiode. Even in the absence of incident light, this slight reverse voltage causes a reverse saturation current called dark current. The dark current increases with increasing reverse voltage or ambient temperature [47]. The dark current equation can be described as a reversed saturation current in the absence of incident light:

$$I_D = I_{SAT}\left(e^{qV_A/k_BT} - 1\right) \qquad \textbf{Equation 2-1}$$

In Equation 2-1 (above), I_D is the dark current, I_{SAT} is the reverse saturation current of the diode, q is the absolute value of electron charge, V_A is the junction voltage, k_B is the Boltzmann constant (1.38 x 10^{-23} J/K), and T is the absolute temperature of the junction [22, 47].

2.1.2.2.3 Spectral Response or Responsivity

The responsivity of a photodiode aids in the precise perception of the sensitivity of a photodiode to the specific incident wavelength. The responsivity of the photodiode is defined as the ratio of the electrical current that is generated by a specific wavelength relative to its power. Somehow, it represents the efficiency of the photodiode in absorbing incident light and converting it to the photocurrent at a specific wavelength. The silicon photodiode has an acceptable spectral response or responsivity at NIR wavelengths. Given the high responsivity of photodiodes in NIR wavelengths, they can be considered as an appropriate alternative for the detection of NIR wavelengths [22, 47].

$$R_\lambda = {}^{I_P}/_{P} \qquad \textbf{Equation 2-2}$$

In Equation 2-2 (above), R_λ is the responsivity of the component, I_P is the current that is generated by incident light at a specific wavelength, and P is the initial energy of incident light.

2.1.2.2.4 Linearity of Transform Function

The transform function of the photodiode (voltage to current) with no incident light, resembles that of a regular diode. In the forward-bias configuration, an exponential function can express voltage-to-current transform function. However, in the absence of incident light, in the reverse bias configuration, there is only a reverse saturation current that flows through the circuit. In the presence of incident light, the I-V curve shifts by the amount of current that is generated with respect to the optical energy [48], see Figure 2-4.

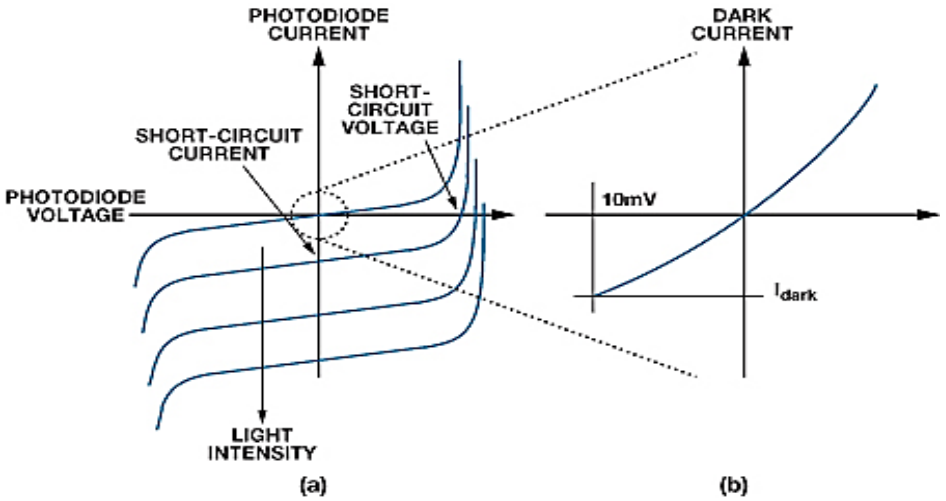

Figure 2-4 The transform function (I-V) diagram of a silicon photodiode.
In a forward bias configuration, there is an exponential relationship between current and voltage. However, in a reverse configuration, without the presence of incident light, there is only reverse saturation current. By illuminating the junction, the photocurrent flows through the diode and shifts the diagram [22, 48].

Equation 2-2 (above), and Equation 2-3 (below), explicitly show that the association between the power of incident light and the photocurrent is linear, given that the diode is configured in the reverse bias configuration and the reverse-biased voltage does not exceed the diode breakdown voltage [22, 48].

$$I_{Total} = I_{SAT}\left(e^{qV_A/k_BT} - 1\right) - I_P = I_D - I_P \qquad \textbf{Equation 2-3}$$

In this equation, I_P is the current that generated by incident light at a specific wavelength. I_D is the dark current of the diode, and I_{Total} is the total current of the diode.

Either voltage or current of the photodiode can describe the intensity of incident light. However, the current exhibits a more linear relationship with the light intensity. An additional circuit, called a trans-impedance amplifier, is required to convert the photocurrent to the voltage appropriately [47, 48].

2.1.2.3 Limitations of Photodiodes

In cerebral near-infrared spectroscopy, regularly, a high ratio of the optical energy is absorbed and scattered by the chromophores and particles of the tissue, and only a small amount of optical energy reaches the photodiodes. The limitation of photodiodes in this application is their low responsivity [22, 48]. The Avalanche Photodiode (ADP) with improved responsivity can be considered as an alternative for low-intensity light detection applications.

2.1.2.4 Avalanche Photodiode (APD)

The Avalanche Photodiode (APD) mechanism is similar to that of conventional photodiodes. The incident light absorbed by electrons increases the level energy of the electrons, and consequently, electron-holes appear in the junction. The ratio of the number of electron-hole pairs, created by incident light, to the number of incident photons is called quantum efficiency (QE) and is regularly expressed as a percent (%).

In APDs, the mechanism by which carriers are generated is similar to that of the standard photodiode; however, in the presence of a reverse voltage, in pn junction, the electrical field pushes the electrons to drift to N+ and holes to P+. Therefore, the quantum efficiency of the photodiode is improved. The stronger the electrical field, the higher the drift speed of the carriers. In this design, we did not consider the implementation of APDs as optical sensors. However, APDs seem to be a distinctive candidate detector for NIR/EEG improvement, particularly when the testing environment involves a high level of light absorption. Due to the high voltage of ADP, some preventive actions should be taken to improve the safety of the device, and eliminate the risk of electric shock to the operator and the patient [47, 48].

2.1.2.5 Trans-impedance Amplifier

In trans-impedance amplifiers, as previously mentioned, the photocurrent is proportional to the intensity of incident light. A linear equation can explicitly define this relation. A trans-impedance amplifier is a low-noise and sensitive current-to-voltage converter that converts the photocurrent generated by photodiodes into photo-voltage, which is more appropriate for use in signal amplification. See Figure 2-5.

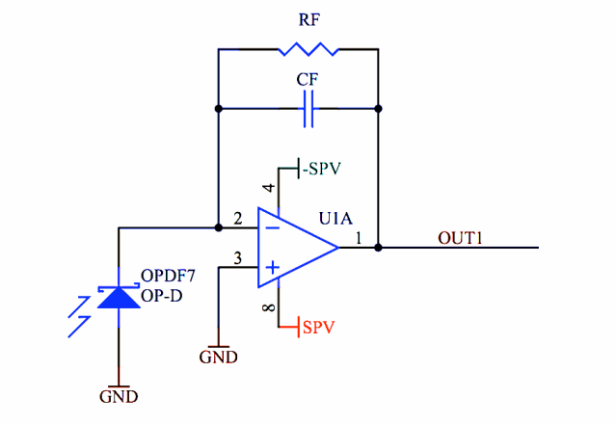

Figure 2-5 Trans-Impedance or current to voltage amplifier
Trans-impedance or current-to-voltage amplifier (reverse bias configuration). The trans-impedance amplifier converts the photocurrent generated by incident light into voltage. The current flows through an RF resistor and generates voltage that is proportional to the applied light intensity at the output[47].

The trans-impedance gain is defined as:

$$Gain = \frac{V_{out}}{I_{diode}} = R_f \qquad \textbf{Equation 2-4}$$

In Equation 2-4 (above), V_{out} is the output voltage; I_{diode} is the current of the photodiode (photocurrent). The thermal noise of the circuit is proportional to the square root of feedback resistor and is defined as:

$$\text{Thermal noise} = \sqrt{4 \times kTBR_f} \qquad \textbf{Equation 2-5}$$

In Equation 2-5 (above) k is the Boltzmann constant, T is the absolute temperature, B is the noise bandwidth, and R_f is the feedback resistor. Since the output voltage of the trans-amplifier is proportional to the feedback resistor (Rf) and the thermal noise is proportional to the square root

of Rf, on increasing the feedback resistor, the SNR (just for thermal noise) of the amplifier improves [22].

As the amplifier detects the current of the photodiode and converts it to voltage, the input bias current of the trans-amplifier needs to be minimized to the lowest possible level. FET input amplifiers are an appropriate alternative for developing trans-impedance amplifiers. In this design, a low input bias current Op-amp (TLV 271, Texas Instruments, typical input bias current = 25pA) has been employed.

The junction capacitance of the photodiode is proportional to the area of the junction and restricts the frequency response of the circuit. In the reverse bias configuration (photoconductive), since the width of the depletion area extends the equivalent capacitance decreases. Similarly, in forward bias (photovoltaic), the equivalent capacitor of the junction raises according to the shrinkage of depletion. The photoconductive circuit configuration has been considered for the implementation of a trans-amplifier [22, 47].

2.1.3 Light Source and Driver

A light source with a specific wavelength is essential to emit the light at a specific wavelength and intensity. Controlling the light intensity is crucial not only for improving the SNR of the output signal but also for the safety matters. A considerable part of the incident light may be absorbed in the superficial layer of the skin and converted to thermal energy. By controlling the light source current, the radiation power of the light source can be controlled and secured. In designing NIR/EEG light source controllers, acquiring Light Emitted Diodes with reliable and precise intensity control appears crucial.

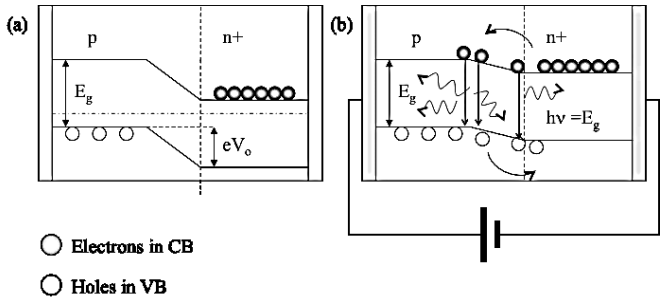

Figure 2-6 The energy band diagram with and without forward voltage.
a) The energy band diagram without forward-voltage, the built in voltage V_0 prevents the electrons from diffusing from n+ to p. b) The applied forward voltage eliminates V_0 and causes the electrons to diffuse to p side. The recombination around the junction and inside diffusion area of the electrons in p side releases photons and emits light [49].

2.1.3.1 Light Emitting Diode Wavelengths

The light emission mechanism of an LED is illustrated in Figure 2-6 (above). In the presence of forward bias voltage, the electrons obtain sufficient energy to pass the forbidden energy gap and approach the conduction band. If each electron that is present in the conduction band returns to the lower level of energy, it delivers a certain amount of energy in the form of light photons [49]. The wavelength of the photons released by the electron is determined by the Planck-Einstein equation:

$$E_g = hf = \frac{hc}{\lambda} \qquad \textbf{Equation 2-6}$$

In Equation 2-6 (above), E_g is the energy of the band in electron-volt, h is the Planck universal constant, f is the frequency of generated waves, c is the speed of light and is a wavelength of generated wave, and λ is the wavelength of light.

Theoretically, E_g is independent of the forward bias current and is strongly related to the physical structure, materials, and density of the thermal energy of the junction [49].

$$E_g(T) = E_g(0) - \frac{\alpha T^2}{T + \beta} \qquad \textbf{Equation 2-7}$$

In this equation (Equation 2-7, above), T is the absolute temperature of the junction, α and β are material constants, and $E_g(0)$ is related to the energy gap of the junction at temperature absolute zero.

GaAs is one of the materials that is often utilized to integrate near infrared LEDs. However, its atomic structure may be modified to form specific band-gap energy and, consequently, a specified wavelength of emitted light. This process is called band-gap energy tailoring. Band-gap energy tailoring is essential to the manufacturing of light-emitting diodes [49].

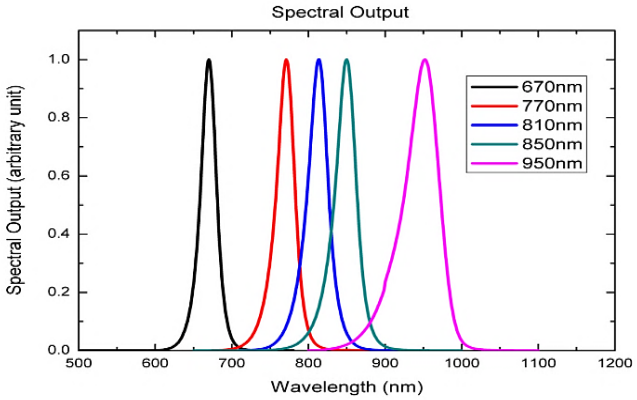

Figure 2-7: The emission spectrum (spectrum output) of multi-wavelengths LED.
Band-gap energy tailoring is usually used to integrate LEDs with specific spectra. This diagram is the spectra of multi-wavelength LED. All the LEDs are integrated into one package. (Image from MTMD6788594SMT6 datasheet from Marktech Optoelectronics Inc.) The dominant wavelength of emission is the wavelength at which LED radiates the most relative power. The dominant wavelength may shift according to the junction current, or with junction temperature changes.

In near-infrared spectroscopy, the wavelength of the light sources plays a substantial role in the measurements. The wavelength of a given LED is determined as an independent parameter from both the junction current and temperature. However, in practice, the emission spectrum, or the dominant wavelength of emission, may be displaced slightly according to the junction temperature or the junction current. Typically, LEDs are represented by their dominant wavelength of emission.

2.1.3.2 Light Emitting Diodes (LED) and Laser Diodes (LD) in NIRS.

An ideal light source component for NIRS emits light at several wavelengths with minimum bandwidths [3]. The bandwidth of LEDs is comparatively wide, ranging from 20 to 100 nm, whereas laser diodes (LDs) have a more compressed spectral deviation from central wavelengths, that is, from 0.1 to 2 nm. See Figure 2-7. Having a narrower spectral bandwidth has made laser diodes (LDs) more suitable for some applications where the interference between the spectrum of light sources is the primary concern [8, 50]. See Figure 2-8 (below).

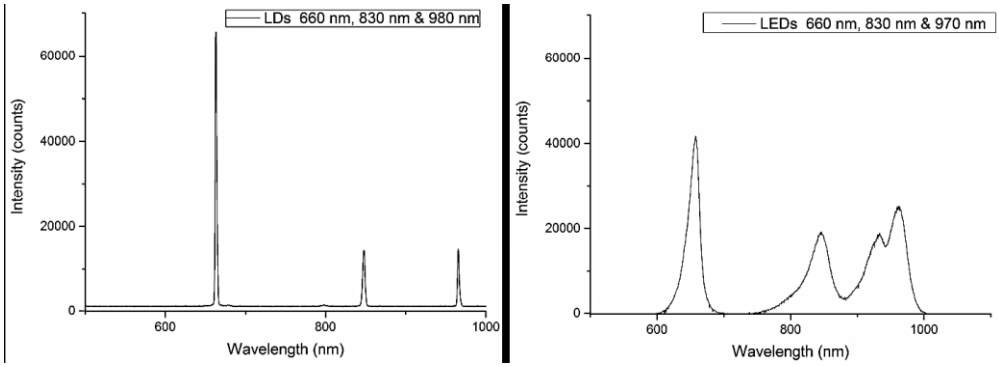

Figure 2-8 Optical spectrum of LD and LED.
The total spectra of light source implemented by a laser diode (LD) (Left) and LED (right) are described in this figure. The spectra of LDs are sharper than those of LEDs. Moreover, LDs are able to release higher optical power at specific wavelengths[8, 50].

To determine an appropriate type of light source, physical specifications such as size, shape, and weight, may be considered. The LDs are regularly larger and heavier than LEDs. Consequently, for portable instruments, LEDs are preferable to LDs. A general comparison of LEDs and LDs is shown in Table 2-3 (below).

General specifications of light emitter diode and laser diodes							
Type	BW (FWHM)	Size	Avail. colors	Divergence	Fiber coupling	Cost	Safety
LEDs LDs	~35nm <1nm	Small Bulkier	Many Limited	Broad Narrow	Possible Easy	Low High	Higher Lower

Table 2-3: General specification of LED and LD [8, 50].

Safety considerations have the highest priority in medical instruments, especially when the device is intended for direct contact with the human body. The light source in NIRS is not ionizing, and it has no dangerous effects on human genes; however, the heat generated by the light source has the potential to cause burn damage to human tissues. The radiated and conducted heats are two types of thermal energy that may be considered as a cause of injury during the experiment [8, 27].

The radiated thermal energy is due to the energy produced by the light source that subsequently radiates into the tissue. However, the source of conducted thermal energy is the heat generated in the semiconductor junction inside the light source [4, 6]. The amount of heat that can cause tissue damage depends on the wavelength and the spot size of the light source.

In LEDs, the light immediately diverges from its original direction. The divergence of light in LEDs leads to a more extended spot size. While the radiated heat is usually not a matter of

concern in LED light sources, the intrinsically-collimated light of LDs could cause severe burn damage to the skin [51],[6].

Depending on the source-detector arrangement, the light, which is emitted from the light source, can travel through two types of trajectories to reach the detector: an angular trajectory or a straight trajectory. When both source and detector are placed on the same side of the head, the light is scattered, absorbed and transmitted through an angular (also known as banana-shaped) trajectory to reach the detector. In this configuration, called a reflectance configuration, the inter-optode distance is recommended to be no less than 2.5 cm. Since this arrangement covers only a limited region of the brain, the output signal contains local information.

Conversely, when collecting information about the general functionality of the brain is required, source and detector should be on opposite sides of the brain. In this arrangement, the light passes a straight trajectory, until it approaches the detector. This mode is classified as transmission mode and is preferred in pulse oximetry of the digits, or in infants with a biparietal distance of 8cm or less. Since the power of LED sources is relatively low, they are usually used in reflectance configuration imaging (except when the distance between optodes is relatively small, such as in a pulse oximeter). Light emitted from LDs, however, can travel a longer distance before excessive attenuation occurs. Therefore, LDs are more appropriate for the transmittance mode [51],[7].

2.1.3.3 Light Emitter Diode Electrical Specification

The emission power of candidate LEDs is a critical parameter for the selection of a suitable LED for device implementation. According to safety regulations, the total power of emitted light should not exceed 1.5mW. Considering the electrical model of an actual diode, by adjusting the

current that flows through an LED, the radiated power of such a LED can be controlled. Therefore, a current source may be acquired as a driver for the LED. There are several alternative electronic circuits for implementing the current controller of LED drivers.

In NIR spectroscopy, the wavelength of the light sources has a significant role in the measurements. The wavelength of LED is usually determined as an independent parameter from the junction current and temperature. In practice, the emission spectrum containing the dominant wavelength may be slightly displaced according to the temperature or junction current variation [22]. The variation in the corresponding absorption coefficient of HHb and HbO_2 may lead to undesired effects in further computations.

For compensating the spectrum shift error, the wavelengths should be chosen in the areas where the slope of the absorption diagram is not high and the absorption coefficient diagram is relatively flat. According to recent investigations, 740nm and 850nm are more convenient for HHb and HbO_2 measurements, however, for performing future investigations, the device is designed in such a way that it is able to control four wavelengths concurrently [22].

2.1.3.4 LED Current Source Driver.

The current source is an alternative for controlling the LED's power of radiation. There are several configurations to implement a current source. **Error! Reference source not found.** (**Error! Reference source not found.**) shows the proposed circuit for implementing the current source circuit [52].

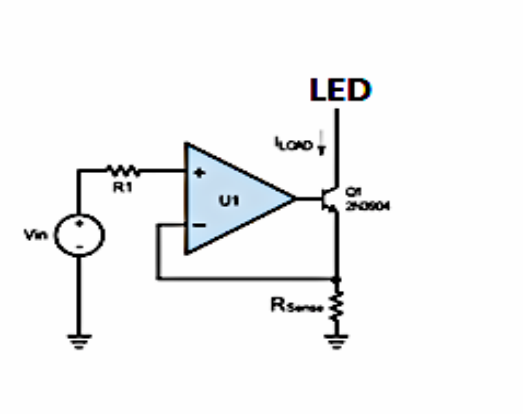

Figure 2-9 Voltage-controlled-current source driver.
This circuit is a classic form of linearized current source. The circuit is based on the common-emitter circuit. The output current can be adjusted by adjusting a Vin [52]

2.1.4 Time Domain and Frequency Domain NIR Source Multiplexing

In NIRS, more than one wavelength is often utilized. Therefore, the transmitted optical energy has to be measured at the receiver site, with respect to the particular optical source.

A mechanism is required to distinguish and separate the transmitted light at the receiver site, to accurately match to the origin light source. Multiplexing allows for the distinction of the transmitted light, according to its original source. There are several multiplexing methods.

2.1.4.1 Multiplexing in Time Domain

Multiplexing in the time domain is the most straightforward solution. Time-multiplexing is utilized in conventional pulse oximetry methods. Each wavelength is emitted to the tissue for a particular period of time, called a time frame, or cycle. A timer circuit switches between wavelengths periodically.

The ambient light and dark current of the photodiode may interfere with NIR sources. At one cycle, no light source is activated, and the device measures the summation of the photodiode dark current and ambient light interference [22].

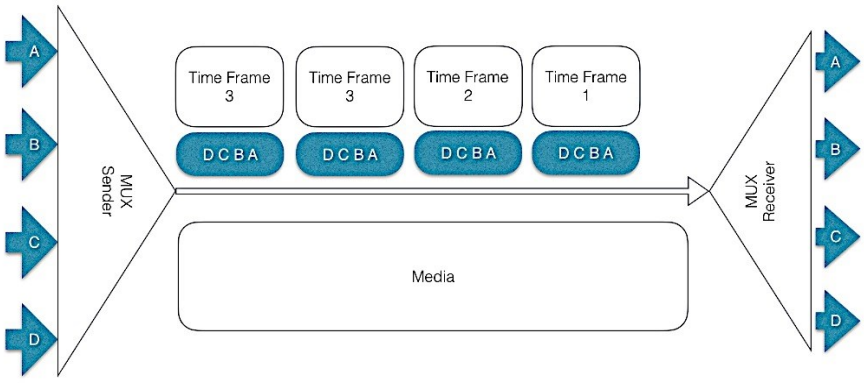

Figure 2-10 Time-multiplexing and demultiplexing.

The summation of the ambient light effect and the dark current of the photodiode is utilized for interference cancellation in the subsequent computations. The time multiplexing method is straightforward and easy to implement. Given that each light source is activated at each time cycle (time-frame), the total power consumption of the device decreases dramatically [22]. See Figure 2-10 (above).

2.1.4.2 Multiplexing in Frequency Domain

Frequency multiplexing is another type of multiplexing that can be applicable to the design of the NIRS/EEG device. In the following explanation, the methodology is described for a single NIRS light source consisting of 4 wavelengths, although the same methodology might be used in scenarios with more than one NIRS light source. Frequency multiplexing is an uncommon

multiplexing method in NIRS; however, several investigations have been conducted in this area recently.

For multiplexing, the source intensity signals in the frequency domain, and the frequency spectrum of each signal must be displaced in the frequency domain. Amplitude modulation is proposed for shifting the signal in the frequency domain [53]. The signal is multiplied by a cosine signal, called carrier signal. The frequency of the carrier signal is the carrier frequency of the channel. All signal sources are multiplied by their carrier signals, shifted and systematically arranged in the frequency domain. See Figure 2-11 (below).

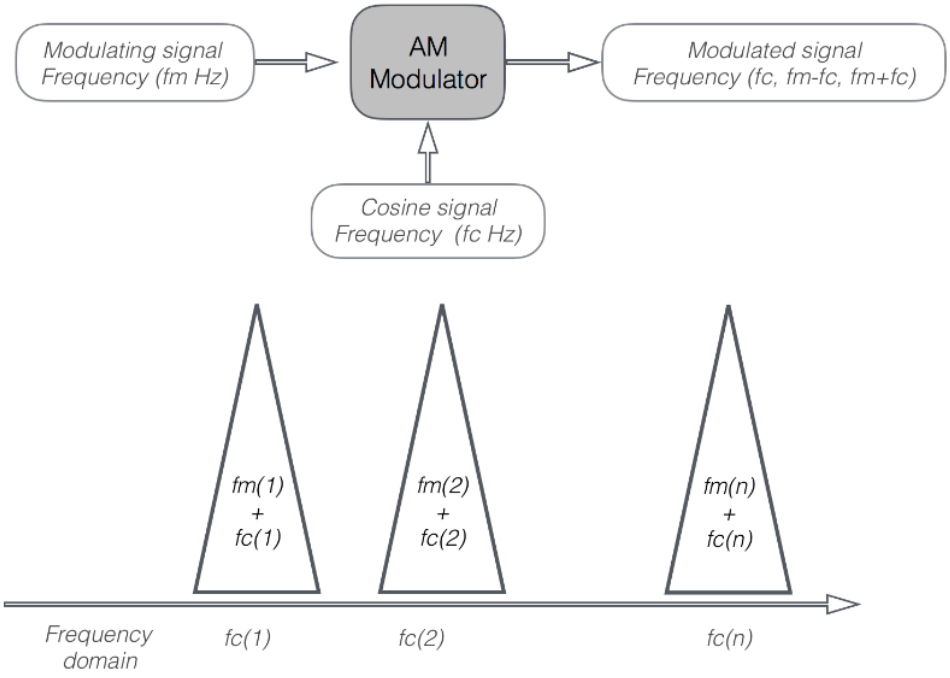

Figure 2-11 Frequency Division Multiplexing (FDM).
In FDM each source is modulated by a specific carrier frequency. Consequently, the spectrum of signal shifts in the frequency domain. The frequency channels are arranged with respect to their carrier frequency [53].

According to the superposition theorem, the output signal can be described as:

$$y_T\,(\mathrm{t}) = y_1\,(\mathrm{t}) + y_2\,(\mathrm{t}) .. + y_n\,(\mathrm{t}) \qquad \textbf{Equation 2-8}$$

$$y_T\,(\mathrm{t}) = \sum_{m=1}^{n} (x_m(t).\, c_m(t))$$

when:

$$\mathrm{c(t)} = \cos(\omega_c t + \theta_c) \quad \text{(Carrier signal)}$$

In Equation 2-8 (above), y_T is the superposition of all modulated signals, $x_m(t)$ is the modulating signal, and $c_m(t)$ is the carrier signal.

In designing the NIRS/EEG device, the time multiplexing method was not utilized. Alternatively, a frequency multiplexing method has been proposed and implemented. The principal reason for not using the time multiplexing method is the sensitivity of this method to changes in ambient light conditions during subject movement or minor changes in illumination. Changes in ambient light at low frequencies may contaminate the signal.

2.1.4.3 NIRS Light Source Modulation and Demodulation

In the NIRS/EEG design, each source is modulated based on the continuous wave amplitude modulation method. Each source has its own carrier frequency and so on the receiver's side, each source is separated from the other sources according to its specific carrier frequency.

WLA, WLB, WLC, and WLD are the respective intensities of four light wavelengths. A specific carrier frequency modulates the intensity of each light wavelength. Considering the

amplitude modulation shifts the spectrum in the frequency domain, a high-pass filter effectively eliminates all the ambient light and dark current of the recorded signal after pre-amplification. See Figure 2-12 (below).

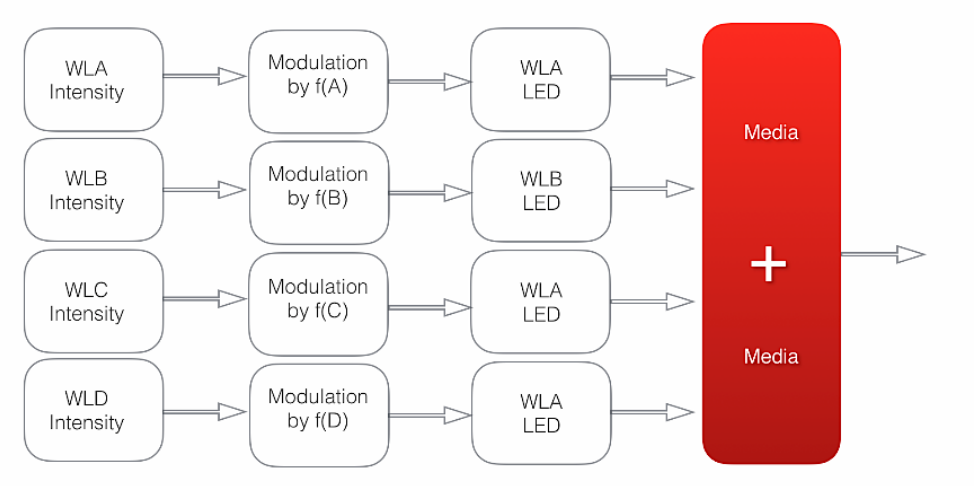

Figure 2-12 Modulation of sources in the NIRS/EEG optical source controller.
In this picture, the CW amplitude modulation is illustrated for one combined light source containing 4 wavelengths (WLA, WLB, WLC, WLD). A specific carrier frequency modulates the intensity of light at each wavelength (f(A), f(B), f(C), F(D)). The modulated intensities go through the LED current drivers. Eventually, the summation of modulated signals is delivered to the tissue accordingly. The continuous wave amplitude modulation has been developed for this method.

The carrier frequencies are selected sparsely and at a distance from each other to eliminate the possible interference between each two channels. Carrier frequencies of 1.5KHz, 15KHz, 54KHz, and 85KHz are determined for f(A), f(B), f(C), and f(D). A precise digital synthesizer (AD9833, 24bit D/A resolution, SPI interface, 0.004Hz frequency resolution) generated the cosine carrier signals.

All the wavelength intensities are modulated at specific carrier frequencies and applied to the tissue (media). Since there is only one medium to transport the energy, the summation of all modulated optical signals travel through the tissue. See Figure 2-12 (above).

$$I_{0=} \sum_{\mathrm{m}=A}^{\mathrm{D}} I_m e^{-i\omega_m t} \qquad m: A, B, C, D \qquad \textbf{Equation 2-9}$$

In Equation 2-9 (above), I_0 is the incident light; I_m is the intensity of the corresponding wavelength, $\omega_m$is the angular carrier frequency for wavelength (A, B, C, D), and *t* is time.

Consequently, at the receiver site, the optical receiver should be able to detect all the wavelengths (A, B, C, D). The receiver detects the transmitted portion of incident light at the receiving site. Based on Beer-Lambert's law, the transmission of light by a particular medium is modeled by a linear transformation, and the frequency of the applied optical signal does not change significantly during transportation.

When considering the Beer-Lambert law and the linearity assumption for medium transmission, the transmitted signal, consisting of four modulated intensities, can be expressed by the following equation:

$$I_0 = \sum_{m=\mathrm{A}}^{D} (I_m\, e^{-i\omega_m t}).\left(e^{\alpha_m c_m(\mathrm{t})\, d}\right)\ m: A, B, C, D \qquad \textbf{Equation 2-10}$$

In Equation 2-10 (above) I_0 is the incident light, I_m is the incident of each wavelength, and is ω_m the angular carrier frequency for wavelength m, and *t* is time. In addition α_m is the extinction coefficient of the compound and c_m is the concentration of the absorbent compound, and d is the distance.

$$I_{Total} = I_0 + I_{AN(DC)} + I_{AN(ac)} + I_{AN\,(others)} \qquad \textbf{Equation 2-11}$$

In Equation 2-11 (above), I_{Total} is the total light intensity that is delivered to sensor at the receiver site. I_{Total} can be considered a summation of I_0 (the modulated intensity of NIR sources); $I_{AN(DC)}$, the low-frequency components of ambient light noise (like sunlight and LED lamps); $I_{AN(ac)}$, the AC component of ambient light in the power line spectrum, and $I_{AN\ (others)}$, the other disturbing ambient light components.

By considering the superposition theorem and the linearity of the light transition function, the summation of four principal components encountered in the photodetectors is estimated. The summation can be decomposed into the principal components by applying a band-pass filter to the receiver signal.

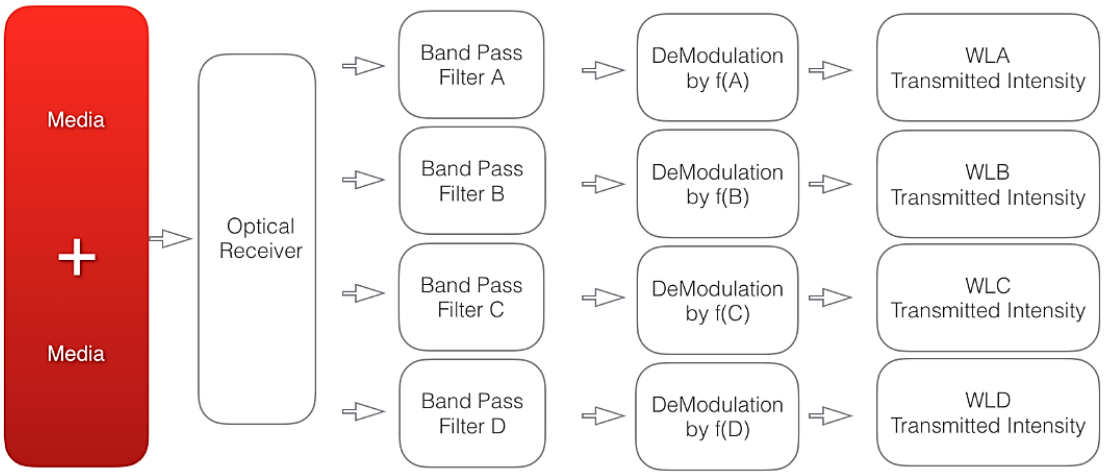

Figure 2-13 The estimation of each wavelength intensity at the receiver point.
The optical receiver receives the summation of all wavelengths; the band-pass filters decompose the summation into four components based on their carrier frequency. After demodulation, the intensity of transmitted light for each wavelength is estimated.

Every receiver has four band-pass filters. Therefore, for a number of 10 receiver channels, 40 band-pass filters need to be implemented. Software development of band-pass filters is not

proposed in this design. Rather, a hardware implementation was used. The first reason for choosing a hardware implementation is the number of channels being used. The implementation of 40 band-pass filters in software would be very costly and time-consuming. The other motivation is the high sampling frequency. Modulation by the carrier frequency shifts the spectrum of the signal, and the sampling frequency needs to be at least double the maximum frequency of the signal. Consequently, the sampling rate increases dramatically. To avoid a high sampling rate and computation time, analog implementation of band-pass filters is preferable. Second-order Sallen-Key low-pass and high-pass filters are determined to implement a full band-pass filter [52]. See Figure 2-14 (below).

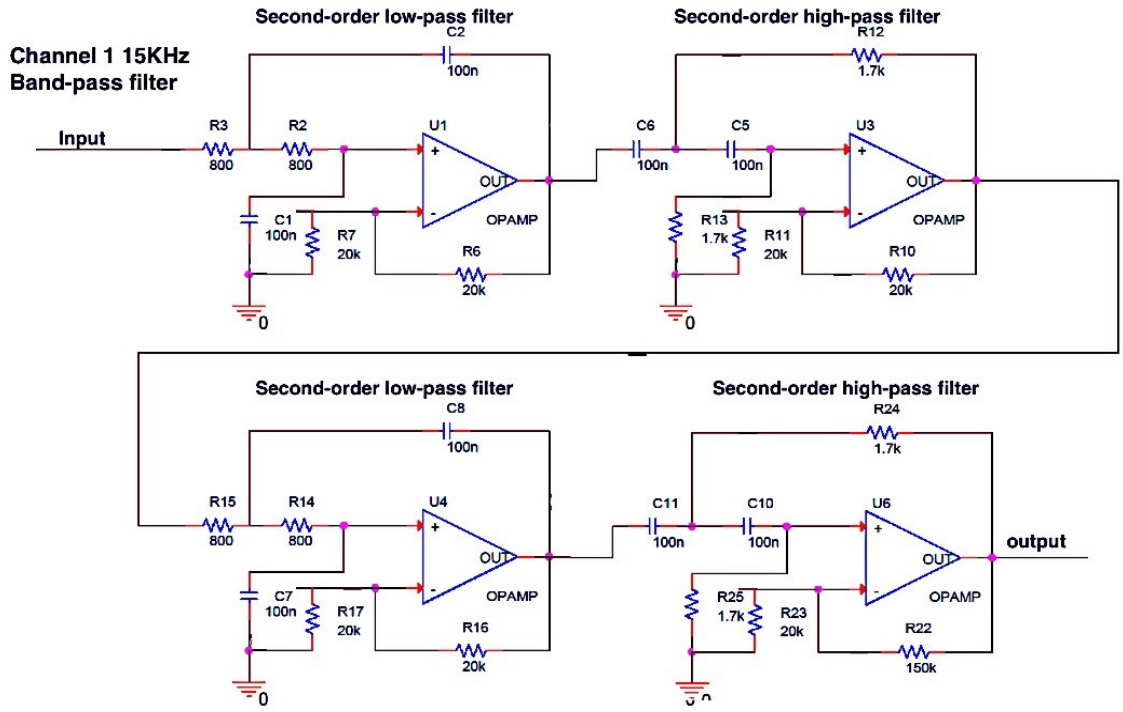

Figure 2-14 Sallen-key configuration filter circuit.
A Sallen-key configuration filter circuit has been proposed for implementing analog band-pass filters. Each band-pass filter consists of two, second order low-pass and high-pass filters. In this particular case, the band-pass filter has been centered at 15KHz.

By using band-pass filters, the received signal is decomposed into four principal components. Each component is related to a particular light wavelength. The band-pass filter not only decomposes the received signal into four principal components, but also separates the signal from ambient interference signals. The ambient light interference, generated from low-frequency light sources (sunlight, LED lightening lamps), 50Hz-lightening lamps, and electromagnetic interferences, are excluded from the primary signal in this method.

2.1.4.4 Evaluation of Amplitude Modulation Method

Theoretically, the noise increases as the frequency of the signal decreases and approaches DC. In analog circuits, the noise level of the op-amp is proportional to *1/f*, where *f* is input frequency. The light measurement may be disrupted by changing ambient light conditions.

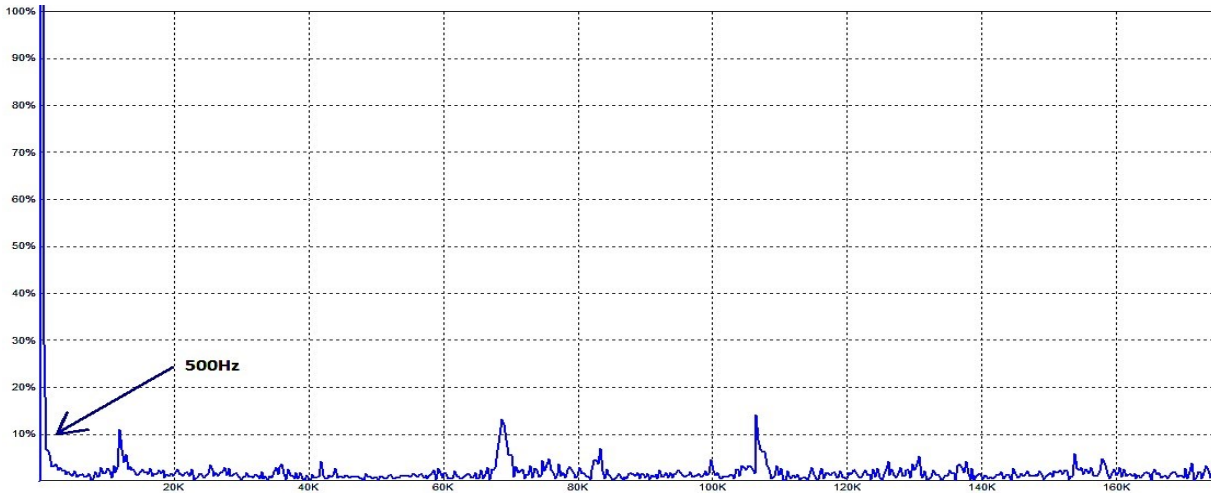

Figure 2-15 Ambient light spectrum.
This picture illustrates the spectrum of ambient light in laboratory conditions, as measured and computed by a spectrum analyzer. The vertical axis is relative amplitude in percent (%), and the horizontal axis is the frequency (Hz).

Choosing a measurement frequency distinct from the low-frequency noise improves the signal-to-noise ratio, allowing detection of weaker signals. Modulating the NIR light source

signal at an appropriate frequency facilitates measurement of scattered light that would otherwise be buried in noise.

An analog circuit implementation has been proposed for implementing the NIRS frequency multiplexing technique. The principal advantage of analog implementation is fast processing time. The processing of analog implementation can be considered as online processing with an almost negligible delay time. On the other hand, since the carrier frequency of modulation in some channels are 15KHz, 67KHz, 300KHz, the digital sampling of the analog signal for numerical and software implementation needs to be remarkably faster in comparison with analog implementation. The faster digital sampling of the analog signal can generate a greater amount of data however analog to digital converter hardware increases the cost of the device.

In the analog implementation of the NIRS frequency multiplexing technique, the Sallen-key configuration has been proposed for band-pass filters. The Sallen-key band pass filter attenuates the effect of low-frequency ambient light noise and as well as other modulated NIR sources.

The numerical and experimental analysis were performed for validating the effectiveness of the NIRS frequency multiplexing technique. In the numerical method, the circuit was simulated by PSPICE and ORCAD 2012. The frequency response of the circuit was estimated and illustrated in the figure. The Sallen-key band pass filter attenuates the effect of ambient light low-frequency noise. According to numerical simulation, the minimum attenuation for 60Hz is -59dB and for 1Hz is -200dB. See Figure 2-16 and Figure 2-17.

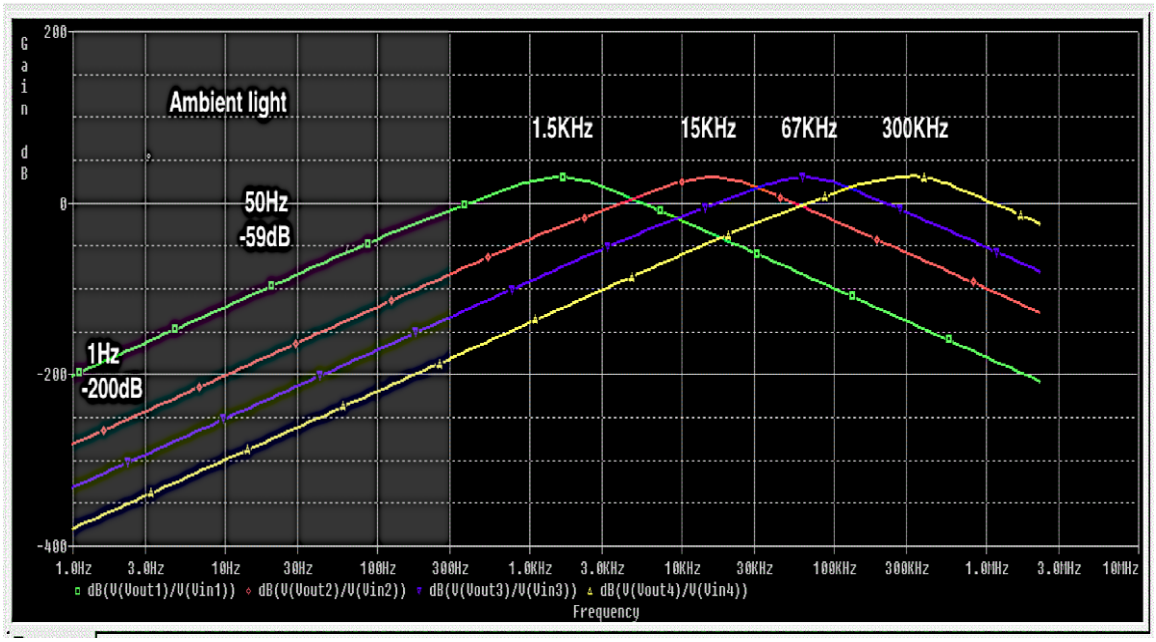

Figure 2-16 Frequency response of circuit (Gain in dB).
The vertical axis represents the gain of analog filters in dB; the horizontal axis represents frequency. Since most of the ambient light is positioned in DC to 500Hz bandwidth. Filters eliminate most of the ambient light. The circuit is modeled by PSPICE and ORCAD 2015.

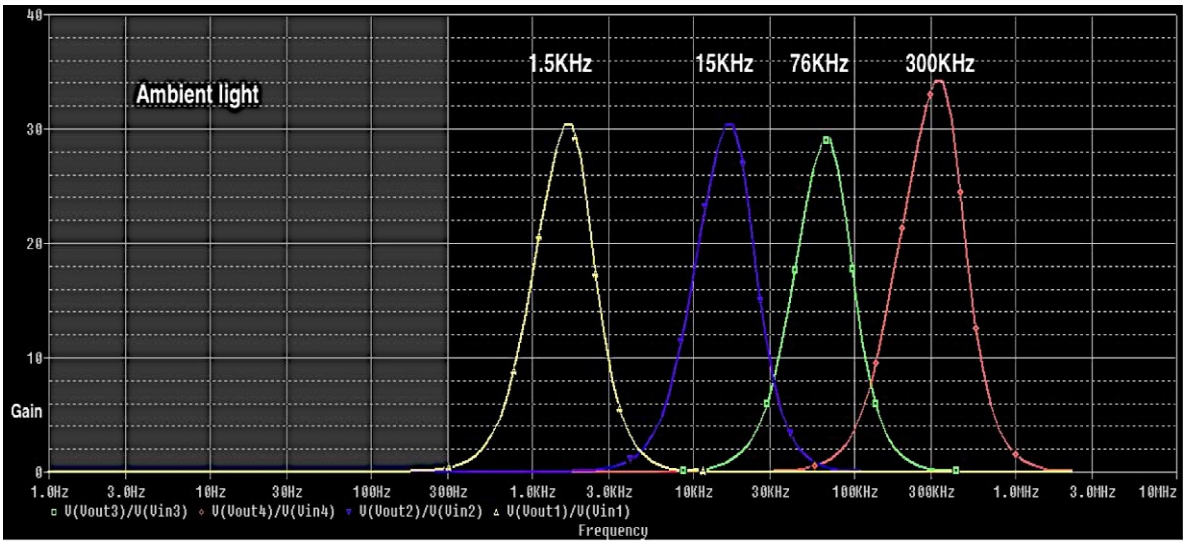

Figure 2-17 Frequency response of circuit.
The vertical axis represents the gain of analog filters. The frequency response of four Sallen-Key band-pass filters are depicted.

In experimental validation, we simulated the condition of ambient light. We intentionally contaminate two known 1Hz and 0.1Hz sinusoidal signals by simulating ambient light and then evaluate the effectiveness of the method to eliminate theambient light noise. The ambient contamination factor was simulated by white noise with the frequency within the 0.016Hz 500Hz bandwidth. The intention was to compare the SNR of the output signal both with and without use of the modulation method.

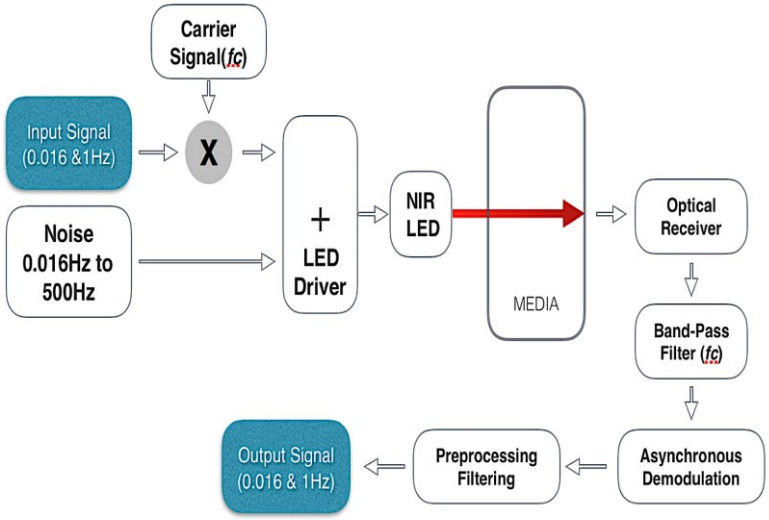

Figure 2-18 The experimental test method.
The input signal (considered 0.1 or 1Hz) was modulated and then mixed with the white noise (0.016Hz to 500Hz), which represents the ambient light conditions. The signal then went through the LED driver and was transmitted through the media. In the receiver site, the signal was detected and filtered by using proposed band-pass filters.

The light source and the light detector were fixed on a synthetic medium, made of multilayer transparent plastic. A Microcontroller (ATXMEGA 128) was acquired for simulating NIRS and ambient light. The signals were synthesized, modulated and converted to a voltage by using its internal digital to analog converters. The intensity of light was considered as 0.1Hz and 1Hz sinoside signals. The intensity signals were modulated by using 1.5KHz, 15KHz, 67KHz, 300KHz carrier signals. For simulating the ambient light noise, a white noise with spectrum

between 0.016 to 500Hz were added to the modulated intensity signal. The amplitude of ambient contamination signal was adjusted properly to approach the desired SNR (50%) for an input signal. See Figure 2-18 (above).

Table 2-4 (below) represents the result of the measurement. The SNR of the signal was adjusted to 50%. The SNR of the signal was measured with and without using the modulation method with respect to the input signal. The SNR improves by increasing the modulation frequency. A dramatic improvement of SNR signal can be observed by using the amplitude modulation technique.

Input signal Frequency	SNR of input signals simulated by Microcontroller %	SNR Without Amplitude Modulation %	Amplitude modulation	
			Mod Frequency	SNR %
0.016Hz	~50	~75 < SNR < ~75	1.5KHz	~88 < SNR < ~92
0.016Hz	~50	~75 < SNR < ~74	15KHz	~89 < SNR < ~94
0.016Hz	~50	~75 < SNR < ~82	67KHz	~87 < SNR < ~93
0.016Hz	~50	~75 < SNR < ~82	300KHz	~88 < SNR < ~93
1Hz	~50	~78 < SNR < ~84	1.5KHz	~89 < SNR < ~92
1Hz	~50	~78 < SNR < ~84	15KHz	~89 < SNR < ~95
1Hz	~50	~78 < SNR < ~84	67KHz	~88 < SNR < ~93
1Hz	~50	~78 < SNR < ~84	300KHz	~89 < SNR < ~93

Table 2-4. Comparing two methods.
The table shows the SNR of the output signals with and without amplitude modulation. The results are estimated for two signals, 0.016Hz and 1Hz signals, as the inputs. The input signals were generated using a microcontroller. The output signals were measured using a digital oscilloscope (Rigol DS1052) and exported to the MATLAB 2012. The SNR of the signal was then estimated accordingly.

Figure 2-19 (below) illustrates the measurement that has been conducted under real conditions. The position of optodes was on the forearm. Two NIR sources modulated at different carrier frequencies have been activated. The first signal shows the summation of two modulated NIR sources and ambient noise. The signal traveled through bandpass filters and was

decomposed into two signals. As it is shown in this figure, in the decomposed signals, SNR is improved dramatically.

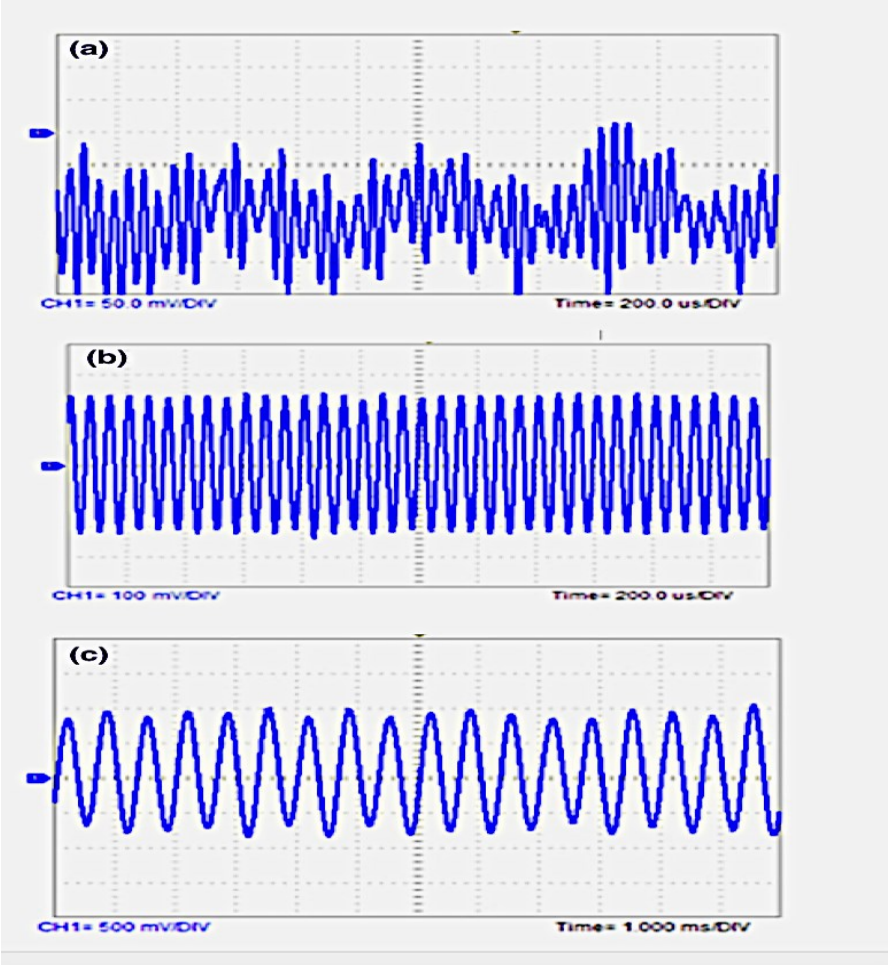

Figure 2-19 Amplitude modulation technique and signal decomposition.
This signal is measured under real conditions; Two NIRS sources are activated at two carrier frequencies (1.5KHz and 15KHz). The first signal (a) is the amplification of photodiode output. This signal is a summation of two modulated NIR sources and ambient noise.

The signals that are depicted in (b) and (c) are decomposed from main signal (a) by using proposed method. It can be seen that the level of noise is dramatically reduced in signals (b) and (c).

The data is measured and exported by a digital oscilloscope (Rigol DS1052). The position of NIRS optodes was on the forearm, and the experiment was conducted under laboratory illumination conditions.

2.1.4.5 Advantages and Limitations of Using Continuous Amplitude Modulation for Multiplexing NIR Sources

The primary advantage of this method is its ability to eliminate ambient light artifacts. When using amplitude modulation multiplexing, the NIRS instrument is not sensitive to artifacts from changes in low-frequency illumination that may occur during subject movement and changes in surrounding ambient light. The 60 Hz illumination artifact is eliminated by the band-pass filters. The frequency multiplexing method allows us to shift the spectrum of the NIRS signal to the right band, and eliminate unwanted destructive noises by applying a band-pass filter.

The amplitude modulation technique has some drawbacks. Since the light sources emit the light concurrently, the total optical energy delivered to the tissue is increased. In future work, by using a combination of time multiplexing and amplitude modulation methods, the total optical energy can be controlled and effectively reduced. Inter-source interference might also be a source of error in NIRS. As previously mentioned, several wavelengths are activated at the source; a particular carrier frequency modulates each wavelength. The received signal is the summation of all the sources that are applied to the tissue under investigation. In order to decompose the summation signal into its principal components, a band-pass filter is determined and implemented. The band-pass filter is not ideal, as a small portion of the signal may leak through.

2.1.5 Transmittance and Reflectance Probes

The incident light emitted by LEDs may be partially absorbed, transmitted, or scattered by tissues and tissue components such as skin, blood, protein, and fat before being detected by the receiver. The intensity of the signal at the receiver site is inversely proportional to the square of the distance; all inter-optode distances and directions must be fixed under proper conditions. In

some applications, the NIRS optodes are conveniently situated in a solid structure so that their relative distance and directions remain unchanged. Transmittance probes are mostly employed in pulse oximetry, when they are positioned on opposite sides of the tissue. There is a direct path between the source and the sensor in the media; therefore, some of the light may be absorbed or scattered away, and eventually, a some of the incident light is transmitted through the tissue and meets the photodetector.

When using reflectance probes, there is no direct path between sender and receiver, and the scattering effect causes the incident light to bend inside the media, return to the surface, and approach the photodetectors. See Figure 2-20 (below).

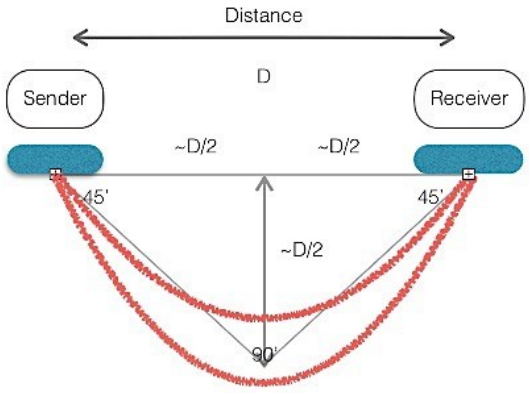

Figure 2-20 The path of light in reflectance probe.
The path of light in the reflectance probe. The light travels through a banana-shaped path. According to recent studies, the depth of penetration is about half of the inter-optode separation distance[28].

Transmission of light at a particular wavelength within the tissue is determined by the combination of three major factors: reflectance, scattering, and absorption. Reflectance is according to the angle of the light beam and the regularity and smoothness of the surface tissue. The reflection decreases with increasing wavelength. Therefore, this effect is far less in NIR relative to visible light. The scattering phenomenon is mostly related to the tissue composition

and tissue interface layers. However, absorption is a function of molecular properties of substances within the light path [8].

2.1.6 Light Source and Sensor Placement

We proposed to place both EEG electrodes and NIRS optodes on the forehead, by designing a dedicated probe, and positioning the electrodes and optodes in a specific arrangement. The electrodes must be placed in such a way that the device is capable of recording signals from the gray matter of the brain, below the forehead.

Increasing the inter-optode distance results in a greater sampling area, with incident light samples from deeper areas of the tissue. A greater sampling area results in less spatial resolution. In addition, extending the inter-optode separation means that there is a longer path of sampling, and consequently, less light energy reaches the photo detectors. Similarly, decreasing the inter-optode distance generates smaller sampling areas. Therefore, the incident light samples more shallow areas, and spatial resolution improves. A small sampling area means a shorter area of sampling, and more photons can be detected on the receiver side. Considering the interaction of inter-optode spacing, path-length, spatial resolution, and intensity of light at the receiver point, there should be a trade-off among these parameters. In many investigations, a distance of 30mm has been proposed for inter-optode separation. The depth of penetration, empirically, is considered to be half of the inter-optode distance [28].

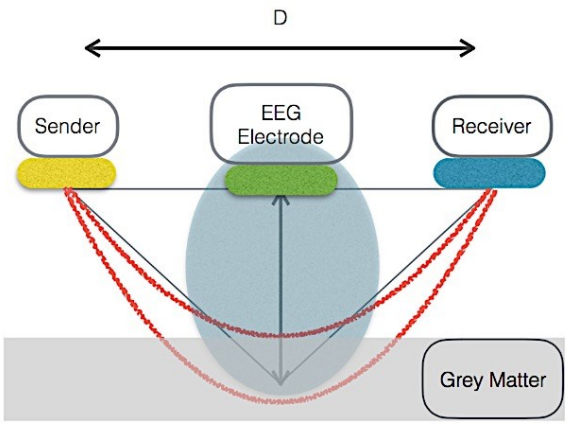

Figure 2-21: The placement of EEG electrode in between receiver and sender.
The positioning of EEG electrodes in between optodes maximizes the conjoined sample area of EEG electrodes and NIRS optodes at the gray matter area of the brain.

The EEG electrodes are positioned in between optodes, to record the neurophysiological activity of the neurons. Positioning the EEG electrodes in between optodes maximizes the conjoined sampling area of EEG and NIRS optodes in the gray matter of the brain. See Figure 2-21(above).

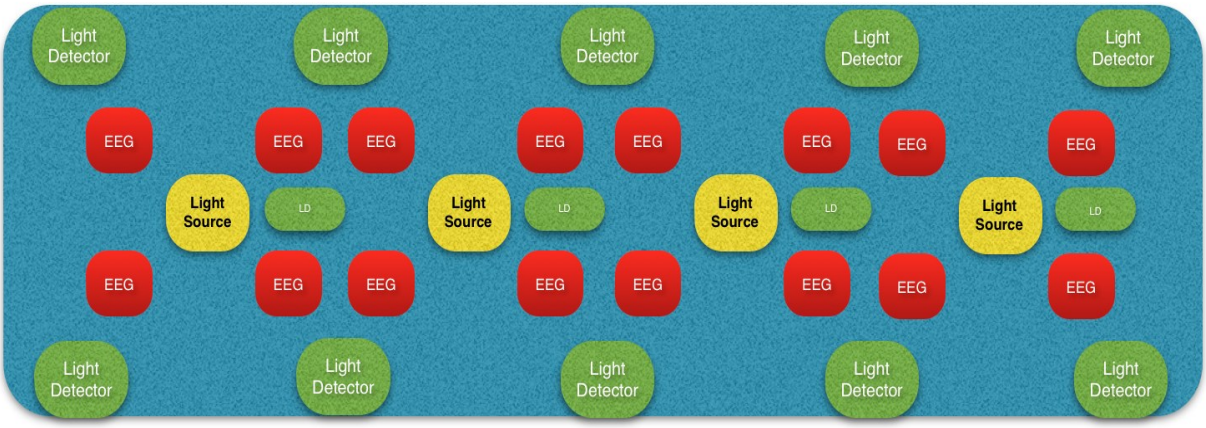

Figure 2-22 The arrangement of EEG and NIRS optodes in the forehead.
There are ten light detectors, signaled by the green color, four light sources, and sixteen EEG electrodes.

The EEG electrodes and NIRS optodes are positioned on a flexible, printed circuit. There are four sources; with each source consisting of four wavelengths. Ten photo-detectors are positioned around the sources. The inter-optode separation distance is specified to be 28mm in this design; 16 EEG electrodes are positioned in between optodes. See Figure 2-22 (above).

Figure 2-23 Implemented NIRS/EEG probe.
This picture depicts the implemented NIRS/EEG probe. The EEG electrodes and NIRS trans-amplifiers are positioned in the probe. For the comfort of the subject, the FPCB has been covered by soft materials.

The implementation of the proposed arrangement is illustrated in Figure 2-23. A flexible platform is designed to fix the electrodes on the forehead; the inter-optode distance may not be significantly changed. The probe can be connected to the amplifier, and the light source controller by two flexible ribbon cables. For monitoring, the entire probe is secured to the forehead by an elastic band. See Figure 2-22 and Figure 2-23.

2.2 The Method's Advantages Constraints, and Source of Errors

The objective of this section is to specify some sources of error in near-infrared spectroscopy that may produce uncertainty in measurements. Recognizing the constraints and limitations of the described methods in this section, as well as the application of appropriate interventions is essential to optimize and enhance the design, and inform the methodology of future investigations.

2.2.1 Scattering and Absorption of the Tissue

In diffused NIR spectroscopy (reflectance probes), the sensors measure the light that is reflected through the banana-shaped trajectory and encountered by the sensors. Based on the transmitted signal, the absorbed and scattered part of the original signal has to be estimated. The attenuation of incident light depends on two primary parameters, namely, scattering and absorption. Increasing any of these two parameters results in the decrease in the recorded signal [28]. The origins of scattering variations within the brain have only been partly discovered. For example, scattering may be higher in areas with compact fiber tracts. Most NIRS monitoring experiments assume that scattering remains relatively uniform throughout investigation of the tissue of interest, and that all detected signal variations are attributable to fluctuations in absorption. This assumption may be one of the limitations of the method. In the presence of any

cause that affects the change of the scattering rate, the NIRS computation may yield uncertain results [28, 50].

2.2.2 Effect of Ambient Light

Ambient light can be a significant disturbing factor to Near Infrared Spectroscopy. Sunlight and LED lights regularly generated light in low frequency (near to DC). However, 60Hz-lightening lamps create ambient light at about 60Hz in the frequency domain. Considering the nonlinear effect of the lightening devices, the power spectrum of the disturbing ambient light may be extended to more than 60Hz. The body surface is nearly opaque under ambient light, although some portion of the ambient light may be diffused and approach the light sensors. In addition, the movement of the body may change the direction of ambient light, thus generating an unwanted effect on NIRS signal. By using the modulation method, most of the ambient light components can be removed from the received signal by using the band-pass filters, centered at carrier frequencies. If significant ambient light encounters the photodiode, it may saturate the preamplifier [22].

2.3 Design, Implementation, and Prototyping

The device consists of three major sections:

- Brain Near Infrared Spectroscopy (NIRS) component
- Electroencephalography (EEG) component
- Data acquisition system

2.3.1 The Block Diagram of Near Infra-Red Spectroscopy Hardware

The NIR section consists of LED light sources. Each LED consists of four wavelengths (740nm, 780nm, 850nm, and 950nm). The NIRS photodetectors gather the light energy that is generated by the incoming light sources. The EEG section consists of EEG electrodes that acquire the summation of neuronal activities in specific areas of the brain. The EEG signal passes through the low-noise high-common-mode-rejection-ratio preamplifier [54]. After amplification and pre-processing, all the signals are converted to digital form and are transmitted to a computer using a high-speed USB 2.0 (680Mb/S). See Figure 2-24 (below).

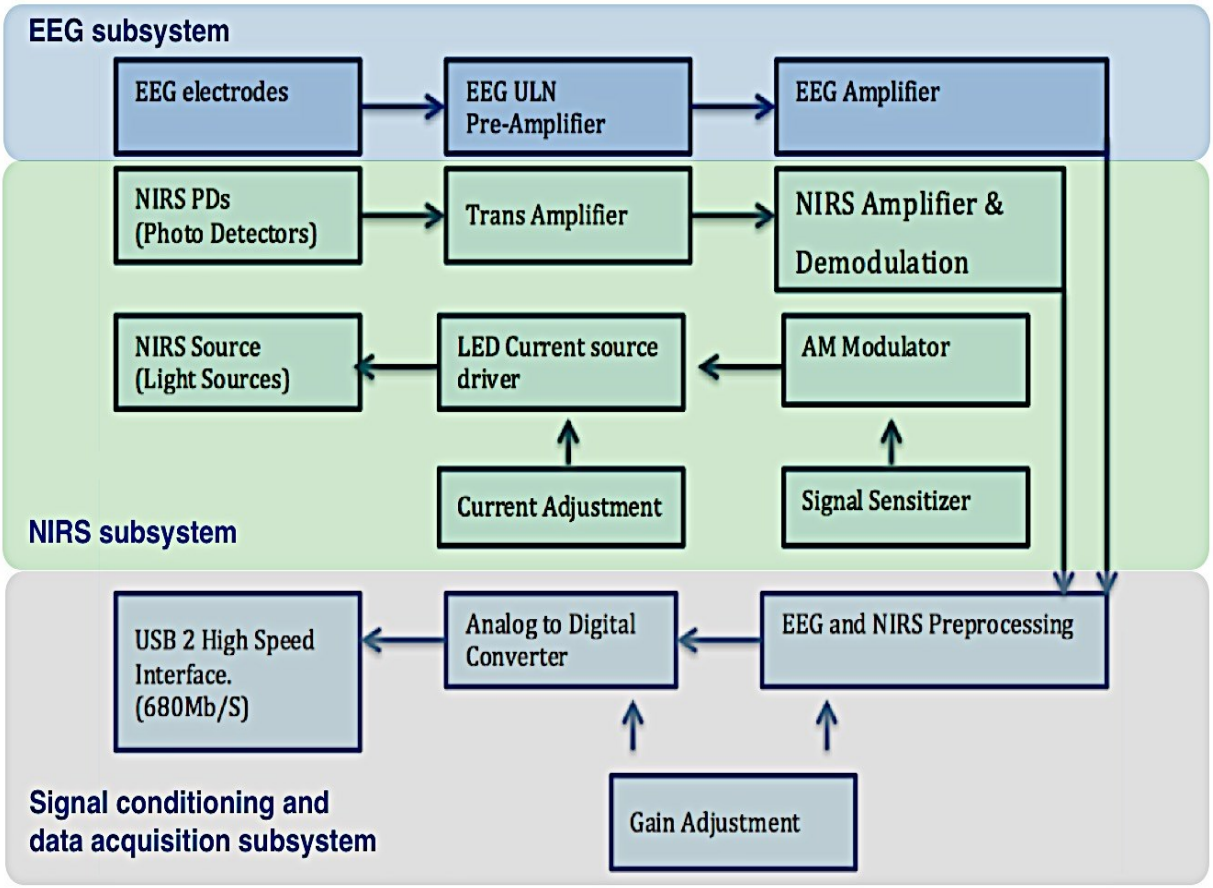

Figure 2-24 The block diagram of the NIRS/EEG device.

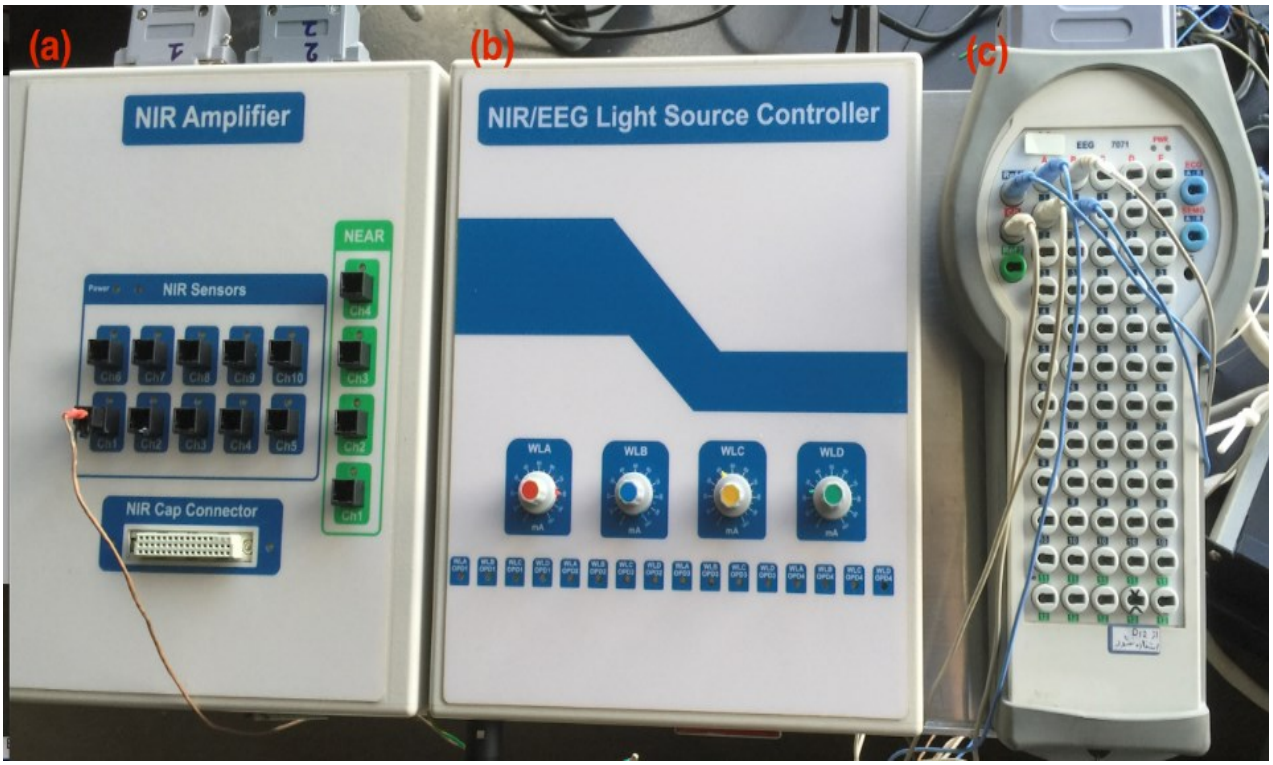

Figure 2-25 The implemented NIRS/EEG prototype.
a) The NIRS amplifier enclosure includes the amplifier, band-pass filter and demodulator modules (Implemented in this study as part of the NIRS/EEG device). b) The NIRS/EEG light source controller includes the source modulator, source drivers, and intensity adjustment modules (Implemented in this study as part of the NIRS/EEG device). c) The EEG amplifier is for recording EEG signals. (Device from Zoya Bastany and Guy Dumont (2015), UBC, 2015 [1])

2.3.2 EEG Amplifier

The EEG component of the system is based on the investigative work of Zoya Bastany, Prof. Gorji and Prof. Guy Dumont [1]. The novel ultra-low-frequency EEG amplifier was initially tested in animal subjects. According to the results, the device was able to record the data in the 0.01 Hz to 120 Hz frequency band[16].

2.3.3 Conclusion

The NIRS/EEG instrument design process has been reviewed in this chapter. The design process began with the evaluation of different methods and components. For detecting NIR at the

receiver site, a photodiode was proposed, and LED was proposed as a light source. The sensitivity of photodiodes is appropriate for recording the signal on the forehead.

However, on the hairy part of the scalp, SNR of the NIRS of the signal was not sufficient. Future investigations may determine if using APD photodetectors may enhance the sensitivity of recording in such cases.

In order to position EEG electrodes and NIRS optodes, a custom NIRS probe has been designed and implemented. In NIRS probe implementation, a multi-layer ultra-flexible printed circuit was used. The NIRS subsystem is capable of using four wavelengths concurrently, although in the investigations described within this thesis, two wavelengths were used. Instead of the conventional time multiplexing method, the frequency multiplexing method has been used in designing this device. The most significant advantage of the frequency multiplexing method is the elimination of the sensitivity of the device to ambient light noise. A hardware implementation has been proposed for prototyping the frequency multiplexing method (amplitude modulation). The Sallen-key band-pass filter has been centered at the carrier frequencies. The effectiveness of the method has been examined by using numerical and experimental methods. Ultimately, the NIRS subsystem was combined with a low-frequency EEG device and connected to a data acquisition system.

Chapter 3: NIRS/EEG Validation

In this section, we discuss several experiments that have been conducted using the NIRS/EEG device. The device used during these experiments is comprised of two major components; one pertaining to EEG, and one pertaining to NIRS.

The EEG component of the system is based on the investigative work of Zoya Bastany, Prof. Gorji and Prof. Guy Dumont (2015). The novel ultra-low-frequency EEG amplifier was initially tested in animal subjects. According to their results, the device was able to record the data in the 0.01Hz to 120Hz frequency band. It has been determined that Ag/AgCl electrodes are optimal for recording EEG within the specified frequency band [55], and therefore we used the same EEG amplifier in the aforementioned experiments.

Before the commencement of any experiments, the signal was analyzed to verify the operation of the NIRS/EEG instrument and its functionality in collecting both DC and AC optical densities. The sensitivity of the device to ambient light was also verified.

Three experimental conditions were studied: The Forearm Arterial Occlusion test, the Cold Pressor Test (CPT), as well as testing under hypoxic conditions.

The Forearm Arterial Occlusion Test is a reliable method for primary validation of NIRS devices, and confirms the functionality of the instrument. In the second experiment, we recorded

NIRS and EEG signal during Cold Pressor Test (CPT) condition. The aim of this study was to investigate the variation of oxygenation and deoxygenation of the brain, as well as the level of gamma-band oscillations (30Hz to 80Hz) in EEG measurements collected during CPT. This experiment was proposed based on an investigation conducted by Z. Barati and K. Pourrezaee at Drexel University in 2012 [2]. In this experiment, we intended to measure the respective concentrations of oxy- and deoxy-hemoglobin using NIRS, and the source-modulation method. During this experiment, EEG was also measured across the full-bandwidth (0.015 to 120Hz).

The hypoxic breathing measurement was the third experimental condition produced as part of this study. In this experiment, we measured NIRS and EEG signals concurrently, during hypoxic breathing conditions. The ultimate goal of this experiment was to investigate the correlation between EEG and NIRS signal during hypoxia.

3.1 NIRS Recording During The Forearm Arterial Occlusion Test

The objective of the experiment is to validate the functionality and effectiveness of the proposed method and its implementation, in measuring HHb and HbO_2 using NIRS. In this experiment, the hemodynamic response to an arterial occlusion of the forearm of a healthy male subject was investigated. This procedure is a straightforward trial for the validation of NIRS instruments.

3.1.1 Material and Methods

Arterial occlusion was induced in the forearm by means of a pneumatic pressure cuff. The NIRS optodes were positioned on the forearm, below the pressure cuff, to monitor the oxygenation of the arm. The occlusion was imposed on the forearm for approximately 45

seconds. A single NIRS probe was used during this experiment. The probe was comprised of an LED emitting two wavelengths (λ_a = 740nm, [MTE1074N1-R, Marktech Optoelectronics] and λ_b = 850nm [TSHG6400, Vishay Semiconductors]) as the light source, and a photodiode (PDB-C160SM, 2.97mm x 2.65mm, Luna Optoelectronics) as the light detector.

The separation distance between the light source and light detector was 28mm. The NIRS optodes were secured firmly to the brachioradialis, using an elastic VELCRO® fastening band.

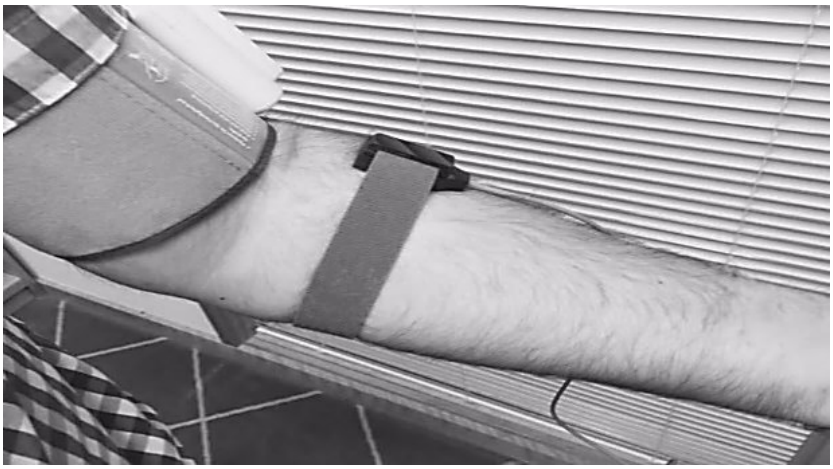

Figure 3-1 The positioning of NIRS probe on the forearm.
The separation distance (Source-Detector) of the optodes was 28mm. The source wavelengths were 740nm and 850nm produced by an LED, and the sensor was photo-detector (PDB-C160SM, 2.97mm x 2.65mm, Luna Optoelectronics). A pneumatic cuff was used to occlude blood flow in the arm. The occlusion was imposed for 45 seconds.

3.1.2 Results

The gradient of the chromophore variations, in this instance, is associated with local tissue oxygenation. When the cuff is released, the changes are reversed. A hyperemic response is observed due to auto-regulative mechanisms. In comparison to measurements taken from the brain, the absorption of light was higher; this higher absorption rate seems to be due to the

presence of different types of tissue chromophores. The result of this study is comparable to other similar experiments. See Figure 3-2 (below).

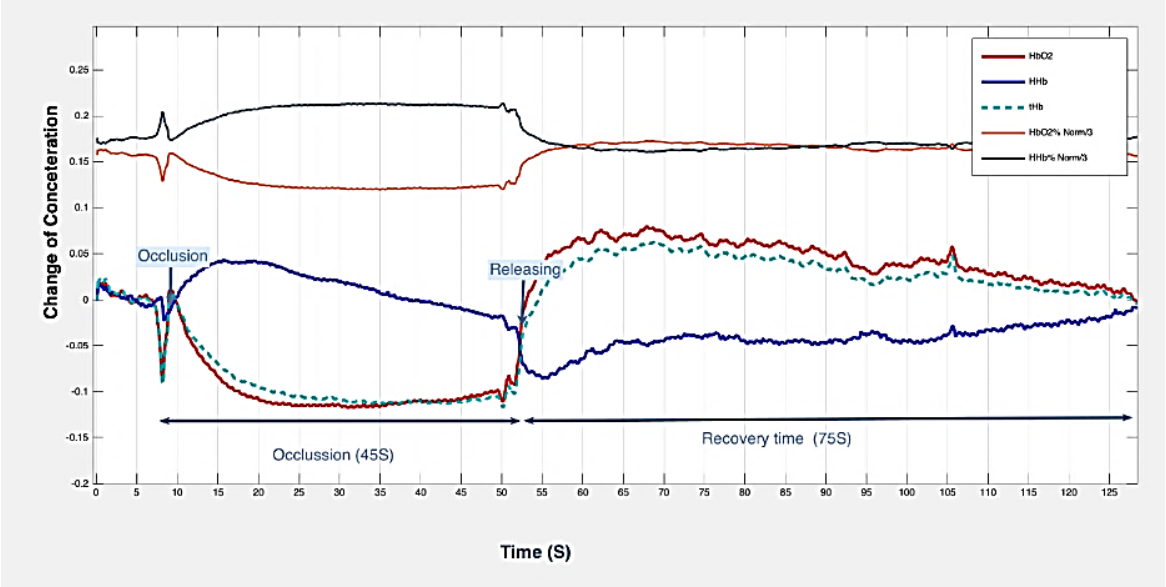

Figure 3-2: The change of HbO_2 and HHb during arterial occlusion.
Changes of blood chromophores (HbO_2 and HHb) during arterial occlusion are illustrated in this figure. The occlusion caused a very tiny artifact and was 45S in duration. Upon release of the cuff, HbO_2 and HHb returned to their original levels (Recovery time). (The Vertical axis represents the change of HHb, HbO_2. Total-Hb ; MicroMole/S);

3.2 Hemodynamic and Electrophysiologic Response to Repeated CPT

The cortical processing of the tonic pain caused by CPT has been studied in some neuroimaging studies. Several brain regions have been shown to be involved in the processing of noxious cold stimuli. Di Piero et al. 17 used a Xenon-133 inhalation single-photon emission tomography (SPET) to assess the cerebral blood flow in response to CPT [2], induced on the left hand. They witnessed increased activation in regional blood flow in the contralateral frontal lobe, bilateral temporal regions, and contralateral primary sensory cortex in the cortical region related to the hand.

The objective of our experiment was to assess the functionality of our NIRS-EEG device in recording the cerebral hemodynamic changes in response to CPT. A similar experiment has been previously conducted at the Biomedical Engineering Department at Drexel University (2012) [2, 56]; The test has been designed to confirm the results and check the functionality of the proposed method by utilizing the implemented prototype and comparing its results with a reference device, under similar conditions.

Ambient temperature and other external stressors are known to influence heart rate (HR) and blood pressure (BP). [57] The Cold pressor test (CPT) is a conventional procedure, broadly utilized across research disciplines involving psychological [57], cardiovascular, and neurological disorders. Wolf and Hardy were the first to introduce the application of the CPT to impose experimental pain in healthy subjects in 1941 [10, 11].

Abrupt and increasingly uncomfortable cold stress, as imposed during CPT, induces the extensive activation of the sympathetic nervous system and discharge of norepinephrine. These responses combine to increase BP. By increasing BP, we expect both THb and HbO_2 levels to increase in the tissue of the forehead[56].

3.2.1 Materials and methods

3.2.1.1 Principle and Instrumentation

In this experiment, we recorded both NIRS and EEG signals concurrently during CPT. The device was composed of two subsystems; EEG and NIRS. The EEG signals were recorded using the AC/DC-EEG amplifier designed by Zoya Bastany and Guy Dumont for recording low-frequency EEG at the University of British Columbia (2015). According to their results, the EEG

device is able to record signals across both ultra-low frequency and standard EEG bandwidths (0.015Hz to 120Hz). The NRSIGN EEG interfacing box and its accompanying software (NRSIGN, BC, Canada) were utilized in this experiment. The low profile Ag/AgCl (Cortech, AC-DC-AGE06 Diameter ~5mm) electrodes were chosen for the recording of EEG signals.

The NIRS hardware was implemented by utilizing the amplitude modulation technique for the purposes of eliminating the effect of ambient light during the experiment. The NIRS subsystem consists of light source controller, amplifier, and optodes. The light source controller is responsible for modulating the intensity of the light, and adjusting the radiated energy levels between 0.5mW to 1.5mW. The amplifier consists of trans-amplifier, demodulator and analog filters. The probe is relatively flexible and can easily be attached to the subject's forehead.

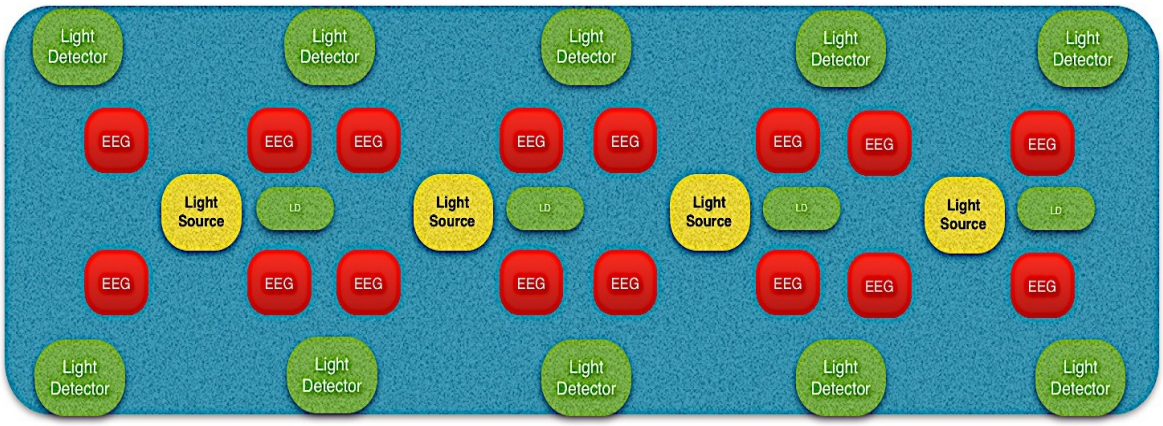

Figure 3-3. The arrangement of EEG and NIRS optodes in the forehead.
There are fourteen light detectors, indicated in green. Ten light detectors are placed around the perimeter, and four light detectors are positioned near to the light sources. Four light sources (each light source emits 740nm and 850nm), The distance between 'Far' optodes (source-detector) is 28mm, and the distance between 'near' optodes is 12mm. Sixteen Ag/AgCl EEG electrodes (Diameter = 4mm) are positioned in between the main NIRS optodes.

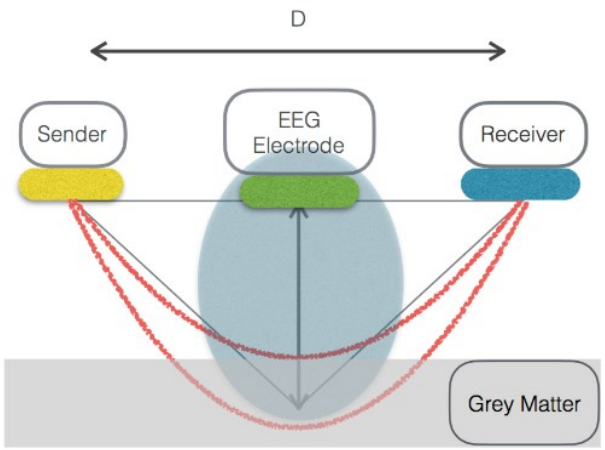

Figure 3-4: The placement of EEG electrode in between NIRS optodes.
The positioning of EEG electrode in between NIRS optodes maximizes the conjoined sample area above gray matter areas of the brain. The NIRS inter-optode separation distance is 28mm. The diameter of EEG electrodes is 5mm (Cortech, AC-DC-AGE06 Diameter ~5mm).

The prototype NIRS/EEG forehead probe has been used in this experiment. The light sources are LEDs emitting 740nm ((MTE1074N1-R, Marktech Optoelectronics) and 850nm (TSHG6400, Vishay Semiconductors) light wavelengths. These LEDs are integrated into a single package. The light sensors are (PDB-C160SM, Luna Optoelectronics). The NIRS sensors, light sources, and EEG electrodes are integrated as a single probe. See Figure 3-3.and Figure 3-5.

In addition, two additional individual EEG electrodes (Cortech, AC-DC-AGE06 Diameter ~5mm), B1 and B2, have been positioned on the portion of the probe that overlies the sensory cortex. A reference electrode was positioned on left ear. We utilized an Ag/AgCl electrode (Ambu® Neuroline 700, Ag/AgCl, disposable Solid Gel Electrode) as a reference electrode (on the left (43) ear and FZ (23) according to 10/10 EEG electrode placement. See Figure 3-6 (below).

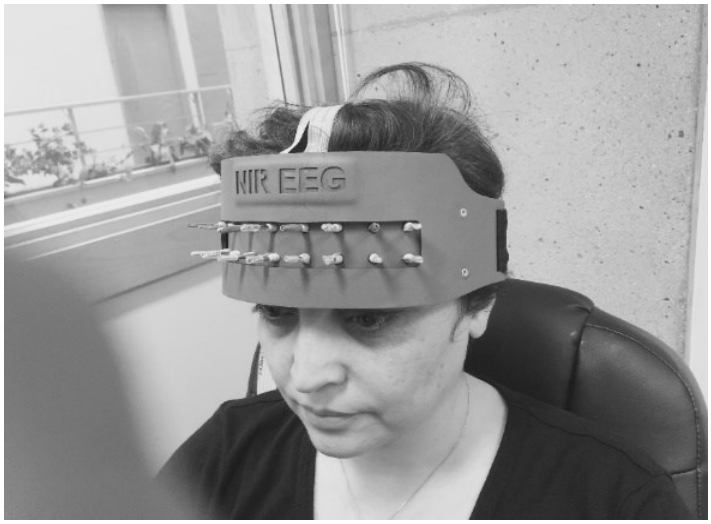

Figure 3-5 The probe integrates NIRS optodes and EEG electrodes.
The NIRS optodes and EEG electrodes are integrated into one probe. The probe "Cap" consists of 1) Four NIRS light sources, each including 740nm and 850nm; 2) Ten NIRS 'Far' light sensors with an inter-optode separation of 28mm; 3) four 'Near' light sensors with an inter-optode separation of 12mm; 4) Sixteen Ag/AgCl EEG (diameter ~5mm) electrodes are positioned in between the 'Far' NIRS optodes. Two ribbon cables connect the probe to the amplifier and light source controller.

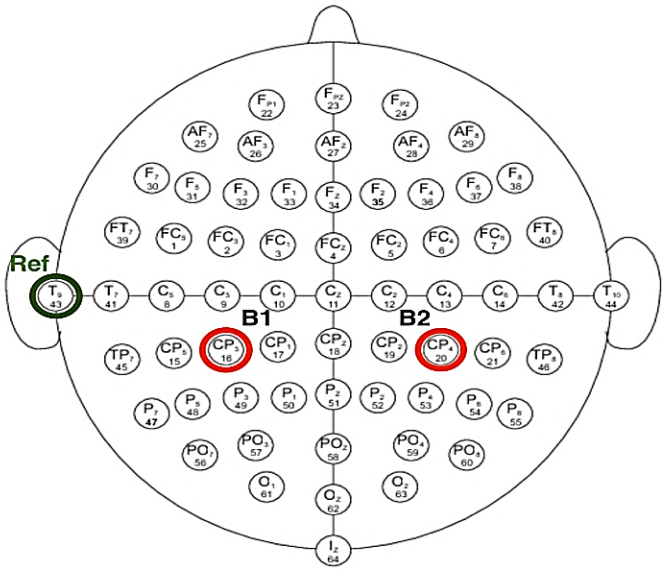

Figure 3-6 EEG B1, B2 electrode positions
EEG individual electrodes, B1, and B2 were positioned in CP3(16), and CP4(20) points to record the signal from somatosensory cortex. The reference electrode is labeled Ref (left ear). The position of the electrodes is according to the 10/10 EEG electrode positioning system [58].

3.2.1.2 Subjects

This study is an observational study, and five healthy volunteers between 20 to 50 years old, male and female, were enrolled. All participants gave written informed consent to participate.

3.2.1.3 Protocol

This experiment was conducted as part of a UBC CREB approved protocol to test non-invasive sensor prototypes developed by the Electrical and Computer Engineering in Medicine team at the Child and Family Research Institute in Vancouver, BC. The subjects were seated comfortably in an armchair. The probe was fastened symmetrically to the forehead of subjects as previously described. The optical density at two wavelengths (740 and 850nm), as well as the EEG signals were sampled at a rate of 512 samples per second. The conductive paste (Ten20, Weaver) was applied to the EEG Ag/AgCl electrodes on the probe, in order to minimize the skin-electrode impedance [55]. The experiment was conducted at room temperature (22~24 °C) and with the normal ambient light presence. The relative changes of HHb and HbO2 and Total-Hb were measured as hemodynamic variation parameters. The EEG signals were recorded concurrently. Two EEG-reference electrodes were used; one positioned frontally Z (23, 10/10 EEG electrode system), and the other one on the left ear (43, 10/10 EEG electrode system) [58].

The experiments began with two minutes of baseline recording, followed by immersion of the left hand up to the wrist into ice water (~0 °C) for 120 seconds, followed by 120 seconds of recording at rest, after removal of the limb from the ice water (22~24 °C). This process repeated for three times. The process of experiments is illustrated in Figure 3-7 (below)

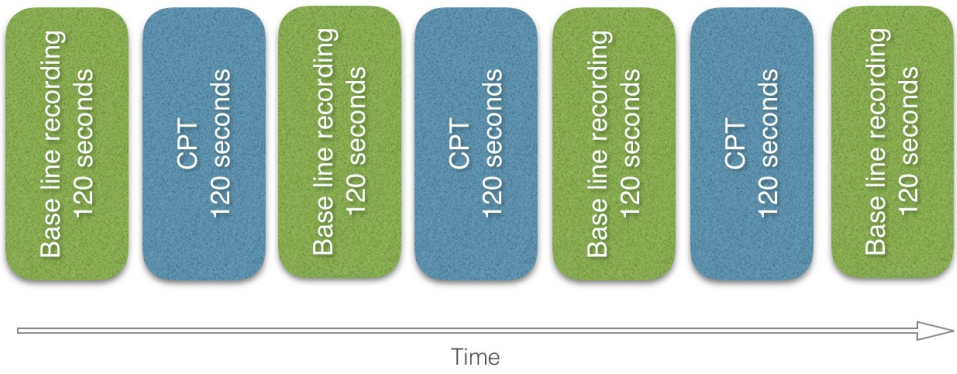

Figure 3-7. The timing diagram of the CPT experiment.
The experiment starts with 120 seconds baseline measurement at rest condition. The cold pressor test is imposed for 120 seconds. During the recovery time, the subject's hand was out of cold water and exposed to room temperature. The CPT and baseline recordings were iterated three times,(We considered to conduct experiment with 60S CPT duration in two subjects)

3.2.2 Results

3.2.2.1.1 Hemodynamic Response to the Cold Pressor Test (CPT)

In this experiment, we would like to determine the effects of a reproducible and safe painful stimulus (CPT) on hemodynamic parameters. The HHb, HbO_2, and Total-Hb have been estimated based on the modified Beer-Lambert law. Motion artifacts were found to be a barrier to the successful analysis of results in one case. However, in the remaining four subjects, the results were very similar, reproducible and can be considered for further analysis. The optical density of the tissue in forehead area is illustrated in Figure 3-9. In this experiment, R and IR represent the optical density of tissue at 740nm and 850nm. Two wavelength intensities are modulated using the source controller. The instruement measures the hemodynamic response during both CPT and recovery time.

The hemodynamic variation of the brain is illustrated in Figure 3-9. The HbO_2 concentration increases during the CPT test and decreases during the recovery period. In the recovery period, the subject's hand was exposed to room temperature (22~24 °C). The concentration of HHb also increases slightly during the cold pressor stimulus, while the HHb and HbO_2 both return to the baseline during the recovery period.

The response of the 'Near' and more superficially penetrating optodes (D=12mm) was very similar to the 'Far' optodes (Distance =28mm). The signals produced by the optodes from the left and right sides of the probe were compared, and no significant differences were observed between the both sides.

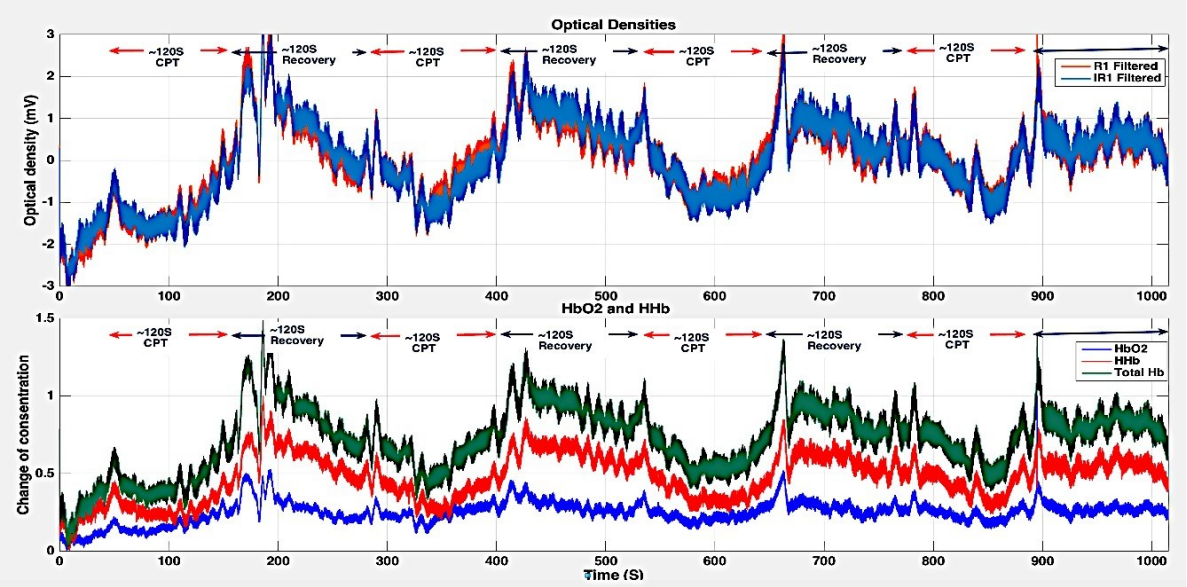

Figure 3-8 The hemodynamic response to cold pressor test (CPT)
The first diagram represents the measurement of optical density in two wavelengths 740nm and 850nm. The measurement is conducted during CPT (forehead, right side). The second diagram illustrates the hemodynamic response of the tissue in the forehead (right side). During the CPT the Total Hb increases, however, it decreases during the recovery time. The result of this experiment is compatible with the experiment, conducted by Zeynab Barati and Dr. K Pourezaee in 2012.

By comparing the results of this experiment and that of the experiment conducted by Zeynab Barati and Dr. K Pourezaee in 2012 [56], it would appear that the results of these two experiments are in agreement. Based on these two recent experiments, it seems that the functionality of the device is acceptable and that the instrument is able to detect variations in HHb and HbO_2 concentrations. After investigating four subjects, no meaningful differences were found between symmetrical NIRS optodes (left side and right side). Moreover, it seems that the increase of Total-Hb in these subjects is largely related to increasing the volume of the blood in the tissue according to the increasing the blood pressure during CPT. See Figure 3-8 (above).

3.2.2.1.2 Hemodynamic Change and EEG Activity Response to Cold Pressor Test (CPT)

Pain may be characterized as an unpleasant experience that affects the conscious awareness of noxious sensations. The measurement of physiological responses to pain may allow the quantification of pain levels. Pain assessment can be critical, especially in patients with chronic disorders of consciousness [59]. These patients have a limited ability to communicate; In spite of their low-level consciousness, somehow they are able to process the pain signals that are generated by peripheral sensory nerves [60, 61].

Several researchers have investigated the neural signature of pain awareness and perception and its relation with Gamma-band oscillations (GBO). The perception of pain invokes a vitally protective reaction, urging the subject to react. Painful stimuli induce widespread propagation of cortical excitability and alerting signals that facilitate a swift reaction to the stimulus[61]. Gamma-band oscillations may be related to voluntary selection, enhanced visual and auditory recognition processes or tactile perceptions. Additionally, Gamma-band oscillations can be observed in response to pain stimuli.

During a painful stimulus, the induced gamma-band oscillations are proportional to the amount of pain consciously perceived. According to recent investigations, the sensory cortex in the central part of the brain as well as the prefrontal lobe may be most significantly implicated in gamma-band oscillations [61].

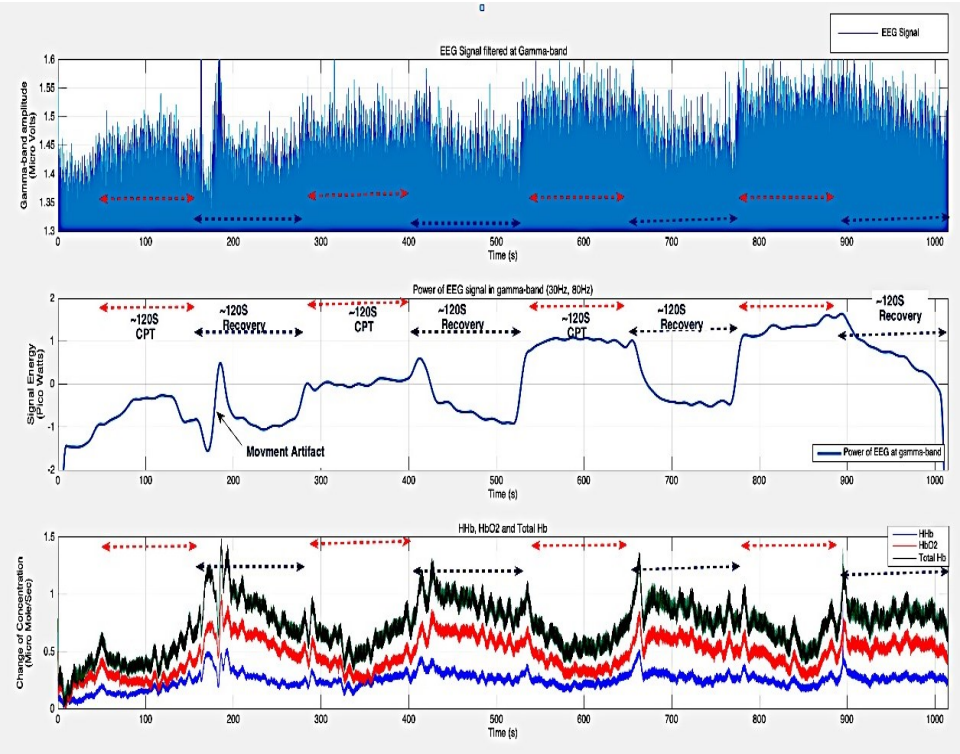

Figure 3-9 The neuronal activity, and hemodynamic variation during CPT.
The first (upper) signal is EEG signal, filtered in gamma-band (30Hz to 70Hz) by IIR filters; A second order IIR 60Hz notch-filter is applied to eliminate the power intertfrences (attentuation~ -45dB) the signal is condensed in the time domain. The change of gamma-band oscillations during CPT can be seen in this diagram.

The second (middle) signal is the power of gamma-band oscillations smoothed by a Hanning filter (5K samples or 10 seconds). The variation of the power during CPT is illustrated in this diagram.

The third signal is the hemodynamic changes of the tissue (forehead) during CPT. The total hemoglobin (THb) increases during CPT and decreases in recovery time.

The EEG signal is from right forehead (A2), and the HHb, HbO_2, and Total-Hb are related to the right forehead. The duration of CPT was 120 seconds and the duration of recovery time was 120 seconds in this experiment.

In this part of the experiment, we intended to measure EEG and hemodynamic responses to the painful stimulus produced by the CPT. The position and the condition of EEG electrodes and NIRS optodes are similar to the "Hemodynamic and Electrophysiologic response to repeated CPT " experiment.

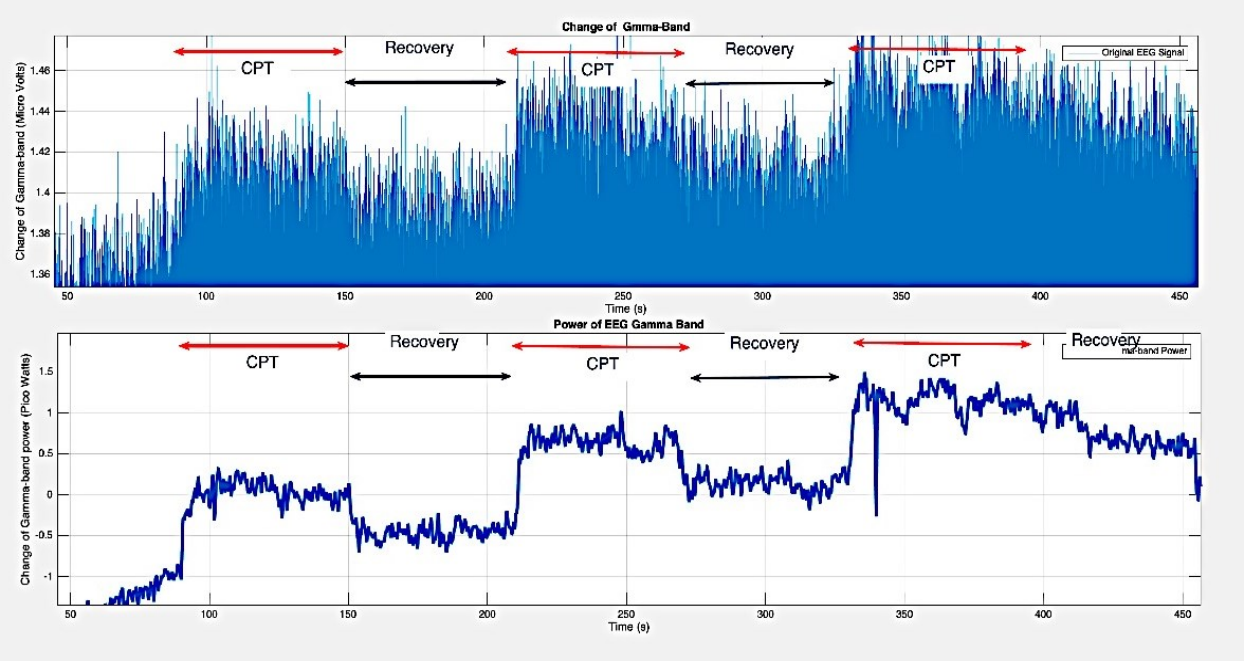

Figure 3-10 Changes of gamma-band power during CPT.
The upper diagram represents the filtered EEG signal in gamma-band (30Hz to 80Hz) the gamma-band signal is condensed in the time domain. A second order IIR 60Hz notch-filter is applied to eliminate the power intertfrences (Attentuation ~ -45dB).

The lower diagram is the power of gamma-band oscillations, smoothed by a Hanning window (2K samples or 4 seconds). This test has been recorded during 60S-CPT, and 60S-recovery. The position of recording electrode was on right forehead. The increasing of gamma-band oscillation due to CPT is shown in this picture.

The EEG signal recorded from electrodes over the frontal lobe has been filtered in the Gamma band (30 to 80Hz). The gamma-band oscillations, condensed in the time domain are illustrated in Figure 3-9 (above), first diagram. As shown, the gamma band oscillation increases during the CPT and decreases during the recovery time. The energy of gamma-band is computed

in the second diagram of Figure 3-9 (above). The signal's energy is smoothed by using Hanning window. As it shown the energy of EEG signal in gamma band increase during the application of the CPT test. The activity of neurons in the gamma band may be due to the pain that is induced during CPT, see Figure 3-10 (above).

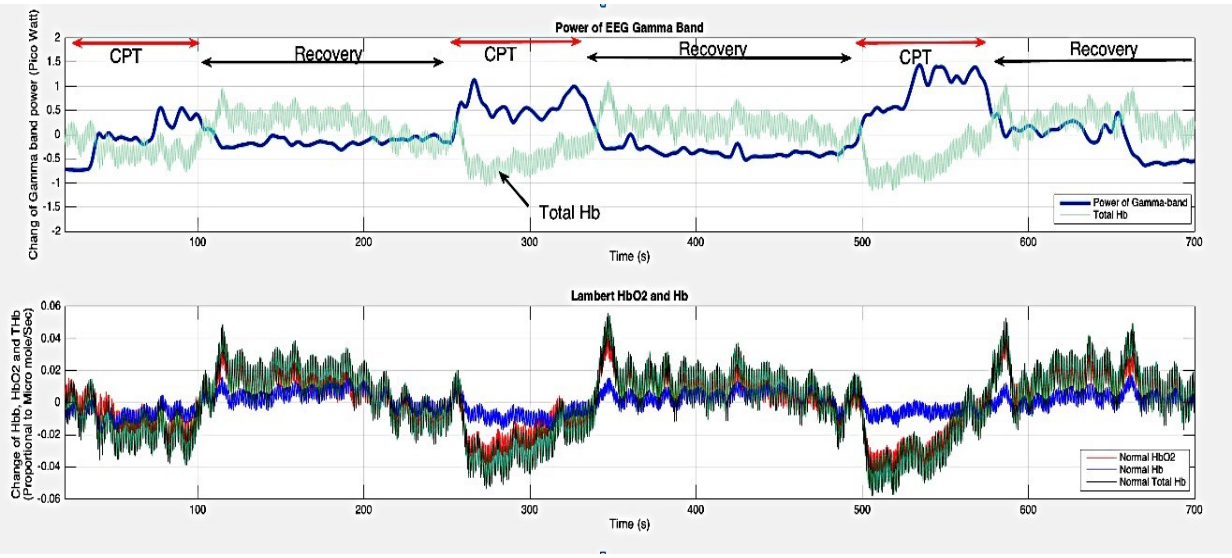

Figure 3-11 Gamma-band oscillations during CPT
The first (upper) diagram shows the power of gamma-band oscillations during CPT in the sensory cortex (B2). As shown, the power of gamma band increases during CPT. (The EEG signal was filtered in gamma-band [30Hz to 80Hz] by IIR filter, the power line interference was eliminated, using a second order IIR 60Hz notch-filter . [Attentuation ~ -45dB].)

The green signal in the background represents the Total-Hb during the experiment. The correlation of gamma-band power and Total-Hb is illustrated in this diagram.

The second (lower) diagram is the change of hemodynamic parameters in forehead left-side during the experiment.

In this experiment, we investigated the presence of gamma-band during the CPT in the area of the brain that resides near to the sensory cortex (B2). As is illustrated in Figure 3-11 (above), the power of the gamma-band increases in the sensory cortex during CPT. Additionally, the power of gamma-band appears to be correlated with Total-Hb of the tissue in the forehead.

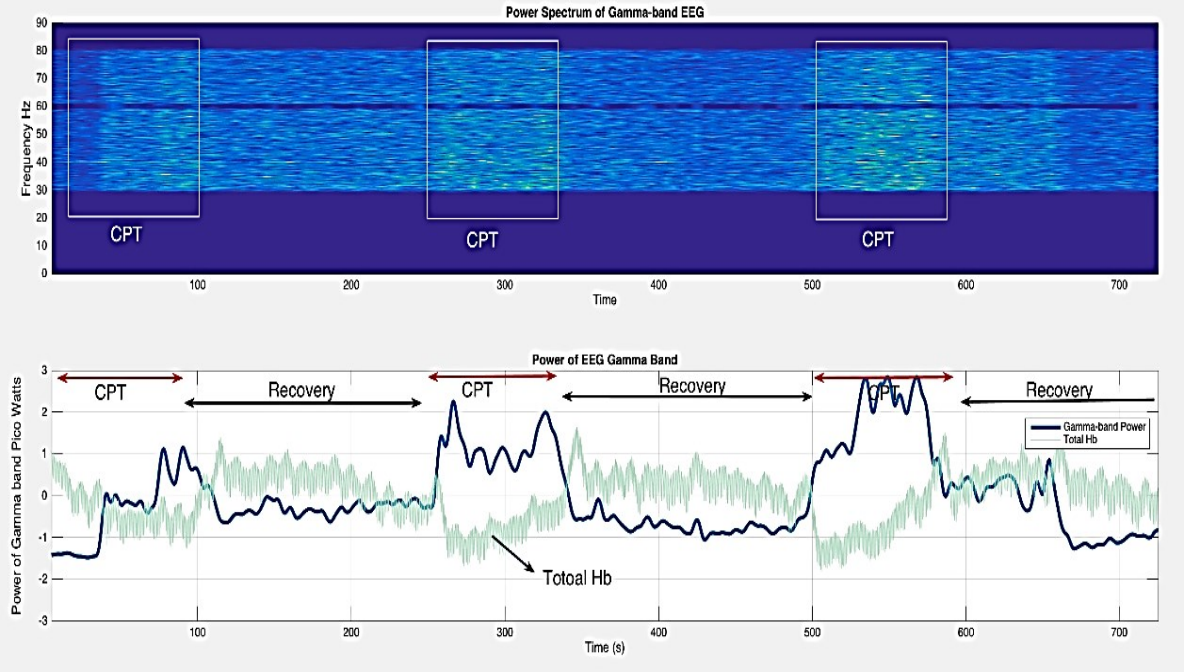

Figure 3-12 Time-frequency transform of EEG signal in gamma-band (30-80Hz).
The upper signal is the spectrogram of gamma-band oscillation, computed based on Short-Time-Fourier-Transform (STFT). The light colored areas in the CPT boxes are according to the high power of gamma-band oscillations during CPT. (The EEG signal was filtered in gamma-band [30Hz to 80Hz] by IIR filter, the power line interference was eliminated, using a second order IIR 60Hz notch-filter. [Attentuation ~ -45dB].)

The lower signal is the power of gamma-band; the green background signal represents the Total-Hb during the experiment. The EEG signal was recorded from the sensory cortex area, on the right side (B2).

Figure 3-12 (above) illustrates the STFT (Short Time Fourier Transform) of EEG in the gamma-band. The distribution of gamma-band oscillations, induced by CPT, is computed over the 30Hz to 80Hz frequency bandwidth. The signal is recorded from B2, which is near to the sensory cortex.

The correlation between Total-Hb and the power of gamma-band oscillations has been examined in 4 subjects. In each subject, the correlation between Total-Hb (forehead, right side) and the power of the gamma-band (forehead, right side) in between corresponding electrodes were calculated (subject one p-value: 0.00003, subject two p-value: 0.000281, Subject three p-

value: 0.971 [no correlation], subject four, p-value: 0.00412, subject five p-value 0.00052). A significant correlation (P-value<0.05, 95% confidence interval) has been observed between these two measurements. In addition, the correlation between Total-Hb (right side, forehead) and the power of the gamma-band oscillations in the sensory cortex (B2 electrode, right side) has been examined in four subjects. (subject one p-value: 0.0022, subject two p-value: 0.00053, Subject three p-value: 0.948 [no correlation], subject four, p-value: 0.0038, subject five p-value 0.00009). A significant correlation (p-value<0.05, 95% confidence interval) was observed.

The correlative analysis demonstrated a strong association between Total-Hb and the power of the gamma-band in localized (forehead left side) as well as general (sensory cortex) areas. As previously mentioned, this study was observational in nature and was limited to a small number of subjects. The study did not show statistically significant results confirming this correlation. However, a future study with an appropriate sample size will be required to determine the significance and validity of the relationship between Total-Hb and the power of the gamma-band oscillation.

3.3 The Hypoxic Breathing Test:

Conventional ideas in electroencephalography (EEG) consider that most of the electrical signals gathered on the surface of the scalp are produced by neuronal networks on cortical dipoles [62]. Some investigations have confirmed the association of glial cells in creating slow local potentials throughout spreading depression, [63], seizures [64], and sleep ([62].Furthermore, pioneer studies in the early 1950s–1970s concluded that slow potential shifts are produced at the cerebrospinal fluid interface. The correlation between slow-EEG or DC-EEG and brain oxygenation has been the subject of few investigations. Some of this correlated activity

may be caused by low-frequency neuronal activity[33, 65]. The neurovascular coupling mechanism reacts to the high concentration of CO_2 (pCO_2) and causes increased oxygenated blood perfusion to the tissue [66]. However, the neurovascular coupling is slightly sensitive to changes in oxygen concentration (pO_2). According to recent investigations, changes in pCO_2 may cause low-frequency shifts, indicated by very slow-EEG signals. However, these slow-EEG signals do not necessarily represent neuronal activity. The non-neuronal slow-EEG shifts caused by pCO_2 changes have been investigated in animal subjects[15].

Cortical spreading depolarization (CSD) is a self-propagating signal, caused by transient loss of neuronal transmembrane ion gradients.[34] Cortical spreading depolarization is associated with vast and dramatic variation in cerebral blood flow (CBF). Despite the initial increases in CBF, hypoxia may occur and extend far into territories of capillary supply.[17] This inverse hemodynamic response is due to swelling of neurons during severe cortical spreading depolarization, and may delay the high energy consuming activity of neuronal recovery. The swelling of tissue during recovery is the major cause of hypoxia; however its effect is superimposed on the highly energy dependent activity of neuronal recovery [17, 65].

In this experiment, we intended to examine the dependent relationship between two related physiological parameters of brain tissue, oxygenation, and slow-EEG potentials, by noninvasively recording NIRS and EEG during hypoxic breathing. Hemodynamic changes in the forehead tissue were measured by utilizing NIRS, alongside concurrent measurement of slow-EEG potentials produced by the brain tissue. During the experiment, an altitude simulation kit was used to restrict the concentration of oxygen in the air that the subject inhaled. During use of the altitude simulation kit, arterial oxygenation, as measured using a pulse oximeter on the index

finger of the subject, dropped dramatically. This confirmed that hypoxic conditions were successfully achieved.

3.3.1 Materials and Methods

3.3.1.1 Principle and Instruments

In this experiment, we intended to record NIRS and EEG signals concurrently during hypoxic breathing. The implemented NIRS hardware has been used in this experiment. The same probe has been utilized in this part of the experiment. See Figure 3-3 (above) and Figure 3-5 (above).

In addition to these 16 EEG electrodes, two additional individual EEG electrodes (Cortech, AC-DC-AGE06 Diameter ~5mm), B1 and B2, have been positioned on the part of the scalp that overlies the sensory cortex. A reference electrode was positioned on left ear. We utilized an Ag/AgCl electrode (Ambu® Neuroline 700, Ag/AgCl, disposable Solid Gel Electrode) as a reference electrode (on the left (43) ear and FZ (23) according to 10/10 EEG electrode placement).

A pulse oximeter on the right index finger (Masimo SET® Rad-8 Pulse Oximeter, Masimo Inc.) monitored arterial blood oxygen saturation throughout the experiment. The altitude simulation kit used to create hypoxic breathing conditions was the AltoLab Platinum BOOST from AltoLab Inc.

3.3.1.2 Subjects

This study is observational in nature, and five healthy volunteers between 20 to 50 years old were enrolled in the experiment. All subjects provided written informed consent to participate in the study.

3.3.1.3 Protocol

This experiment was conducted as part of a UBC CREB approved protocol to test non-invasive sensor prototypes developed by the Electrical and Computer Engineering in Medicine team at the Child and Family Research Institute in Vancouver, BC. The subjects were seated comfortably in an armchair. The probe was fastened symmetrically to the forehead of subjects as previously described. The optical density at two wavelengths (740 and 850nm), as well as the EEG signals, were sampled at a rate of 512 samples per second. The conductive paste (Ten20, Weaver) was applied to the EEG Ag/AgCl electrode on the probe, in order to minimize skin-electrode impedance. The experiment was conducted at room temperature (22~24 °C) and with the normal ambient light present. The relative changes of HHb and HbO_2 and Total-Hb were measured as hemodynamic variation parameters. The EEG signals were recorded concurrently. Two EEG-reference electrodes were used; one positioned frontally Z (23, 10/10 EEG electrode system), and the other one on the left ear (43, 10/10 EEG electrode system).

A pulse oximeter on the right index finger (Masimo SET® Rad-8, Masimo Inc.) was used to monitor the arterial blood oxygen saturation during the experiment. An altitude simulator kit and accompanying mask (AltoLab Platinum BOOST, AltoLab Inc.) was used to create hypoxic breathing conditions. The subject was asked to breathe through the mask until arterial oxygenation as measured by pulse oximeter approached the 85%~95% blood oxygen saturation.

Afterward, the subject was instructed to remove the mask and asked for breath normally for two minutes.

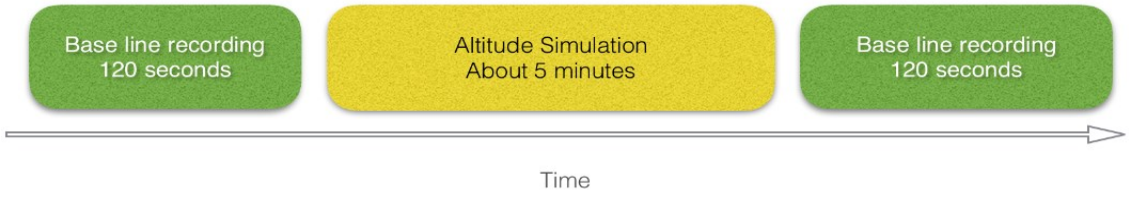

Figure 3-13 The timeline of the experiment.
The timeline of the experiment is illustrated in this picture. The experiment started with 120 seconds of baseline recording, followed by about 5 minutes' altitude simulation, and ended with baseline recording. During the Altitude simulation (AltoLab Platinum BOOST, AltoLab Inc.), the subject was asked to breathe by using an altitude simulation filter until arterial oxygenated, positioned in point finger approached 85% ~ 90%.

3.3.2 Results

The hemodynamic changes in the brain, resulting from hypoxia, were detected by the NIRS recording apparatus, were observed to occur earlier than changes in peripheral oxygenation, as measured using pulse oximetry on the index finger. This delay varied 10 to 15 seconds among subjects.

Speckmann, Gorji, and Elger investigated CO_2-dependent low-frequency EEG potential change in 1999. According to their investigations, low-frequency CO_2-dependent potential shifts are mostly associated with the activity of apical dendrites of cortical neurons. Recent technological advances allow us to record the EEG potentials across the full frequency band. In this study, we used NIRS hemodynamic estimation as a supplementary parameter for recording the neurophysiological activity of the brain, and were able to make observations from a different perspective[33, 34, 65].

In this experiment, we proposed to measure the full-band EEG and concurrent hemodynamic changes during hypoxic breathing conditions. Non-invasive surface electrodes were used during this experiment. The NIRS optodes were positioned on the forehead to monitor the frontal lobe; The Ag/AgCl electrodes were interspersed between the NIRS optodes. Two EEG electrodes monitored electric potentials in sensory cortex.

The pulse oximetry device on the left finger verified the effectiveness of the altitude simulation maneuver, as well as allowed a physician to continually monitor the safety and well-being of the subjects.

The hypoxic breathing conditions led to variation in CO_2 concentration (or partial pressure of CO_2; pCO_2). In all five subjects, the EEG measured from the scalp displayed low-frequency shifts during hypocapnia. As shown Figure 3-14 (below), the EEG low-frequency shifts appeared after the observed hemodynamic changes.

The CO_2-dependent low-frequency shifts in EEG have been investigated using several methods. Most of these investigations have utilized invasive methods to monitor the hemodynamic variation of the brain in a particular area [15].

The graph of hemodynamic response and concurrent EEG illustrates two relevant low-frequency EEG signals, recorded from the forehead (A1 left side), and sensory cortex (10/10 EEG electrode system, CP3(16)). See Figure 3-15 (below).

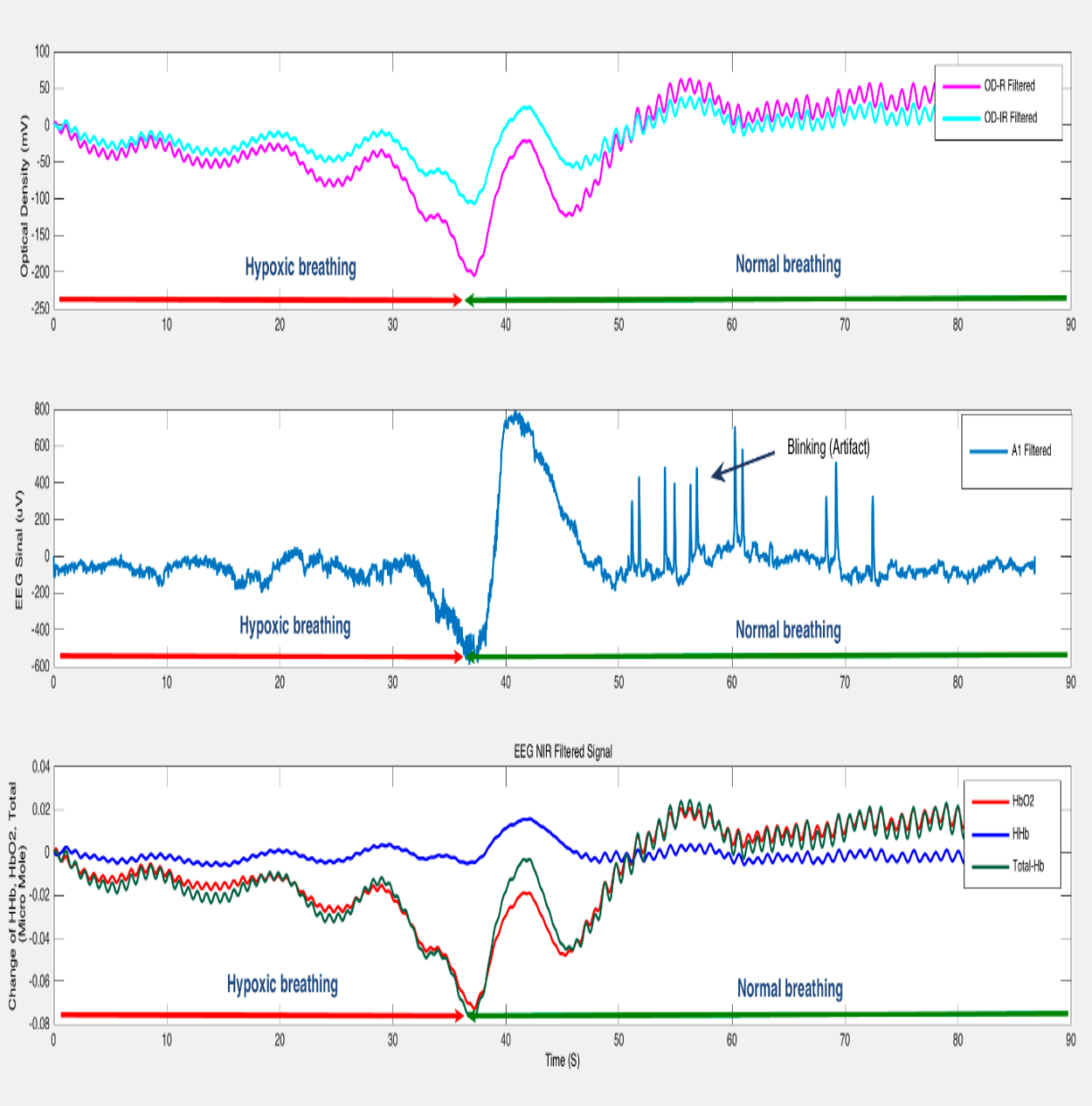

Figure 3-14 EEG and hemodynamic changes induced by hypoxic breathing.
The upper diagram is the optical density of the tissue at 740nm and 850nm wavelengths.

The middle diagram is EEG signal, recorded from the frontal lobe (forehead, left side). The left ear reference electrode has been utilized as the reference for recording this measurement. The low-frequency shift induced by hypoxic breathing is illustrated in this figure.

The lower diagram is the hemodynamic changes of tissue induced by hypoxic breathing.

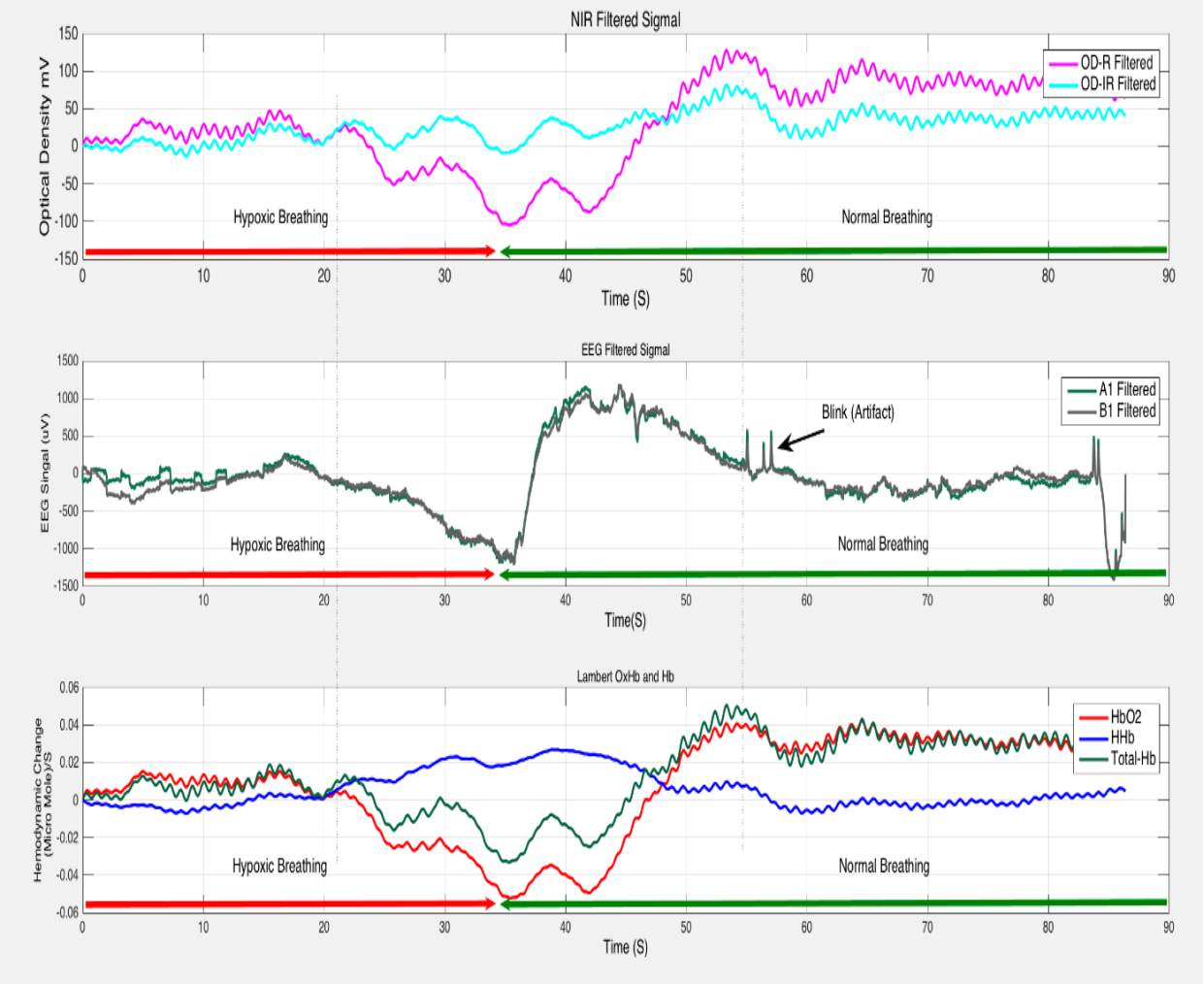

Figure 3-15 EEG and NIRS in the frontal and sensory cortex during hypoxic breathing.
The upper diagram is the optical density of the tissue at 740nm and 850nm wavelengths.

In the middle diagram, two EEG signals are depicted, A1 from the left frontal lobe, and B1 or (CP3(16)) positioned above the sensory cortex.

In the lower diagram, the hemodynamic changes of the tissue induced by hypoxic breathing condition are depicted. The NIRS optodes were positioned on the left side of the forehead. There was no significant difference observed between A1 and B1 with respect to low-frequency EEG components during hemodynamic variation.

The spectrum analysis of the EEG signal by using Short-Time-Fourier-Transform (STFT) is illustrated in Figure 3-16 (below). The low-frequency activity of the EEG signal is presented in this picture.

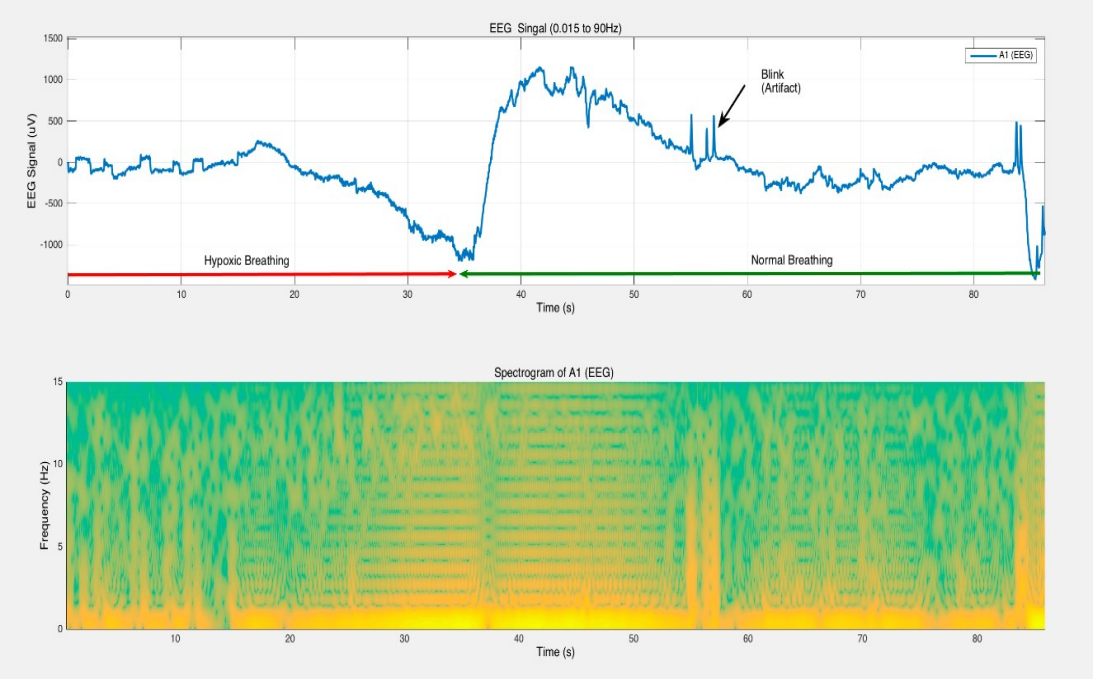

Figure 3-16 The time-frequency analysis of signal based on STFT.
The signal spectrum is estimated based on STFT. The change of the signal spectrum during hypoxia breathing can be seen in this diagram.

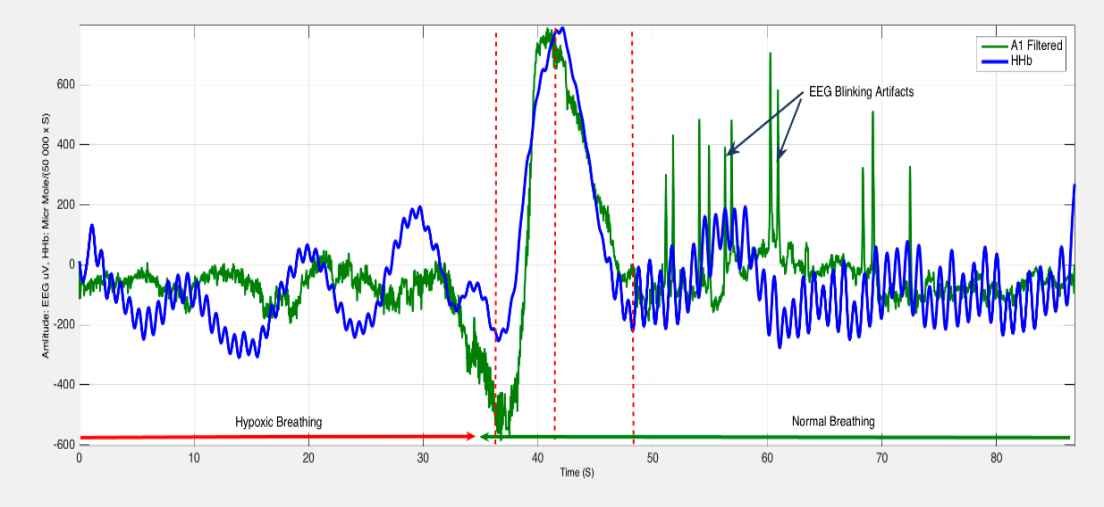

Figure 3-17 The superposition of EEG signal A1 and HHb multiplied by 50K.
The superposition of A1 and HHb recorded at the frontal lobe, left size. The HHb represents the change in concentration of non-oxygenated hemoglobin, estimated by using NIRS.

The superposition of HHb and EEG signal, recorded at the frontal lobe in the left side is illustrated in Figure 3-17. The EEG changes induced by CO_2 concentration are proportional to the HHb parameter recorded by the NIRS subsystem. See Figure 3-17 (above).

An investigation, conducted in 2004 at Helsinki University,[15] studied the genesis of slow-wave EEG recorded during hypoxia. Researchers investigated a variety of causes that may be involved in the genesis of slow EEG signal during hypoxic breathing. The result of our experiment included slow-EEG signals and the concentration of CO_2 concurrently, and the results of these studies appear to be in agreement.

Chapter 4: Conclusion

Since the first introduction of NIRS by Jobsis, many advanced investigations have been conducted to apply this non-invasive physiological monitoring method to various biomedical applications. The combination of NIRS and EEG is a promising application of NIRS in neurology and neuroscience studies. In this thesis, we attempted to address some of the applications of NIRS/EEG recording and current issues in NIRS/EEG signal processing.

4.1 Design and Implementation NIRS/EEG Instrument

In this chapter, we reported the design of the NIRS/EEG instrument to record the hemodynamic changes and electrophysiological activity of the brain. The design process began with the evaluation of different methods and components. For detecting NIR at the receiver site, a photodiode was proposed, and LED was proposed as a light source. The sensitivity of photodiodes is appropriate for recording the signal on the forehead. However, the recorded signal from the hair-covered part of the scalp was not satisfactory. The SNR for the signal recorded was insufficient due to the high absorption rate of melanin particles in the hair itself. Optical detectors, like APD components, may be considered as alternatives that could be employed in future designs. The design and implementation of a probe secured to the forehead by a single strap are also explained in this chapter. The functionality of the cap, after investigation, was shown to be satisfactory. The device is able to apply four wavelengths, concurrently. In this

research, we used two wavelengths (670nm and 850nm). However, in future work, four wavelengths may be analyzed to provide a more precise estimation of the hemodynamic changes in the subject's tissue.

Utilizing the amplitude modulation methods to multiplex NIR sources eliminated the interference produced by ambient illumination and improved the SNR of the signal. In this design, we adopted the hardware asynchronous modulation method, which is a nonlinear process that may cause some distortion and deformities. The synchronous modulation method, with greater linearity and less distortion, can be considered as one potential and substantial improvement for future research in this area.

4.2 NIRS/EEG Validation

In NIRS/EEG validation, the NIRS/EEG instrument has been utilized for conducting three experiments. The first experiment was conducted for the purpose of measuring the hemodynamic changes of the forearm during occlusion. The change of HHb and HbO_2 was observed and reported.

The next experiment was the measurement of hemodynamic changes (HHb, HbO_2, and Total-Hb) while CPT was applied. The result of the experiment was very similar to the equivalent study, which was conducted at Drexel University by Zeynab Barati and Dr. K Pourezaee in 2012 [2]. The increase of blood perfusion during the CPT pain stimulus was observed in all the areas of the forehead. Additionally, detection of gamma-band oscillation was conducted as part of this experiment. Brain activation is accompanied by a complex sequence of cellular, metabolic, and vascular processes. Neuronal activity is an energy-consuming process that necessitates a high amount of glucose and oxygen and, consequently, produces a large

amount of CO_2. A regional increase in cortical activity accompanies a local increase in blood flow. This mechanism is called neurovascular coupling. This study has found an increase in gamma-band activity and total blood perfusion (30–80 Hz) over frontal scalp sites, due to the subjective experience of pain (CPT). The change in gamma-band oscillations should not be considered as the only cause of the blood perfusion increase in the tissue.

A high correlation between the power of the gamma-band (30Hz to 80Hz) and the Total-Hb has been observed and reported. The cause and effect relationship between the power of the gamma-band and the amount of blood perfusion may be a prospective subject of future investigation.

The measurement of neurophysiologic and hemodynamic responses to imposed subjective pain in a larger subject cohort should be undertaken in another future investigation. This experiment is key to demonstrating the significance of NIRS/EEG technology in neurology and neuroscience applications.

Recording NIRS/EEG during hypoxic breathing is the final experiment discussed in this thesis. The hypoxic breathing conditions led to variations in CO_2 concentration (or partial pressure of CO_2; pCO_2). We observed low-frequency EEG shifts during the hypoxic periods. In the study conducted in 2004 at Helsinki University, the researchers investigated a variety of causes that may be involved in the genesis of slow EEG signal during hypoxic breathing in animal subjects [15]. According to their study, the changes in pCO_2 induced low-frequency shifts in EEG recording. The change in CO_2 concentration is proportional to that of HHb, which is estimated by the NIRS measurements in our experiment.

The association between HHb and slow EEG signals, as observed in this study, is analyzed and reported. The results of this analysis included slow-EEG signals and the concurrent change of CO_2 concentration. The aforementioned results appear to be in agreement with those of previously reported studies. Consequently, the EEG shifts, measured on the surface of the scalp, were non-neuronal EEG and did not represent the low-frequency activity of the neurons. Our experiment was observational in nature. However, the number of subjects in this study was not sufficiently powered to prove statistically significant correlation between HHb and slow EEG shifts. A study with a larger number of subjects is required to demonstrate the significance of this association.

Bibliography

[1] Z. Bastany, "Scalp ultra-low frequency (DC-coupled) Electroencephalography " *Master of Applied Acinece, Univeristy of British Columbia, Vancouver,* Unpublished.

[2] Z. Barati, P. A. Shewokis, M. Izzetoglu, R. Polikar, G. Mychaskiw, and K. Pourrezaei, "Hemodynamic response to repeated noxious cold pressor tests measured by functional near infrared spectroscopy on forehead," *Annals of biomedical engineering,* vol. 41, pp. 223-237, 2013.

[3] M. Cutler, "Transillumination as an aid in the diagnosis of breast lesions," *Surgery, gynecology and obstetrics,* vol. 48, pp. 721-729, 1929.

[4] M. Perutz, "Hoppe-Seyler, Stokes and haemoglobin," *Biological chemistry Hoppe-Seyler,* vol. 376, pp. 449-450, 1995.

[5] K. Schübel, "Zur Pharmakologie der Chlorogensäure," *Naunyn-Schmiedebergs Archiv für Experimentelle Pathologie und Pharmakologie,* vol. 190, pp. 199–200, 1938.

[6] Y. Hoshi, "Functional near-infrared spectroscopy: current status and future prospects," *Journal of Biomedical Optics,* vol. 12, p. 062106, 2007.

[7] S. Cutini, S. Moro, and S. Bisconti, "Review: Functional near infrared optical imaging in cognitive neuroscience: an introductory review," *Journal of Near Infrared Spectroscopy,* vol. 20, p. 75, 2012.

[8] F. Scholkmann, S. Kleiser, A. J. Metz, R. Zimmermann, J. Mata Pavia, U. Wolf*, et al.*, "A review on continuous wave functional near-infrared spectroscopy and imaging instrumentation and methodology," *NeuroImage,* vol. 85, pp. 6–27, 2014.

[9] Gregg, "Brain specificity of diffuse optical imaging: improvements from superficial signal regression and tomography," *Frontiers in Neuroenergetics,* 2010.

[10] A. N. Gay, D. A. Lazar, B. Stoll, B. Naik-Mathuria, O. P. Mushin, M. A. Rodriguez*, et al.*, "Near-infrared spectroscopy measurement of abdominal tissue oxygenation is a useful indicator of intestinal blood flow and necrotizing enterocolitis in premature piglets," *Journal of pediatric surgery,* vol. 46, pp. 1034-1040, 2011.

[11] B. Molavi and G. A. Dumont, "Wavelet-based motion artifact removal for functional near-infrared spectroscopy," *Physiological measurement,* vol. 33, p. 259, 2012.

[12] M. Takeuchi, E. Hori, K. Takamoto, A. H. Tran, K. Satoru, A. Ishikawa*, et al.*, "Brain Cortical Mapping by Simultaneous Recording of Functional Near Infrared Spectroscopy and Electroencephalograms from the Whole Brain During Right Median Nerve Stimulation," *Brain Topography,* vol. 22, pp. 197–214, 2009.

[13] S. Sanei and J. A. Chambers, *EEG signal processing*: John Wiley & Sons, 2013.

[14] P. Olejniczak, "Neurophysiologic basis of EEG," *Journal of clinical neurophysiology,* vol. 23, pp. 186-189, 2006.

[15] D. A. Nita, S. Vanhatalo, F.-D. Lafortune, J. Voipio, K. Kaila, and F. Amzica, "Nonneuronal origin of CO2-related DC EEG shifts: an in vivo study in the cat," *Journal of neurophysiology,* vol. 92, pp. 1011-1022, 2004.

[16] S. A. Zoya Bastany, Guy A. Dumont, Ali Gorji, "Non-invasive monitoring of spreading depression," *Neuro Science Journal (NSC),* Unpublished (Acceptance of NSC-16-755R2).

[17] L. Østergaard, J. P. Dreier, N. Hadjikhani, S. N. Jespersen, U. Dirnagl, and T. Dalkara, "Neurovascular Coupling During Cortical Spreading Depolarization and–Depression," *Stroke,* vol. 46, pp. 1392-1401, 2015.

[18] J. P. Dreier, "The role of spreading depression, spreading depolarization and spreading ischemia in neurological disease," *Nature medicine,* vol. 17, pp. 439-447, 2011.

[19] M. Bélanger, I. Allaman, and P. J. Magistretti, "Brain energy metabolism: focus on astrocyte-neuron metabolic cooperation," *Cell metabolism,* vol. 14, pp. 724-738, 2011.

[20] B. N. Pasley and R. D. Freeman, "Neurovascular coupling," *Scholarpedia,* vol. 3, p. 5340, 2008.

[21] R. Avila-Flores and R. A. Medellin, "Ecological, taxonomic, and physiological correlates of cave use by mexican bats," *Journal of Mammalogy,* vol. 85, pp. 675-687, Aug 2004.

[22] J. G. Webster, *Design of pulse oximeters*: CRC Press, 1997.

[23] J. G. Kim, M. Xia, and H. Liu, "Extinction coefficients of hemoglobin for near-infrared spectroscopy of tissue," *Engineering in Medicine and Biology Magazine, IEEE,* vol. 24, pp. 118-122, 2005.

[24] A. Sassaroli and S. Fantini, "Comment on the modified Beer? Lambert law for scattering media," *Physics in Medicine and Biology,* vol. 49, p. N255, 2004.

[25] I. E. Commission, "IEC 62471: 2006," *Photobiological safety of lamps and lamp systems. Geneva: IEC,* 2006.

[26] I. E. Commision, "Photobiological safety of lamps and lamp systems. Technical report,," p. 12, 2006.

[27] A. Bozkurt and B. Onaral, "Safety assessment of near infrared light emitting diodes for diffuse optical measurements," *Biomedical engineering online,* vol. 3, p. 9, 2004.

[28] G. Strangman, D. A. Boas, and J. P. Sutton, "Non-invasive neuroimaging using near-infrared light," *Biological psychiatry,* vol. 52, pp. 679-693, 2002.

[29] M. S. Patterson, S. Andersson-Engels, B. C. Wilson, and E. K. Osei, "Absorption spectroscopy in tissue-simulating materials: a theoretical and experimental study of photon paths," *Applied optics,* vol. 34, pp. 22-30, 1995.

[30] N. Roche-Labarbe, F. Wallois, E. Ponchel, G. Kongolo, and R. Grebe, "Coupled oxygenation oscillation measured by NIRS and intermittent cerebral activation on EEG in premature infants," *Neuroimage,* vol. 36, pp. 718-727, 2007.

[31] D. P. Subha, P. K. Joseph, R. Acharya, and C. M. Lim, "EEG signal analysis: a survey," *Journal of medical systems,* vol. 34, pp. 195-212, 2010.

[32] R. Srinivasan, "Methods to improve the spatial resolution of EEG," *International Journal of Bioelectromagnetism,* vol. 1, pp. 102-111, 1999.

[33] A. Gorji and E.-J. Speckmann, "Epileptiform EEG spikes and their functional significance," *Clinical EEG and neuroscience,* vol. 40, pp. 230-233, 2009.

[34] E. Speckmann, C. Elger, and A. Gorji, "Neurophysiologic basis of EEG and DC potentials," *Niedermeyer's Electroencephalography,* pp. 17-32, 2011.

[35] E.-J. Speckmann, "Introduction of the neurophysiological basis of the EEG and DC potentials," *Electroencephalography: Basic principles, clinical applications, and related fields,* pp. 15-26, 1993.

[36] H. Saadi and M. Attari, "Electrode-gel-skin interface characterization and modeling for surface biopotential recording: Impedance measurements and noise," in *Advances in Biomedical Engineering (ICABME), 2013 2nd International Conference on*, 2013, pp. 49-52.

[37] K. Peng, D. K. Nguyen, T. Tayah, P. Vannasing, J. Tremblay, M. Sawan*, et al.*, "fNIRS-EEG study of focal interictal epileptiform discharges," *Epilepsy research,* vol. 108, pp. 491-505, 2014.

[38] F. Wallois, A. Patil, C. Héberlé, and R. Grebe, "EEG-NIRS in epilepsy in children and neonates," *Neurophysiologie Clinique/Clinical Neurophysiology,* vol. 40, pp. 281-292, 2010.

[39] F. Wallois, M. Mahmoudzadeh, A. Patil, and R. Grebe, "Usefulness of simultaneous EEG–NIRS recording in language studies," *Brain and language,* vol. 121, pp. 110-123, 2012.

[40] B. Molavi, L. May, J. Gervain, M. Carreiras, J. F. Werker, and G. A. Dumont, "Analyzing the resting state functional connectivity in the human language system using near infrared spectroscopy," *Frontiers in human neuroscience,* vol. 7, 2013.

[41] D. Zhang, X. Hou, Y. Liu, C. Zhou, Y. Luo, and H. Ding, "The utility of amplitude-integrated EEG and NIRS measurements as indices of hypoxic ischaemia in the newborn pig," *Clinical Neurophysiology,* vol. 123, pp. 1668-1675, 2012.

[42] U. Food and D. Administration, "Design control guidance for medical device manufacturers," *Center for Devices and Radiological Health, Rockville, MD, USA: United States Food and Drug Administration,* 1997.

[43] R. Kaye and J. Crowley, "Guidance for industry and FDA premarket and design control reviewers. Medical device use-safety: incorporating human factors engineering into risk management. Document issued on July 18, 2000," ed, 2012.

[44] I.-S. Jeong, J. H. Kim, and S. Im, "Ultraviolet-enhanced photodiode employing n-ZnO/p-Si structure," *Applied physics letters,* vol. 83, pp. 2946-2948, 2003.

[45] T. Rauch, M. Böberl, S. F. Tedde, J. Fürst, M. V. Kovalenko, G. Hesser*, et al.*, "Near-infrared imaging with quantum-dot-sensitized organic photodiodes," *nature photonics,* vol. 3, pp. 332-336, 2009.

[46] T. Swe and K. Yeo, "An accurate photodiode model for DC and high frequency SPICE circuit simulation," in *Technical Proceedings of the 2001 International Conference on Modeling and Simulation of Microsystems*, 2001, pp. 362-365.

[47] S. Donati, "Photodetectors: devices, circuits, and applications," ed: IOP Publishing, 2001, p. 103.

[48] R. J. Keyes, *Optical and infrared detectors* vol. 19: Springer Science & Business Media, 2013.

[49] T. Yagi, "Light emitting diode," ed: Google Patents, 2004.

[50] H. W. Siesler, Y. Ozaki, S. Kawata, and H. M. Heise, *Near-infrared spectroscopy: principles, instruments, applications*: John Wiley & Sons, 2008.

[51] A. Pellicer and M. del Carmen Bravo, "Near-infrared spectroscopy: a methodology-focused review," in *Seminars in Fetal and Neonatal Medicine*, 2011, pp. 42-49.

[52] P. Horowitz, W. Hill, and T. C. Hayes, *The art of electronics* vol. 2: Cambridge university press Cambridge, 1989.

[53] A. V. Oppenheim, R. W. Schafer, and J. R. Buck, *Discrete-time signal processing* vol. 2: Prentice hall Englewood Cliffs, NJ, 1989.

[54] A. M. Van Rijn, A. Peper, and C. Grimbergen, "High-quality recording of bioelectric events," *Medical and Biological Engineering and Computing,* vol. 28, pp. 389-397, 1990.
[55] P. Tallgren, S. Vanhatalo, K. Kaila, and J. Voipio, "Evaluation of commercially available electrodes and gels for recording of slow EEG potentials," *Clinical Neurophysiology,* vol. 116, pp. 799-806, 2005.
[56] M. Menkes, K. A. Matthews, D. S. Krantz, U. Lundberg, L. A. Mead, B. Qaqish*, et al.*, "Cardiovascular reactivity to the cold pressor test as a predictor of hypertension," *Hypertension,* vol. 14, pp. 524-530, 1989.
[57] M. A. Greene, A. J. Boltax, G. A. Lustig, and E. Rogow, "Circulatory dynamics during the cold pressor test," *The American journal of cardiology,* vol. 16, pp. 54-60, 1965.
[58] V. Jurcak, D. Tsuzuki, and I. Dan, "10/20, 10/10, and 10/5 systems revisited: their validity as relative head-surface-based positioning systems," *Neuroimage,* vol. 34, pp. 1600-1611, 2007.
[59] F. Plum and J. B. Posner, *The diagnosis of stupor and coma* vol. 19: Oxford University Press, USA, 1982.
[60] P. Martelletti, R. H. Jensen, A. Antal, R. Arcioni, F. Brighina, M. de Tommaso*, et al.*, "Neuromodulation of chronic headaches: position statement from the European Headache Federation," *J Headache Pain,* vol. 14, p. 86, 2013.
[61] M. de Tommaso, "Response: Commentary: Cortical responses to salient nociceptive and not nociceptive stimuli in vegetative and minimal conscious state," *Frontiers in human neuroscience,* vol. 10, 2016.
[62] F. Amzica, "Physiology of sleep and wakefulness as it relates to the physiology of epilepsy," *Journal of clinical neurophysiology,* vol. 19, pp. 488-503, 2002.
[63] G. G. Somjen, "Ion regulation in the brain: implications for pathophysiology," *The Neuroscientist,* vol. 8, pp. 254-267, 2002.
[64] U. Heinemann and W. Walz, "Contribution of potassium currents and glia to slow potential shifts (SPSs)," *Glial cells: their role in behaviour,* pp. 197-209, 1998.
[65] A. Gorji, D. Scheller, H. Straub, F. Tegtmeier, R. Köhling, J.-M. Höhling*, et al.*, "Spreading depression in human neocortical slices," *Brain research,* vol. 906, pp. 74-83, 2001.
[66] M. Freeman, A. Mauskopf, S. Mei, K. Stanke, and Z. Yan, "Neurovascular coupling," *Neuron,* 2014.